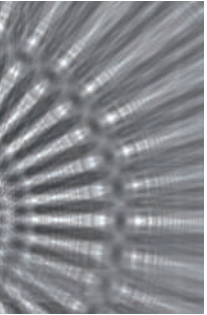


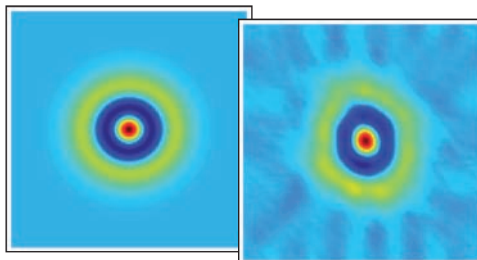
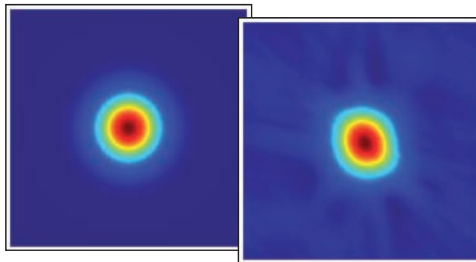
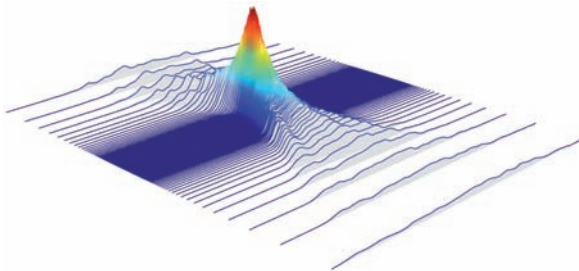


Göttingen Series in
X-ray Physics



Tobias Mey

Radiation characteristics of extreme UV and soft X-ray sources



Universitätsverlag Göttingen

Tobias Mey

Radiation characteristics of extreme UV and soft X-ray sources

This work is licensed under a [Creative Commons Attribution-ShareAlike 4.0 International License](https://creativecommons.org/licenses/by-sa/4.0/).



Published in 2015 by Universitätsverlag Göttingen
as volume 15 in the series „Göttingen series in X-ray physics“

Tobias Mey

Radiation characteristics
of extreme UV
and soft X-ray sources

Göttingen series in X-ray physics
Volume 15



Universitätsverlag Göttingen
2015

Bibliographic information published by the Deutsche Nationalbibliothek

The Deutsche Nationalbibliothek lists this publication in the Deutsche Nationalbibliografie; detailed bibliographic data are available on the Internet at <http://dnb.dnb.de>.

Address of the Author

Tobias Mey

e-mail: tobias.mey@llg-ev.de

Dissertation

for the award of the degree

“Doctor rerum naturalium”

of the Georg-August-Universität Göttingen

within the doctoral program ProPhys

of the Georg-August University School of Science (GAUSS)

Thesis Committee:

Prof. Dr. Tim Salditt

Prof. Dr. Claus Ropers

This work is protected by German Intellectual Property Right Law.

It is also available as an Open Access version through the publisher's homepage and the Göttingen University Catalogue (GUK) at the Göttingen State and University Library (<http://www.sub.uni-goettingen.de>).

The conditions of the license terms of the online version apply.

Layout: Tobias Mey

Cover: Jutta Pabst

Cover image: Tobias Mey

© 2015 Universitätsverlag Göttingen

<http://univerlag.uni-goettingen.de>

ISBN: 978-3-86395-211-2

ISSN: 2191-9860

Preface of the series editors

The Göttingen series in x-ray physics is intended as a collection of research monographs in x-ray science, carried out at the Institute for X-ray Physics at the Georg-August-Universität in Göttingen, and in the framework of its related research networks and collaborations.

It covers topics ranging from x-ray microscopy, nano-focusing, wave propagation, image reconstruction, tomography, short x-ray pulses to applications of nanoscale x-ray imaging and biomolecular structure analysis.

In most but not all cases, the contributions are based on Ph.D. dissertations. The individual monographs should be enhanced by putting them in the context of related work, often based on a common long term research strategy, and funded by the same research networks. We hope that the series will also help to enhance the visibility of the research carried out here and help others in the field to advance similar projects.

Prof. Dr. Sarah Köster

Prof. Dr. Tim Salditt

Editors

Göttingen June 2014

ABSTRACT

Electromagnetic radiation in the extreme UV and soft x-ray spectral range is of steadily increasing importance in fundamental research and industrial applications. For instance, the molecular structure of certain proteins and viruses has become accessible by coherent imaging techniques and already today, lithographic processes for the microchip production are being adapted to that wavelength range. For both examples, a comprehensive beam characterization is an essential condition for an ideal use of the available photons. Following that goal, this work addresses the pathway of extreme UV and soft x-ray radiation from its generation, through the beam transport by the beamline to the probe position. Experimentally, those aspects are optimized at a laser-produced plasma source and at an arrangement for the generation of high-harmonics. Additionally, the coherence of laser beams is analyzed by measurements of the Wigner distribution function. This method is applied to the photon beam of the free-electron laser FLASH, resulting in the entire characterization of its propagation properties.

ZUSAMMENFASSUNG

Elektromagnetische Strahlung im extremen UV und weichen Röntgenspektralbereich ist von stetig wachsender Bedeutung, sowohl im Bereich der Forschung als auch in industriellen Anwendungen. So konnte beispielsweise erstmals die Molekülstruktur bestimmter Proteine und Viren entschlüsselt werden und bereits heute werden die lithographischen Prozesse zur Herstellung von Mikrochips auf diesen Wellenlängenbereich adaptiert. Dabei ist eine umfassende Strahlcharakterisierung die Grundlage für eine ideale Nutzung der Photonen. Unter dieser Zielsetzung behandelt die vorliegende Arbeit den gesamten Weg der extremen UV und weichen Röntgenstrahlung, von ihrer Erzeugung, über die Strahlführung bis hin zur Probenposition. Experimentell werden diese Aspekte an einer Laser-produzierten Plasmaquelle beziehungsweise an einer Anordnung zur Erzeugung Hoher Harmonischen optimiert. Weiterhin wird die Kohärenz von Laserstrahlen anhand der Wigner Verteilungsfunktion analysiert. Die Methode wird auf den Photonenstrahl des Freien-Elektronen Lasers FLASH angewendet und liefert eine vollständige Beschreibung seiner Propagationseigenschaften.

PUBLICATIONS

Some ideas and figures have appeared previously in the following publications:

B. Schäfer, B. Flöter, T. Mey, P. Juranic, S. Kapitzki, B. Keitel, E. Plönjes, K. Mann and K. Tiedtke
“FEL beam characterization from measurements of the Wigner distribution function”
Nuclear Instruments and Methods in Physics Research A 654, 502-507 (2011)

T. Mey, M. Rein, P. Großmann and K. Mann
“Brilliance improvement of laser-produced soft x-ray plasma by a barrel shock”
New Journal of Physics 14, 073045 (2012)

T. Mey, B. Schäfer, K. Mann, B. Keitel, M. Kuhlmann and E. Plönjes
“Wigner distribution measurements of the spatial coherence properties of the free-electron laser FLASH”
Optics Express 22, 016571 (2014)

M. Müller, T. Mey, J. Niemeyer and K. Mann
“Table-top soft x-ray microscope using laser-induced plasma from a pulsed gas jet”
Optics Express 22, 023489 (2014)

T. Mey, B. Schäfer and K. Mann
“Measurement of the Wigner distribution function of non-separable laser beams employing a toroidal mirror”
New Journal of Physics 16, 123042 (2014)

T. Mey, S. Zayko, C. Ropers, B. Schäfer and K. Mann
“Toroidal grating astigmatism of high-harmonics characterized by EUV Hartmann sensor”
Optics Express 23, 15310 (2015)

CONTENTS

1	INTRODUCTION	1
2	EUV AND SOFT X-RAY SOURCES	5
2.1	Laser-produced plasma	7
2.2	High-harmonic generation	17
2.3	Free-Electron Laser	23
3	THEORY OF BEAM CHARACTERIZATION	29
3.1	Matrix methods in ray optics	29
3.2	The wavefront	33
3.3	Coherence properties	36
3.4	The Wigner distribution function	41
4	BRILLIANCE IMPROVEMENT OF A LASER-PRODUCED PLASMA SOURCE	49
4.1	The laser-produced soft x-ray source	50
4.2	Gas jet and soft x-ray diagnostics	52
4.3	Experimental results	56
5	BEAM TRANSPORT OF HIGH HARMONICS	65
5.1	Characterization of high harmonic beam	66
5.2	Alignment of toroidal grating	74
6	COHERENCE MEASUREMENTS AT THE FREE-ELECTRON LASER FLASH	79
6.1	Experiment at FLASH	80
6.2	Reconstruction of the Wigner distribution function	82
6.3	Results	85
6.4	Error estimations	94
6.5	4D measurement	100
7	SUMMARY	107
A	APPENDIX	109
A.1	Ray transformation matrices	109
A.2	Wigner reconstruction algorithm	111
	BIBLIOGRAPHY	117

LIST OF FIGURES

Figure 0.1	Color scales employed in this work	xi
Figure 1.1	Electromagnetic spectrum from the infrared to the hard x-ray range	1
Figure 1.2	Influence of beam aberrations and coherence on focusing properties	2
Figure 2.1	Classification of EUV and soft x-ray sources	6
Figure 2.2	Scheme of the emission spectrum of a hot dense plasma	8
Figure 2.3	Sketch of a de Laval nozzle	11
Figure 2.4	State functions of a flow in a de Laval nozzle	12
Figure 2.5	Illustration of a normal shock	13
Figure 2.6	Typical structure of a barrel shock	14
Figure 2.7	State functions along the symmetry axis of a barrel shock	15
Figure 2.8	Typical HHG spectrum	17
Figure 2.9	Ionization mechanisms depending on the Keldysh parameter γ_K	18
Figure 2.10	Trajectories of electrons during the HHG pro- cess	20
Figure 2.11	Kinetic energy E_{kin} of an electron at recollis- ion with the ion and recollision time t_0 after ionization	21
Figure 2.12	Generation of undulator radiation	24
Figure 2.13	Microbunching	26
Figure 2.14	Exponential gain of the photon pulse energy by the SASE process	27
Figure 3.1	Definition of the ray vector	30
Figure 3.2	Local beam diameter around beam waist . . .	32
Figure 3.3	Variance ellipse of the near-field	33
Figure 3.4	The first ten Zernike polynomials	35
Figure 3.5	Definition of the mutual coherence function	37
Figure 3.6	Coherence functions in the Gaussian Schell- model	39
Figure 3.7	Wigner distribution function	42
Figure 3.8	Propagation of the Wigner distribution func- tion	45
Figure 3.9	Scheme of the reconstruction of the Wigner distribution function	47
Figure 4.1	Principle of plasma generation	50

Figure 4.2	Emission spectra of various target gases . . .	51
Figure 4.3	Experimental setup for Schlieren and wavefront measurements	52
Figure 4.4	Wavefront deformation due to the gas jet . .	53
Figure 4.5	Plasma characterization by pinhole camera and diode measurement	55
Figure 4.6	Schlieren images indicating the supersonic flow structure of a N ₂ jet	57
Figure 4.7	Distance between Mach disk and nozzle exit for various pressure ratios	58
Figure 4.8	Wavefront and Schlieren image with density distribution in the target gas jet	59
Figure 4.9	Pinhole camera images of the plasma superimposed on Schlieren images of gas jet . . .	61
Figure 4.10	Pinhole camera images of the plasma for various background pressures	62
Figure 5.1	Setup of HHG source with two toroidal gratings	67
Figure 5.2	Intensity profiles of HHG beam	68
Figure 5.3	Local diameters of HHG beam in proximity of the focus	69
Figure 5.4	Optical path through an arrangement of focusing gratings	71
Figure 5.5	Wavefront of the 25 th harmonic	73
Figure 5.6	Individual spots captured by the wavefront sensor	74
Figure 5.7	Setup of HHG source with a single toroidal grating	75
Figure 5.8	HHG wavefront for different incidence angles	76
Figure 5.9	Astigmatic waist difference against incidence angle	78
Figure 6.1	Setup for measurement of intensity profiles at FLASH	80
Figure 6.2	Intensity profiles of the photon beam at FLASH	81
Figure 6.3	Reconstruction of the Wigner distribution function	83
Figure 6.4	Wigner distribution function of the FLASH beam	86
Figure 6.5	Reconstruction of intensity profiles from the WDF	88
Figure 6.6	Sections of a reconstructed intensity profile .	89
Figure 6.7	Mutual coherence function of the FLASH beam	90
Figure 6.8	Local degree of coherence	91

Figure 6.9	Position of apertures in the beam line	92
Figure 6.10	Coherent fraction for different apertures	93
Figure 6.11	Pointing stability of the FLASH beam	95
Figure 6.12	Fluctuations of beam diameter and divergence	96
Figure 6.13	Wigner distribution function of a Gaussian Schell-model beam	98
Figure 6.14	Setup for a 4D measurement of the Wigner distribution	100
Figure 6.15	Intensity profiles of different TEM modes	103
Figure 6.16	Wigner distribution functions of Hermite-Gaussian beams in theory and experiment	104
Figure 6.17	Wigner distribution function of non-separable beam in theory and experiment	105

LIST OF TABLES

Table 4.1	Particle density ahead and after the barrel shock	60
Table 4.2	Comparison of plasma emission characteristics without and with barrel shock	63
Table 5.1	HHG beam parameters derived from intensity profiles and wavefront	73
Table 6.1	Beam propagation parameters of FLASH	86
Table 6.2	Coherence parameters of FLASH	91
Table 6.3	Coherence parameters of FLASH for various sizes of apertures	93
Table 6.4	Beam parameters of a synthetic Gaussian Schell-model beam	99
Table 6.5	Coherence of TEM beams in theory and experiment	105

SYMBOLS

Symbol	Unit	Description
A, B, C, D	$-, m, -, m^{-1}$	2x2 propagation matrices
A	m^2	Area
B	T	Magnetic field strength
Br	$s^{-1} mm^{-2} mrad^{-2}$	Brilliance
D	-	Linear dispersion
E	$V m^{-1}$	Electric field strength
E_{kin}	J	Kinetic Energy
\mathcal{F}	-	Fourier transformation
I	$W m^{-2}$	Intensity
I_p	J	Ionization potential
K	-	Global degree of coherence
K_u	-	Undulator parameter
L_g	m	Gain length
M	-	Mach number
M_x^2	-	Beam quality factor
\mathcal{M}	-	Beam matrix
N	m^{-3}	Particle density
N_{ph}	-	Number of photons
P	W	Power
R_s, R_t	m	Sagittal and tangential radius
R_{sp}	$J kg^{-1} K^{-1}$	Specific gas constant
R_∞	m^{-1}	Rydberg constant
\mathcal{S}	-	4x4 propagation matrix
\vec{S}_\perp	-	Normal. transverse Poynting vector
S_{sh}	-	Shielding constant
T	K	Temperature
U_p	J	Ponderomotive potential
V	J	Binding potential
Z	-	Zernike polynomial
Z_{at}	-	Atomic number

Symbol	Unit	Description
a, b	m	Plasma diameter (FWHM)
a_0	m	Ponderomotive radius
c	m s^{-1}	Speed of light
d	m	Diameter
d_0	m	Waist diameter
e	C	Electron charge
\hbar	J s	Planck's constant
f	m	Focal length
g	m^{-1}	Groove density
h	$\text{W m}^{-2} \text{rad}^{-2}$	Wigner distribution function
j_u, j_v	rad^{-1}	Reciprocal angular coordinates
k	m^{-1}	Wave number
l	m	Distance or length
m	-	Diffraction order
m_e	kg	Electron mass
n	-	Refractive index
n_e	m^{-3}	Electron density
p	N m^2	Pressure
q_u, q_v	m^{-1}	Reciprocal spatial coordinates
r	m	Radius of source flow
s_x, s_y	m	Spatial distance coordinates
t	s	Time
u, v	rad	Angular coordinates
\bar{v}_z	m s^{-1}	Mean longitudinal velocity
w	m	Wavefront
x, y, z	m	Spatial coordinates
z_0	m	Waist position
z_R	m	Rayleigh length

Symbol	Unit	Description
α	rad	Incidence angle
β	rad	Deflection angle
Γ	W m^{-2}	Mutual coherence function
γ	-	Complex degree of coherence
γ_K	-	Keldysh parameter
γ_L	-	Lorenz factor
ϵ	-	Eccentricity
ϵ_0	F m^{-1}	Vacuum permittivity
Θ	rad	Azimuth angle
θ	rad	Divergence angle
κ	J K^{-1}	Boltzmann constant
λ	m	Wavelength
ξ	$\text{N m}^{-1} \text{K}^{-1}$	Rarefaction parameter
ρ	kg m^{-3}	Density
σ	m	Standard deviation
τ	s	Time scale
ϕ	rad	Rotation angle
φ	rad	Phase shift
χ	-	Heat capacity ratio
Ω	rad^2	Solid angle
ω	s^{-1}	Angular frequency
ω_p	s^{-1}	Plasma frequency

ACRONYMS

Acronym	Description
BL	Beamline
CCD	Charge-coupled device
CDI	Coherent diffractive imaging
EUV	Extreme ultraviolet
FEL	Free-electron laser
FLASH	Free-electron laser in Hamburg
FWHM	Full width at half maximum
HHG	High-harmonic generation
IR	Infrared
LPP	Laser-produced plasma
MCF	Mutual coherence function
PMMA	Poly(methyl methacrylate) - acrylic glass
SASE	Self-amplified spontaneous emission
TEM	Transverse electromagnetic mode
UV	Ultraviolet
WDF	Wigner distribution function

COLOR SCALES

The following color scales are employed for the representation of two-dimensional distributions. Each scale is applied in a specific context as described below.

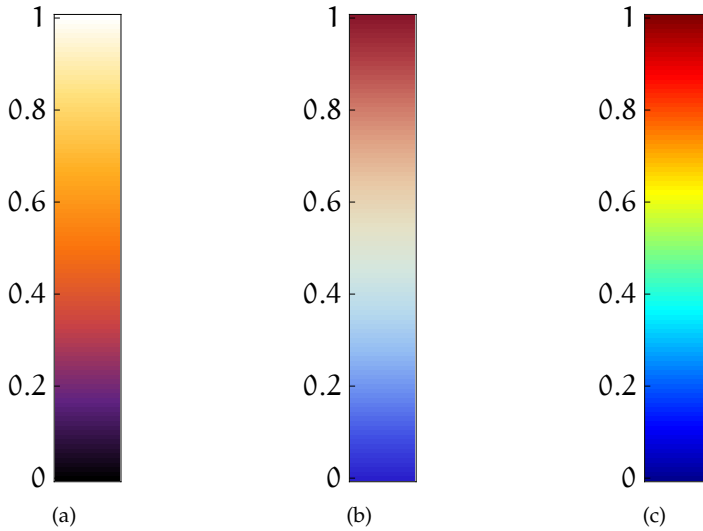


Figure 0.1: Color scales employed in this work. Scale (a) is applied to depict irradiance profiles, scale (b) visualizes the height of wavefronts and scale (c) is used to illustrate Wigner and coherence distributions.

INTRODUCTION

In the electromagnetic spectrum, extreme ultraviolet (EUV) and soft x-ray radiation is found between UV light and hard x-rays. Photons of this spectral region have very small absorption lengths in all kinds of material due to the strong interaction with matter. This fact together with the short wavelengths qualify this radiation as a tool for structuring and the analysis with nanometer resolution.

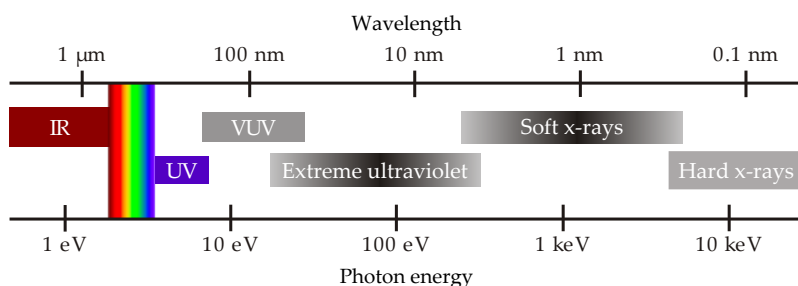


Figure 1.1: Electromagnetic spectrum from the infrared to the hard x-ray range. Adapted from [1].

An important application is the next-generation lithography which further reduces the achievable feature size in computer chip production [2, 3]. Surface analysis becomes extremely precise by means of reflectometry and scatterometry [4, 5, 6] and also the binding state of molecules can be studied by spectral investigations [7, 8, 9]. Microscopy with radiation at wavelengths in the water window ($\lambda = 2.3 \dots 4.4 \text{ nm}$) allows highly resolved direct imaging of samples in aqueous environment [10, 11, 12]. With coherent diffractive imaging (CDI) it is even possible to reconstruct the molecular structure of proteins and viruses [13, 14, 15]. Finally, ptychography is a diffraction based technique that serves to image larger samples such as biological cells in both, amplitude and phase contrast [16, 17].

Mostly, these applications are realized at the large scale facilities, such as synchrotron sources or free-electron lasers (FELs). However, the demand for beam time is always too large to be satisfied by these institutions and thus, people endeavor to transfer experiments to their laboratories. This constitutes the need of compact beam sources, as can be realized by the principle of laser-produced plasmas (LPP) or high-harmonic generation (HHG). These systems

are much more affordable but provide a significantly lower brilliance. In order to acquire a sufficient number of photons on the sample anyway, the efficiency of both, photon generation and beam guidance needs to be at an optimum. The diffraction based imaging techniques further require the photon beam to be fully coherent. These three properties, *beam generation*, *transport* and *coherence* are subject of this work and will be addressed employing both, compact and large scale beam sources.

Beam transport and coherence can strongly affect the focusing properties of the generated photons. An illustration of that effect is given in figure 1.2, where the intensity profile of an EUV beam is simulated at its mean focus position. In sub-figure (a), propagation parameters are employed as found for the photon beam of the free-electron laser FLASH. As it will be discussed in detail in chapter 6, a moderate astigmatic aberration is contained and the global degree of coherence is relatively low. Easily, the beam transport can be optimized by an alignment of the focusing optic, leading to a significant reduction of the beam diameter, as apparent in sub-figure (b). If additionally, the beam would be fully coherent as in sub-figure (c), the same amount of photons would be concentrated into a much smaller focus. This is one aspect that establishes the need to characterize and ideally, to control those beam properties.

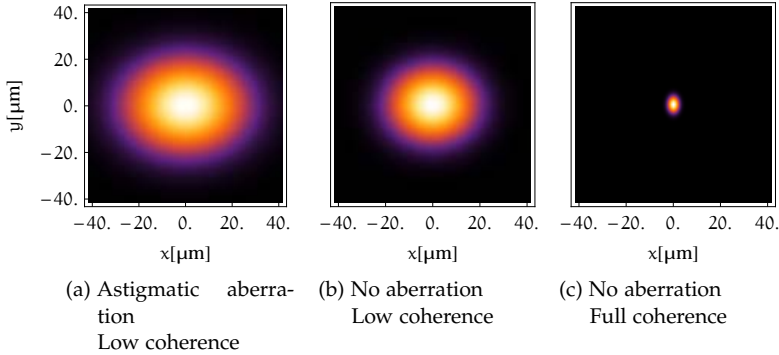


Figure 1.2: Influence of beam aberrations and coherence on focusing properties: (a) shows an intensity profile at mean focus position with parameters as found for FLASH, (b) results if the astigmatic waist difference vanishes and (c) follows if additionally, the global degree of coherence is raised to unity.

BEAM GENERATION In a first part, the brilliance of a laser-produced plasma is enhanced for gaseous target concepts. In contrast to solid or liquid target materials, these sources are clean and versatile but provide a comparably low conversion efficiency of laser energy into EUV and soft x-ray radiation. The basic idea is to induce supersonic effects in the gas jet leading to a local increase of the particle density and thus, to a larger number of emitters.

Typically, the target gas is expanded into a vacuum environment and the density drops rapidly in all directions. In order to weaken this density loss, there exist strategies to laterally guide the target gas by a concentric jet [18]. Ideally, here another atomic species is employed which shows weak absorption of the generated soft x-rays such as, for example, helium.

In the present approach, a low pressure helium atmosphere is used to generate shock waves in the supersonic nozzle flow. As a consequence, the so-called *barrel shock* evolves which is terminated in axial direction by the *Mach disc*, a practically normal shock [19]. Passing through these structures, the target gas is recompressed, and the particle density is raised. Focusing the laser beam into this region, a higher number of gas atoms can be ionized resulting in a brighter and smaller plasma.

After a discussion of the underlying gas dynamics in section 2.1.2, the jet is characterized experimentally by Schlieren imaging and wavefront measurements in chapter 4. The resulting effect on the plasma is observed by a pinhole camera, and the increased source brilliance is quantified by a diode measurement.

BEAM TRANSPORT In chapter 5, the EUV beam transport within the experimental arrangement of an HHG source is studied. In that case, a toroidal grating combines spectral filtering and focusing in order to produce a small individual spot for each harmonic. The highest possible EUV intensity at sample position is achieved if the beam is free from aberrations. Thus, the alignment of the optic plays a major role.

Here, the effect of small deviations from perfect alignment is investigated. A simple theoretical description of low order aberrations is found employing optical matrix methods. Experimentally, this is confirmed by a Hartmann sensor that captures the EUV wavefront of the aberrated beam. A scan of intensity profiles serves as an additional cross-check. During online measurement of the wavefront, the toroidal grating is subjected to an adjustment procedure. This way, the beam power is concentrated in the smallest focal spot diameter and the EUV intensity is maximized.

BEAM COHERENCE The spatial coherence of the EUV beam generated by the free-electron laser FLASH is discussed in the third part. This property of FEL radiation is of particular interest since full coherence throughout the sample is demanded by many experiments, such as coherent diffractive imaging or ptychography [20]. However, recent studies have shown that successful CDI results could be achieved even with less coherent beams in case that the mutual coherence function is known [21, 22].

The spatial coherence properties of free-electron lasers are addressed in many publications employing Young's double pinhole experiment [23], speckle statistics [24] or Hanbury Brown-Twiss interferometry [25]. However, in these studies a comprehensive characterization of the four-dimensional mutual coherence function is only possible if the FEL beam follows the Gaussian Schell-model. The complicated structure of the intensity profiles, as observed at FLASH, questions that assumption.

Here, the formalism of the Wigner distribution function provides an approach which is free from simplifications. As the Fourier transform of the mutual coherence function, it can simply be transferred into the latter and all spatial coherence parameters of interest can be derived. Experimental access is provided by measuring intensity profiles of the focused FEL beam at several positions. A tomographic reconstruction algorithm then yields the four-dimensional Wigner distribution function.

After an introduction of the Wigner formalism in section 3.4 the experiment at the free-electron laser FLASH is described in chapter 6 followed by a discussion of the results. Since the present setup scans a three-dimensional sub-manifold of the four-dimensional phase space only, some aspects of the beam might be missed, such as the twist term. It is shown that replacing the fixed angle focusing mirror with a rotatable toroidal mirror, the entire phase space of the beam becomes accessible. The principle is demonstrated for several modes of an IR laser.

As a theoretical basis of this work, chapter 3 gives an introduction in the field of beam characterization. Prior to this, the fundamentals of EUV and soft x-ray beam generation are discussed in chapter 2, primarily with respect to the investigated sources.

Our sun is likely to be the most prominent source of EUV and soft x-ray radiation. However, these photons don't reach us on earth due to their strong absorption by the atmosphere and thus, they are under investigation in satellite missions since 1959 [26, 27]. Today, the sun is continuously imaged by the "Extreme ultraviolet Imaging Telescope" [28] at four different EUV wavelengths uncovering the dynamics of different ionization states of iron and helium [29].

Also on earth, EUV and soft x-ray radiation is of great scientific interest and enables groundbreaking industrial applications, as discussed in the introduction. Thus, different beam sources covering that wavelength range have been developed in the last few decades.

In 1895, W. C. Röntgen produced hard x-rays for the first time employing a cathode ray tube [30]. Today, with modified x-ray tubes it is possible to produce EUV radiation, too [31]. Also synchrotrons, initially intended as particle colliders, emit radiation in a broad spectral range (from hard x-rays to the IR). The mechanism is based on the radial acceleration of charged relativistic particles which is caused by bending magnets [32]. The second generation of synchrotron light sources increased the photon yield by the wiggler which forces the particles to follow sinusoidal trajectories. In the third generation, the amplitude of the transversely oscillating particles is reduced by the undulator [33] and the emerging photon beam interacts with the charged particle cloud. Here, the undulator period defines a certain resonant wavelength and the spectral purity of the emitted radiation increases.

The described synchrotron light sources represent large scale facilities. An example of a compact soft x-ray and EUV beam source is given by the x-ray laser. Its realization is a peculiar challenge due to the lack of appropriate mirrors to build a resonator [34, 35]. As active medium it employs a highly ionized plasma which can be generated by a capillary discharge or by an optical laser pulse focused onto a solid target. While first devices provided radiation with a relatively poor coherence [36], nowadays this issue is overcome and diffraction limited beams in the EUV and soft x-ray range are generated [37, 38]. Still, these systems are rather complex and their availability is limited to a few research groups only.

In contrast, compact beam sources based on laser-produced plasmas (LPP) and high harmonic generation (HHG) are commonly

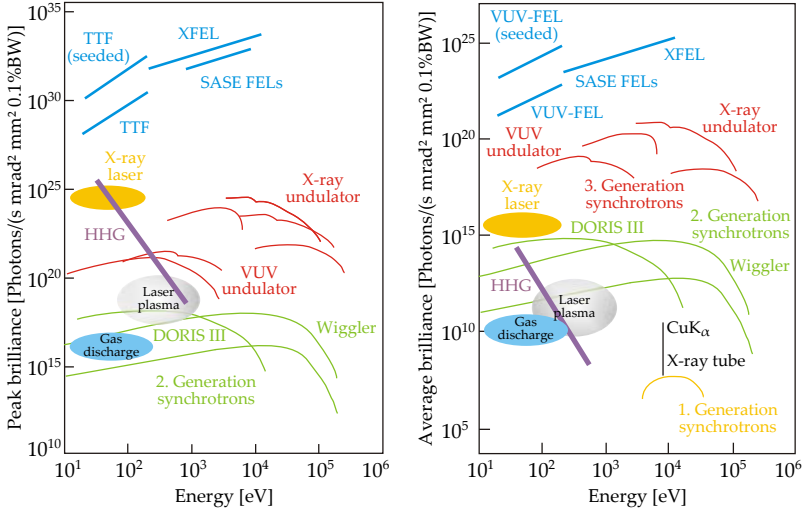


Figure 2.1: Classification of EUV and soft x-ray sources according to their brilliances and the photon energy. Adapted from [1].

used. As they are relevant for this work, the principle of these sources will be discussed in more detail in the following subsections. Furthermore, the concept of a free-electron laser (FEL) will be described particularly since this large scale facility represents the basis for the coherence measurements of chapter 6.

In order to classify and compare the radiation of soft x-ray and EUV beam sources, the brilliance Br is a commonly used quantity which is the number N_{ph} of photons within a narrow spectral range $\Delta\lambda/\lambda$ emitted into a solid angle Ω from an area A within the time scale τ (typically the wavelength range $\Delta\lambda$ is defined to be 0.1% of the central wavelength λ) [1]

$$Br = \frac{N_{ph}}{\tau \cdot A \cdot \Omega \cdot \Delta\lambda/\lambda}. \quad (2.1)$$

The value of Br is given in the unit $1/(\text{s} \cdot \text{mm}^2 \cdot \text{mrad}^2 \cdot 0.1\% \text{BW})$ with 0.1%BW indicating the bandwidth of 0.1%. A distinction is made between the peak brilliance, where τ denotes the pulse duration and the average brilliance where τ is the inverse of the repetition rate. Figure 2.1 gives an overview of the discussed beam sources in terms of both, average and peak brilliance. Apparently, free-electron lasers produce most brilliant beams, followed by syn-

chrotrons of the third generation and the x-ray laser. The compact beam sources based on laser plasmas and high harmonic generation provide a comparably lower brilliance. However, in relation to synchrotrons of the second generation, their radiation is equally or even more brilliant.

2.1 LASER-PRODUCED PLASMA

A *hot dense plasma* emits a broad spectral range of electromagnetic radiation including EUV and soft x-ray wavelengths. This peculiar state of matter is found in the stars and, in laboratory scale, it can be generated by irradiating a target material with an intense laser beam. Since this can involve high particle energies of the order of keV and densities approaching those of solids, it is referred to as a hot dense plasma.

Solids, liquids and gases are used as target materials, whereas basically, the source brilliance scales with the density. Thus, with solids, the largest number of photons originating per volume can be achieved. Respective target materials are deposited on rotating cylinders [39] or quickly moving tapes [40] which provide repetition rates of up to 1 kHz. Prominent elements are gold or tin for the production of radiation at a wavelength of 13.5 nm which is applied in EUV lithography [41]. Furthermore, there are sources employing cold gases in a solid phase such as an argon filament which emits in the soft x-ray range 2...5 nm [42]. Achievable plasma sizes with solid targets are comparably small and of the order of several tens of μm (FWHM).

A plasma of similar brilliance and extent is obtained with liquid targets, e.g., xenon [43], methanol [44] or tin [41]. A fluid jet [45] provides high target densities but might lead to size and brightness fluctuations. Going one step further to individual microscopic droplets [46], the advantage is the mass limitation such that the entire target material is converted into a highly ionized plasma state supporting source stability.

However, the disadvantage of solid and liquid target concepts is the inevitable production of fast particles and ions with kinetic energies of up to several hundred keV [47] which severely damage optics in the beam path. There are mitigation strategies to slow down the debris material like repeller fields [48] or localized gas jet shields [49] but still, collector optics have a limited lifetime [2].

Contrarily, gaseous targets are almost free from debris [18]. Short gas pulses with durations of μs ...ms are expanded from a pressure of several 10 bar into vacuum by a piezo-mechanical or electromag-

netic nozzle, resulting in a supersonic jet. Different target gases feature individual spectra of the resulting radiation, ranging from emitters with characteristic spectral lines (low atomic number, e.g., nitrogen) to broadband emitters (high atomic number, e.g., xenon) [50]. However, here, the conversion efficiency from laser energy into EUV and soft x-ray energy is comparably low due to the low density of the target material. Furthermore, achievable plasma sizes of several 100 μm are large. For metrology or scientific applications though, these sources are very attractive due to their high cleanliness and versatility [51, 8].

2.1.1 Physical properties of a plasma

Initially, the laser beam that irradiates the target material creates ions by multiphoton absorption, tunneling or field ionization [52]. The resulting free electrons are accelerated by the strong electric field leading to inverse bremsstrahlung and avalanche ionization. A hot dense plasma state is generated. In competition to the heating processes, deionization takes place in terms of diffusion and recombination [52]. Depending on the electron temperature, a continuum of electromagnetic radiation is produced due to bremsstrahlung and recombination of free electrons with ions. Additionally, bound-bound transitions within the ions contribute narrow lines to the emission spectrum. A corresponding scheme is depicted in figure 2.2.

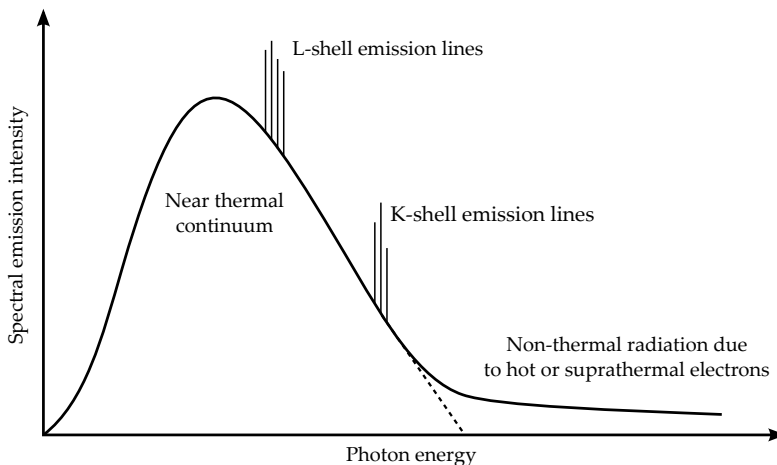


Figure 2.2: Scheme of the emission spectrum of a hot dense plasma [1].

The thermodynamics within a hot dense plasma can be approximated by the idealized state of a *thermal* plasma which is characterized by a single electron temperature T and a corresponding Maxwell velocity distribution. Within that simplification the plasma may be treated as a blackbody that emits radiation with a continuous spectrum. The assumption that photons are emitted carrying discrete quanta of energy, with energy proportional to frequency, leads to the spectral energy density [1]

$$\text{Br} = 3.146 \cdot 10^{11} \left(\frac{\kappa T}{\text{eV}} \right)^3 \frac{(\hbar\omega/\kappa T)^3}{e^{\hbar\omega/\kappa T} - 1} \frac{\text{photons/s}}{\text{mm}^2 \text{mrad}^2 (0.1\% \text{BW})}, \quad (2.2)$$

here, given in units of the brilliance with Planck's constant \hbar and the photon frequency ω . Typical electron temperatures for gas targets irradiated by nanosecond laser pulses are 20 eV ... 200 eV [53, 54]. Corresponding spectral maxima of the Planck distribution are found at the photon wavelengths 2.2 ... 22.0 nm with peak brilliances of $3.6 \cdot 10^{15} \dots 3.6 \cdot 10^{18} (\text{s mm}^2 \text{mrad}^2 0.1\% \text{BW})^{-1}$.

In fact, a laser-produced plasma is far away from thermodynamic equilibrium and a *thermal* plasma rather is an upper limit for the spectral power density. However, mostly a two-temperature model is already sufficient to adequately describe the continuum radiation by a hot dense plasma which is then called *near-thermal* plasma [1]. Additionally to the thermal electrons a suprathermal component is introduced which is raised by non-linear interactions such as resonant absorption. When these electrons undergo bremsstrahlung or recombination they give rise to a high photon energy tail in the emission spectrum as indicated in figure 2.2.

Line radiation is emitted when electrons change their energy state within an ion from an outer to an inner electron shell. The resulting photon energy corresponds to the transition energy of the electron as described by Moseley's law which is an extension of the Rydberg formula [55]

$$\frac{1}{\lambda} = \frac{R_{\infty}}{1 + m_e/m_{\text{nuc}}} (Z_{\text{at}} - S_{\text{sh}})^2 \left(\frac{1}{n_1^2} - \frac{1}{n_2^2} \right) \quad (2.3)$$

with the Rydberg constant R_{∞} , the nuclear mass m_{nuc} and the atomic number Z_{at} . The constant S_{sh} describes the shielding due to electrons between the core and the considered electron. Furthermore, n_1 and n_2 are the principal quantum numbers of initial and final state of the electron. In plasmas of species with low atomic

numbers like nitrogen ($Z_{\text{at}} = 7$), comparatively few free electrons are produced and the emitted radiation is dominated by single spectral lines. In contrast, elements with high atomic numbers like xenon ($Z_{\text{at}} = 54$) yield much more free electrons, resulting in a spectrum of numerous closely packed lines and a significant thermal contribution.

Another important plasma parameter is the electron plasma frequency [1]

$$\omega_p = \left(\frac{e^2 n_e}{\epsilon_0 m_e} \right)^{1/2} \quad (2.4)$$

at which the free electrons tend to oscillate (e is the electron charge, n_e the electron density, m_e the electron mass and ϵ_0 the vacuum permittivity). As a consequence, an incident electromagnetic wave can propagate in the plasma only if its frequency ω is greater than ω_p and it is totally reflected if $\omega = \omega_p$. This yields a critical electron density [1]

$$n_c = \frac{\epsilon_0 m_e \omega^2}{e^2} \quad (2.5)$$

which is $n_c = 1 \cdot 10^{21} \text{ cm}^{-3}$ for a common Nd:YAG laser beam with the wavelength 1064 nm. Thus, when the plasma reaches the critical electron density it can not further be heated what poses a limit especially for solid and liquid target concepts. In order to mitigate that limitation, a less intense pre-pulse can be used to heat the target material and decrease its density precedent to the main pulse [56].

2.1.2 Gas dynamics of jet targets

Supersonic gas jets employed as targets inherently exhibit strong density gradients. Here, the basics of supersonic nozzle flows and related shock phenomena are described theoretically, mainly based on [57, 58]. As a result, density estimations of the target gas are provided corresponding to the experimental situation at a laser plasma source.

Let us first consider the example of a compressible fluid that expands through a convergent-divergent nozzle, a so-called *de Laval* nozzle as shown schematically in figure 2.3. In gas dynamics, the basic equations to describe that problem are the conservation laws

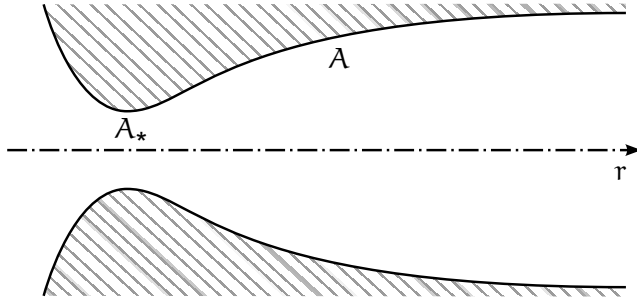


Figure 2.3: Sketch of a de Laval nozzle. A denotes the local cross sectional area with the minimum value A_* at throat position.

of mass and energy, formulated for compressible and isentropic flows. It can be shown that these relations lead to the well-known area relation between the local cross sectional area A , the throat area A_* and the local Mach number M [58]

$$\frac{A}{A_*} = \frac{1}{M} \left[\frac{2}{\chi+1} \left(1 + \frac{\chi-1}{2} M^2 \right) \right]^{\frac{\chi+1}{2(\chi-1)}}. \quad (2.6)$$

Here, $\chi = c_p/c_v$ is the ratio of specific heats (c_p at constant pressure and c_v at constant volume) and the Mach number M is defined as ratio between the local flow velocity and the local speed of sound. In the present example of a convergent-divergent nozzle, a gas is accelerated in the convergent part according to the continuity equation. If the critical Mach number $M_* = 1$ is reached at the throat this results in supersonic velocities $M > 1$ in the divergent part, and the thermal energy of the gas is efficiently converted into directed kinetic energy. Concurrently, the gas density decreases according to the relation [57]

$$\frac{\rho}{\rho_0} = \left(1 + \frac{\chi-1}{2} M^2 \right)^{-\frac{1}{\chi-1}}. \quad (2.7)$$

The shape of the cross sectional area A/A_* of a typical de Laval nozzle is depicted in figure 2.4 together with the resulting distribution of density ρ/ρ_0 (ρ_0 stagnation density) and Mach number M under the assumption of a diatomic gas with $\chi = 7/5$.

Utilizing a supersonic gas jet as a target for laser-produced plasmas requires large particle densities for high conversions efficiencies of laser energy into EUV or soft x-ray energy. Thus, a compromise needs to be found between a directed, but rarefied flow

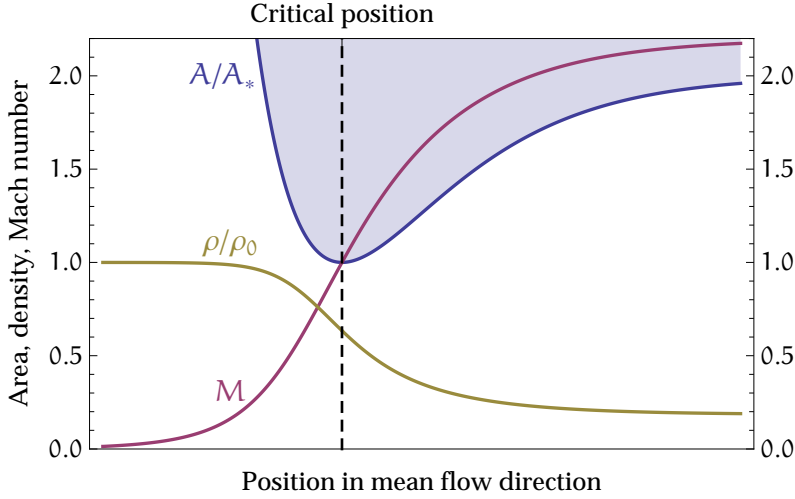


Figure 2.4: State functions of a flow in a de Laval nozzle: density ρ in terms of its stagnation value ρ_0 , Mach number M and the local cross sectional area A reaching A_* at its throat position. A diatomic gas with $\chi = 7/5$ is assumed.

at high Mach numbers and divergent but denser flow at low Mach numbers. This can be achieved by adapting the nozzle geometry [59].

Within this work, shock waves, as they can be observed in supersonic flows, are employed to further optimize the particle density in a jet target. Within very short distances on the order of the mean free path of the molecules, this phenomenon leads to an increase in density, pressure and temperature while the Mach number decreases. Based on the conservation laws of mass, momentum and energy it is possible to derive equations that relate the initial values of those properties with the conditions right behind a shock wave. Here, it is sufficient to consider the change of the initial density ρ and Mach number M in case of a normal shock relative to the flow direction. After passing through the shock structure these properties are denoted as $\hat{\rho}$ and \hat{M} , as indicated in figure 2.5. The corresponding shock relations read [57]

$$\frac{\hat{\rho}}{\rho} = \frac{(\chi + 1)M^2}{2 + (\chi - 1)M^2} \quad (2.8)$$

$$\hat{M} = 1 - \frac{M^2 - 1}{1 + \frac{2\chi}{\chi + 1}(M^2 - 1)}. \quad (2.9)$$

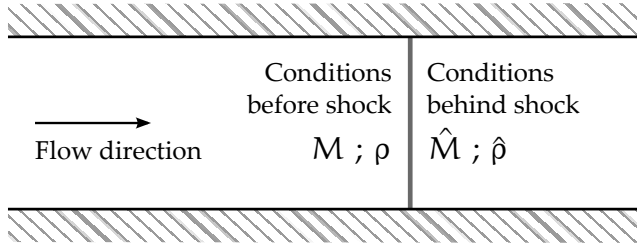


Figure 2.5: Normal shock structure in a supersonic flow. Gas passing through the shock experiences a decrease from the initial Mach number M to \hat{M} and an increase in density from ρ to $\hat{\rho}$.

Basically, high Mach numbers lead to a strong compression of the fluid when passing through a shock. However, relation (2.8) defines an upper limit for the density ratio that can be achieved in connection with a shock wave. This limit is approached if $M \rightarrow \infty$ and, for diatomic gases, it is $\frac{\hat{\rho}}{\rho} \rightarrow 6$ ($\chi = 7/5$). At the same time, the Mach number behind the shock decreases to $\hat{M} \rightarrow 1/7$.

Shock waves appear, e.g., when obstacles perturb a supersonic flow or, vice versa, when objects travel with Mach numbers $M > 1$ through a gas at rest. In case of a supersonic jet that expands from a stagnation pressure p_0 into an atmosphere with a sufficiently large background pressure p_b , shock waves can be observed, too. At a certain distance to the nozzle exit, the collision between the jet particles and the surrounding gas particles leads to a shock structure which is called *barrel shock*, see figure 2.6. With respect to that situation, Muntz *et al* introduced the rarefaction parameter [60]

$$\xi = d_* \frac{\sqrt{p_0 \cdot p_b}}{T_0} \quad (2.10)$$

where d_* is the throat diameter of the nozzle and T_0 denotes the stagnation temperature. This parameter describes the interaction between jet and background particles, i.e., how strong the expansion flow is influenced by the surrounding gas. Muntz *et al* propose a differentiation of the occurring flow into three regimes [60]:

- Scattering regime $\xi \leq \xi_s$
Molecules of the background gas interact with the freely expanding jet by diffusion only, no distinct shock waves evolve.
- Transition regime $\xi_s < \xi < \xi_c$
Thick lateral shock waves develop and confine an undisturbed core of the jet which is surrounded by a mixing zone of jet and background particles.

- Continuum regime $\xi_c \leq \xi$

The fully evolved barrel shock structure is present, as shown in figure 2.6. The inner barrel shock waves and the *Mach disk* spatially delimit the influence of the background gas.

In the continuum regime, the extent of the shock structure scales with the nozzle pressure ratio p_0/p_b . In particular, within the range $15 < p_0/p_b < 17000$ the distance $l_M = r_M - r_*$ between nozzle throat and Mach disk is given by [61]

$$l_M = 0.67 \cdot d_e (p_0/p_b)^{1/2} \quad (2.11)$$

where d_e is the exit diameter of the orifice. It should be noted that this relation has been derived for nozzles with a constant diameter, i.e., for a non-divergent geometry.

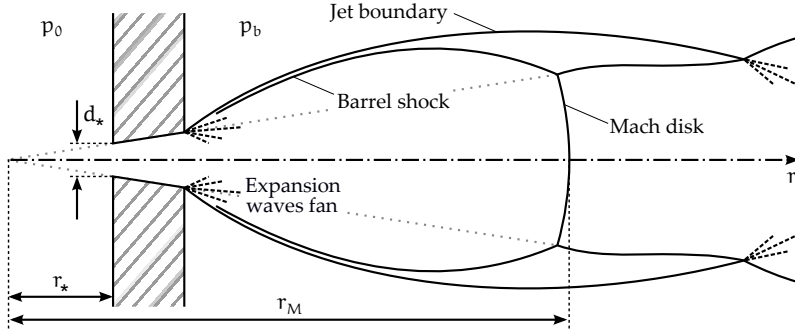


Figure 2.6: Typical structure of a barrel shock as apparent at supersonic jets in presence of a background gas. Here, a fluid is expanded from a high pressure p_0 through the conically diverging nozzle into an ambient atmosphere of relatively low pressure p_b . The depicted shock system represents the continuum regime. Adapted from [19].

In the following, estimations are made for a gas jet with barrel shock structures as it is under experimental investigation in this work, too. This reasoning has been published already [50].

Nitrogen expands from a pressure of $p_0 = 11$ bar into a helium atmosphere with a pressure of $p_b = 170$ mbar through a conically diverging nozzle (thickness $l_n = 1$ mm, throat diameter $d_* = 300\mu\text{m}$ and exit diameter $d_e = 500\mu\text{m}$). At rest, both gases are at room temperature $T_0 = 293$ K. In a simplification, a source flow is assumed corresponding to the dotted cone in figure 2.6 with its apex in a distance of $r_* = 1.5$ mm to the nozzle's throat. According to

equation (2.11) the Mach disk appears 2.7 mm behind the nozzle throat, i.e., $r_M = 4.2$ mm. The dimensionless area of the assumed source flow is expressed in terms of the distance r to the virtual source as $A/A_* = (r/r_*)^2$. Solving equations (2.6) and (2.7) results in the state functions ρ/ρ_0 and M along the symmetry axis of the nozzle from throat position to the Mach disk, i.e., in the range $1.5 \text{ mm} \leq r \leq 4.2 \text{ mm}$. The conditions directly behind the Mach disk are determined by the shock relations (2.8) and (2.9). For $r > 4.2 \text{ mm}$ the flow is assumed to be incompressible ($\rho = \text{const.}$) since the Mach number has decreased sufficiently below $M = 1$. Thus, subsequent behavior of M is approximated by the continuity equation $M(r) = \hat{M} \cdot (r/r_M)^2$.

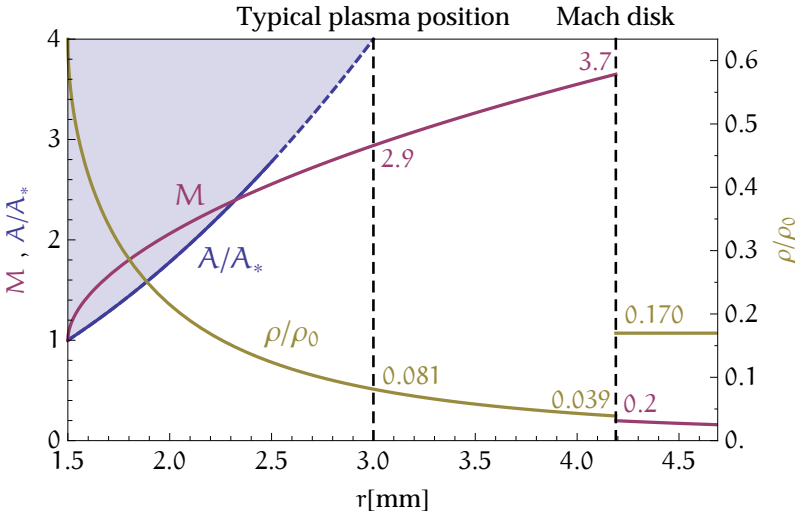


Figure 2.7: State functions along the symmetry axis of a barrel shock: density ρ in terms of its stagnation value ρ_0 , and Mach number M . The solid blue line for A/A_* represents the cross sectional area of the orifice whereas the dashed blue line indicates the subsequent conical source flow. Since this figure corresponds to the real experimental situation investigated in chapter 4, the length r is given in physical units.

The corresponding state functions $\rho(r)/\rho_0$ and $M(r)$ are depicted in figure 2.7 with respect to the distance r to the virtual source. Usually, the nozzle is operated with a background pressure on the order of $p_b \leq 10^{-4}$ mbar and the plasma is generated in a distance of $500 \mu\text{m}$ to the nozzle exit. The conditions at the usual plasma position, before and behind the Mach disk are given in the diagram. It is revealed that due to the shock, a two times higher density

is achieved in a larger distance to the nozzle as compared to the typical plasma position. In practice, the density increase is even higher since plasma production takes place a few 100 μm besides the symmetry axis of the nozzle. Here, without ambient gas the jet is even more rarefied and with ambient gas the shock structure is present.

2.2 HIGH-HARMONIC GENERATION

High-harmonic generation (HHG) refers to a process where a strong electromagnetic field at a frequency ω_0 is converted into integer multiples $n \cdot \omega_0$ due to a highly nonlinear interaction with a conversion medium [62]. Second-harmonic generation has already been demonstrated in 1961 [63] with a ruby laser beam ($\lambda = 694 \text{ nm}$) propagating through a quartz crystal resulting in UV light at a wavelength of 347 nm. In 1987, the seventeenth harmonic ($\lambda = 14.6 \text{ nm}$) of an excimer laser beam ($\lambda = 248 \text{ nm}$) has been generated by the HHG process with neon as conversion medium [64]. One year later, even the 33rd harmonic of an Nd:YAG laser has been observed [65]. An explanation of the observed processes was found by Corkum [66] and Kulander *et al.* [67] in 1993 in terms of a quasiclassical model, the so-called *three-step model*. Shortly afterwards, Lewenstein *et al.* found a fully quantum-mechanical description confirming the quasiclassical results [68]. Today, the shortest man-made electromagnetic pulses in the attosecond range are produced by the HHG process [69].

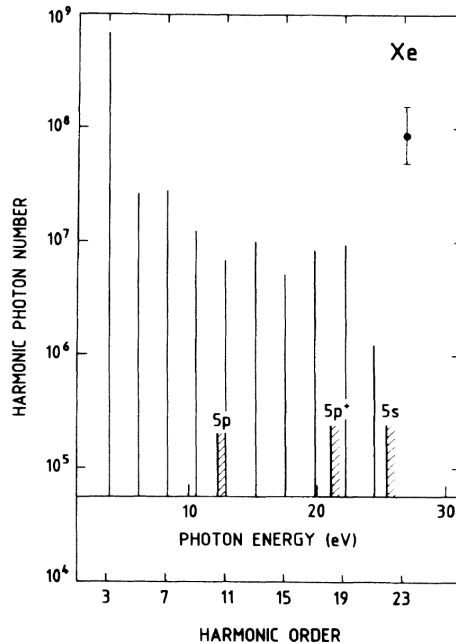


Figure 2.8: Typical HHG spectrum generated in Xe revealing odd harmonics of the fundamental wavelength $\lambda = 1064 \text{ nm}$ up to 21st order, taken from [70].

A typical HHG spectrum is shown in figure 2.8 revealing odd harmonics of the laser's fundamental frequency up to the 21st order. Three different spectral regions can be distinguished: the perturbative regime shaped by rapidly decreasing low-order harmonics, a plateau region with harmonics of equal intensity which ranges down to the cut-off wavelength, where the following harmonics quickly vanish.

In perturbation theory, the appearance of harmonics is explained by a multiphoton absorption. Within the scope of that process, the conversion efficiency decreases exponentially with the number of absorbed photons, standing in contradiction to the observed plateau region. Here, the three-step model proposes a different mechanism, which results in the generation of equally intense harmonics terminated by a cut-off wavelength. In the following, the three steps of this model are discussed in detail, i.e., ionization, propagation and recombination.

2.2.1 The three-step model

2.2.1.1 Step I: Ionization

First step in the HHG process is the generation of a free electron by ionization. Three different scenarios are possible: multiphoton absorption, tunneling through a potential barrier and barrier-suppressed ionization as indicated in figure 2.9. These mechanisms depend on the electromagnetic field $E(t) = E_0 \cos(\omega t)$ of the incident laser pulse which deforms the Coulomb potential of the atom, i.e., the binding potential sensed by the electron

$$V(\vec{r}, t) = -\frac{e^2}{4\pi\epsilon_0 r} + e\vec{E}(t) \cdot \vec{r}. \quad (2.12)$$

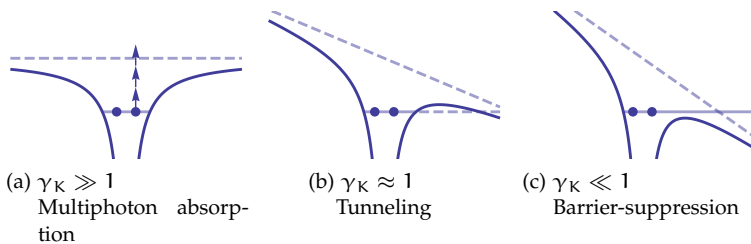


Figure 2.9: Ionization mechanisms depending on the Keldysh parameter γ_K .

The dominant ionization process is determined by the Keldysh parameter γ_K [71] which relates the ionization potential I_p of an electron to the ponderomotive potential U_p

$$\gamma_K = \sqrt{\frac{I_p}{2U_p}} \quad \text{with} \quad U_p = \frac{e^2 E_0^2}{4 m_e \omega^2}. \quad (2.13)$$

If $\gamma_K \gg 1$ the binding potential stays unperturbed and multiphoton absorption is the only possible ionization mechanism. For larger electromagnetic field strengths E_0 , the Keldysh parameter decreases to $\gamma_K \approx 1$ and the Coulomb potential becomes significantly deformed creating a finite potential barrier as shown in figure 2.9(b). Here, tunnel ionization is possible if the period $2\pi/\omega$ of the oscillating field is long compared to the tunnelling time. Shorter periods will lead to increasing γ_K and multiphoton ionization again. Even higher field strengths E_0 ($\gamma_K \ll 1$) further suppress the potential barrier below the ionization energy and the electron can classically escape the ion.

2.2.1.2 Step II: Propagation

After the ionization, the electron can be regarded as a free charged particle. Due to the oscillating homogenous electric field of the laser $E(t) = E_0 \cos(\omega t)$, it is accelerated by the force $F(t) = -eE(t)$ to the velocity $v(t) = \int_0^t -\frac{e}{m} E(t') dt' + v_0$. Taking into account that the ionization can happen at arbitrary phases φ and assuming a vanishing initial velocity $v_0 = 0$ at the ionization position $x_0 = 0$, the equations of motion are

$$\begin{aligned} v(t) &= -\frac{E_0 e}{m_e \omega} [\sin(\omega t + \varphi) - \sin(\varphi)] \\ x(t) &= -\frac{E_0 e}{m_e \omega^2} [\cos(\omega t + \varphi) - \cos(\varphi) + \sin(\varphi) \cdot \omega t], \end{aligned} \quad (2.14)$$

where $x(t)$ denotes the spatial coordinate. The ponderomotive potential U_p introduced in equation (2.13) results from the mean kinetic energy $\bar{E}_{\text{kin}} = \frac{1}{2} m_e \cdot \frac{2\pi}{\omega} \int_0^{2\pi/\omega} v(t)^2 dt$ of an electron which is ionized at phase $\varphi = 0$. Another characteristic quantity is the ponderomotive radius

$$a_0 = \frac{E_0 e}{m_e \omega^2} \quad (2.15)$$

with typical values on the order of a few nanometers (for an electromagnetic field with $\lambda = 800$ nm and $I = 10^{16}$ W/cm²).

Figure 2.10 shows trajectories $x(t)$ for electrons which are born at different phases φ of the electromagnetic wave. Apparently, φ plays a major role: while at very small phases $\varphi \approx 0$, the electron stays close to the ion, for increasing φ it quickly propagates away in space. However, in most cases (except $\varphi = 0.5\pi$) the electron recollides at least once with the ion leading to an eventual recombination and photon emission.

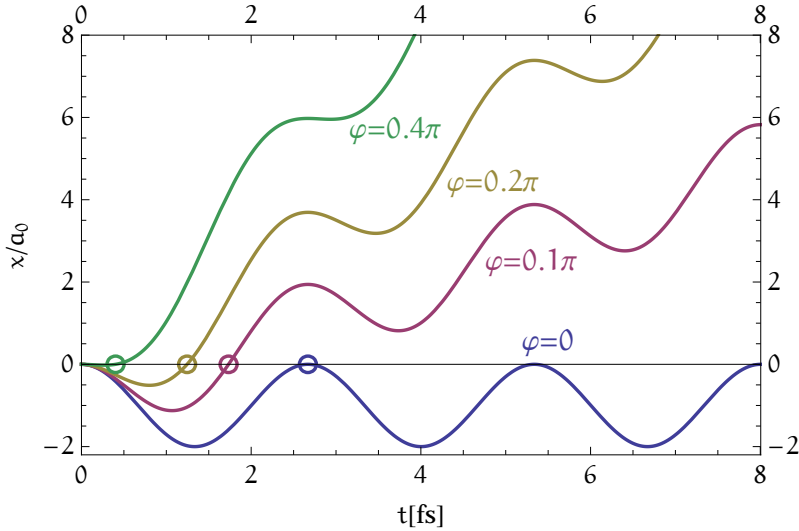


Figure 2.10: Trajectories of electrons which are ionized at time $t = 0$ at different phases φ of the accelerating laser pulse ($\lambda = 800$ nm). The ponderomotive radius a_0 is employed for scaling. Recollisions with the parent ion are indicated by circles.

2.2.1.3 Step III: Recombination

When the electron happens to recombine with the parent ion, it generally emits a photon carrying the kinetic energy of the electron E_{kin} at the moment of recollision plus the ionization energy I_p

$$\hbar\omega = E_{\text{kin}} + I_p. \quad (2.16)$$

As it is evident in figure 2.10, after ionization at $t = 0$ the duration t_0 until possible recombination becomes shorter with increasing φ . More importantly, the slope of the trajectories at t_0 varies with φ ,

i.e., the kinetic energy of the electron. This relation is illustrated in figure 2.11 which is derived as follows: The numerical solution of the equation $x(t_0) = 0$ for various phases φ yields the recollision time $t_0(\varphi)$ after ionization. Subsequently, the current kinetic energy $E_{\text{kin}} = \frac{1}{2}m_e v(t_0)^2$ is derived. A maximum value of $E_{\text{kin}} = 3.17 U_p$ is found if the ionization happens at the phase $\varphi = 0.1\pi$ of the driving electromagnetic field. Thus, the highest energy that can be expected for a photon resulting from recombination is

$$\hbar\omega_c = 3.17 U_p + I_p \quad (2.17)$$

corresponding to a cut-off wavelength λ_c , as observed in the experimental spectra.

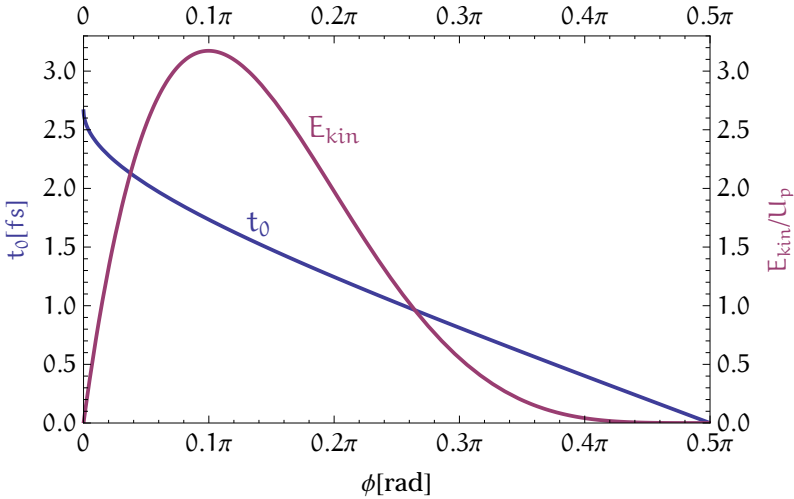


Figure 2.11: Kinetic energy E_{kin} of an electron at recollision with the ion and recollision time t_0 after ionization, both depending on the phase φ of the laser field when the free electron is born. The maximum energy value $3.17 U_p$ is reached at a phase of 0.1π .

2.2.2 Spectral properties of HHG radiation

So far, the spectral plateau region terminated by a cut-off wavelength could well be explained. Now, the appearance of discrete integer multiples of the driving frequency $\omega_0 = 2\pi/T_0$ is derived by considering a particle ensemble in a many cycle electromagnetic field. Two different classes of conversion media are distinguished:

- Inversion symmetry

The production of photons with a specific energy occurs repetitively in cycles with a duration of $T_0/2$. In Fourier space, such a process exhibits a discrete spectrum with a frequency separation of $\Delta\omega = 2\pi/(T_0/2) = 2\omega_0$. Now consider two photons which have been generated with a time difference $T_0/2$. They annihilate each other due to destructive interference. In contrast, a time difference T_0 leads to constructive interference. Thus, the lowest frequency of the HHG spectrum is $\omega_0 = 2\pi/T_0$ and it follows

$$\omega = (2n - 1) \cdot \omega_0 \quad \text{with} \quad n = 1, 2, 3, \dots$$

- Broken inversion symmetry

On the contrary, a broken inversion symmetry of the conversion medium leads to the generation of even *and* odd multiples of the fundamental frequency since the photon production repeats every *full* laser cycle, i.e.,

$$\omega = n \cdot \omega_0 \quad \text{with} \quad n = 1, 2, 3, \dots$$

2.3 FREE-ELECTRON LASER

From classical electrodynamics it is known that the acceleration of charged particles leads to the emission of electromagnetic radiation [72, 73]. In a free-electron laser (FEL) relativistic electrons propagate in an oscillating motion through a periodic magnetic field, thus generating a photon beam. Particularly, the interaction between the initially incoherent photon beam and the electron beam causes the so-called *microbunching* within the electron cloud and as a consequence, coherent radiation becomes amplified. This physical process is referred to as *self-amplified spontaneous emission* (SASE) and will be discussed in more detail after a brief review of the history of FEL development.

The undulator which provides the periodic magnetic structure has been investigated theoretically [74] and experimentally [33] in the early fifties as a source for visible light and microwave radiation. In 1977, the first free-electron laser emitted coherent light from an undulator arrangement in combination with an optical resonator [75, 76]. In the following decades, efforts have been made to increase photon energies into the UV and soft x-ray range [77, 78] reaching the hard x-ray regime in 2009 [79]. Today, FELs deliver pulses with durations of a few femtoseconds and peak powers on the order of 10^{10} W at wavelengths down to 1 \AA [80], i.e., the most brilliant radiation in the EUV and soft x-ray range which is currently available. Since these facilities reach lengths of several hundred meters or even kilometers, present investigations aim to realize more compact and even table-top sized free-electron lasers [81, 82, 83].

2.3.1 Spontaneous undulator radiation

The scheme of an undulator is depicted in figure 2.12 as a top view together with the sinusoidal trajectory of an electron cloud emitting undulator radiation. In the following, the undulator equation is derived which defines resonance wavelengths depending on the electron's kinetic energy and the undulator parameter K_u [84, 85].

A photon emitted at a wave crest travels with the speed of light c while an electron propagates with the mean longitudinal velocity $\bar{v}_z < c$. At time $\tau = \lambda_u / \bar{v}_z$, when the electron reaches the next wave crest, the photon has traveled the distance $c \cdot \lambda_u / \bar{v}_z > \lambda_u$. In order to interfere constructively with the next emitted photon, the path difference between the first photon and the electron at time τ needs to be an integer multiple of the photon wavelength λ_p .

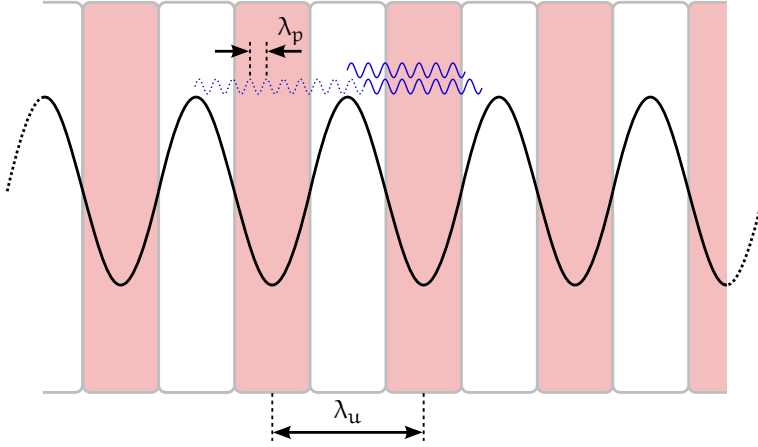


Figure 2.12: Schematic top view of an undulator with the trajectory of an electron (black) producing undulator radiation (blue).

The undulator radiation interferes constructively if the following condition is fulfilled

$$n \cdot \lambda_p = \lambda_u \left(\frac{c}{\bar{v}_z} - 1 \right) \quad \text{with } n = 1, 2, 3, \dots \quad (2.18)$$

Assuming that N_{ph} photons are generated with equal field strength E_0 but different relative phases φ_j , their total intensity is given by

$$I \propto \left| \sum_{j=1}^{N_{\text{ph}}} E_0 e^{i\varphi_j} \right|^2. \quad (2.19)$$

While for coherent light, i.e. $\varphi_j = n \cdot 2\pi$, the electric field strengths E_0 of N_{ph} photons add up to $E_{\text{coh}} = N_{\text{ph}} \cdot E_0$, for an incoherent superposition, i.e. random φ_j , this applies to the intensities $I_{\text{incoh}} = N_{\text{ph}} \cdot I_0$. Thus, the intensity of coherent radiation $I_{\text{coh}} \propto E_{\text{coh}}^2 \propto N_{\text{ph}}^2$ increases much stronger than the intensity of incoherent radiation $I_{\text{incoh}} \propto N_{\text{ph}}$ and photons which meet condition (2.18) will dominate the spectrum of the undulator radiation.

Formulating the condition for constructive interference in terms of Lorentz factor $\gamma_L = 1/\sqrt{1-v^2/c^2}$ and undulator parameter K_u

leads to the undulator equation [85] which specifies the fundamental resonant wavelength ($n = 1$)

$$\lambda_p = \frac{\lambda_u}{2\gamma_L^2} \left(1 + \frac{K_u^2}{2} \right) \quad (2.20)$$

with the dimensionless undulator parameter

$$K_u = \frac{e\lambda_u B_0}{2\pi m_e c}. \quad (2.21)$$

A deeper analysis reveals that only odd harmonics $n \cdot \lambda_p$ ($n = 1, 3, 5, \dots$) are emitted on-axis [86]. Equation (2.20) defines a Lorentz factor γ_L , i.e., a specific kinetic energy $E_{\text{kin}} = \gamma_L m_e c^2$ that an electron needs to emit coherent radiation with the wavelength λ_p .

Practically, the photon wavelength is controlled through γ_L by variation of the electron energy with the accelerator [87]. Much more quickly, λ_p can be influenced through a change of K_u by variation of B_0 with variable gap undulators [88]. Typical values of the free-electron laser FLASH are $K_u = 1.23$, $\lambda_u = 27.3$ mm and $E_{\text{kin}} = 1.2$ GeV which results in a fundamental wavelength of $\lambda_p = 4$ nm [89]. Lower electron energies allow tuning of the photon wavelength up to 45 nm. The European XFEL, currently under construction, will accelerate electrons up to 17.5 GeV extending the spectral range of the achievable radiation down to 0.1 nm [80].

2.3.2 High-gain FEL radiation

In the infrared and visible spectral range, an FEL can be equipped with an optical cavity such that a circulating electron beam spatially overlaps with the produced photon beam and the latter will accumulate more energy each cycle [90]. This way, an average FEL beam power of more than 10 kW is achievable at IR wavelengths [91].

However, in the EUV and soft x-ray spectral range, this scheme is not feasible due to the lack of appropriate mirrors to build a resonator. Here, the electron bunch can travel only once through the undulator. Thus, in order to produce a high power photon beam at these wavelengths, all available electrons need to emit coherently. This is the case if all electrons emit from the same position, or, if individual electrons are longitudinally separated by distances of the radiation wavelength. The latter situation appears due to the interaction between the produced electromagnetic radiation and the electron beam which is called *microbunching*.

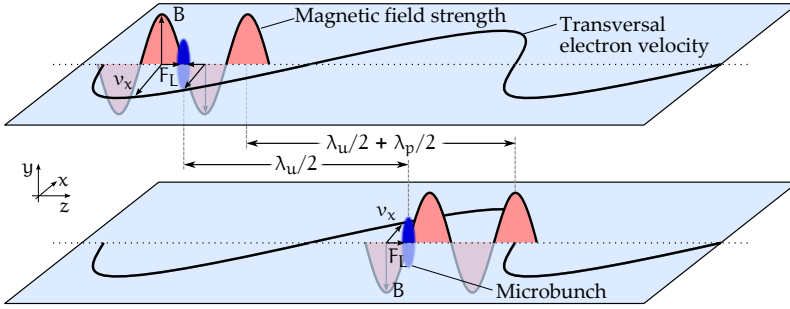


Figure 2.13: Microbunching mechanism induced by the co-propagating electromagnetic wave. An electron traveling outside the microbunch experiences the Lorentz force F_L dragging it into the bunch. When the electron bunch propagated half an undulator period $\lambda_u/2$ its transverse velocity v_x is reversed. During the same period the electromagnetic wave traveled $\lambda_u/2 + \lambda_p/2$ - the magnetic field strength is reversed too and the mechanism maintained. Reproduced from [92].

The mechanism of microbunching is illustrated in figure 2.13. Electrons experience the Lorentz force due to the co-propagating electromagnetic wave. Depending on the individual position of an electron in the light wave, this results in an acceleration or a deceleration. This process effectively confines the electron distribution into small microbunches. Now the electrons have a slightly lower longitudinal velocity \bar{v}_z than the photon beam and thus, when the electrons passed half an undulator period $\lambda_u/2$ the light wave has advanced $\lambda_u/2 + \lambda_p/2$ [92]. Consequently, after half an undulator period both are reversed, the transverse velocity of the electron and the magnetic field, maintaining the direction of the Lorentz force, and the microbunching continues.

At this point, the duration Δt of an FEL pulse can be estimated since spatially, the electromagnetic wave grows by one wavelength λ_p for each of the N_u undulator periods

$$\Delta t = N_u \cdot \frac{\lambda_p}{c}. \quad (2.22)$$

Thus, with $N_u = 1000$ undulator periods (as present at FLASH) the pulse length varies between 13 fs . . . 150 fs for wavelength in the range 4 nm . . . 45 nm.

In the course of the described mechanism, an electromagnetic wave with wavelengths close to λ_p defined by the undulator equa-

tion (2.18) is amplified. In the beginning, the radiation power P grows linearly with respect to the propagation distance z until the photon beam has become strong enough to modulate the electron distribution to microbunches. Subsequently, the interaction between photons and electrons leads to an exponential gain

$$P(z) \propto e^{z/L_g}. \quad (2.23)$$

L_g denotes the gain length which is $L_g = 2.5$ m for FLASH [93]. The exponential growth stops after $\approx 22 L_g$ [92] where the best achievable modulation of the electrons is reached and the saturation regime begins. The course of the gain curve throughout the undulator is depicted in figure 2.14.

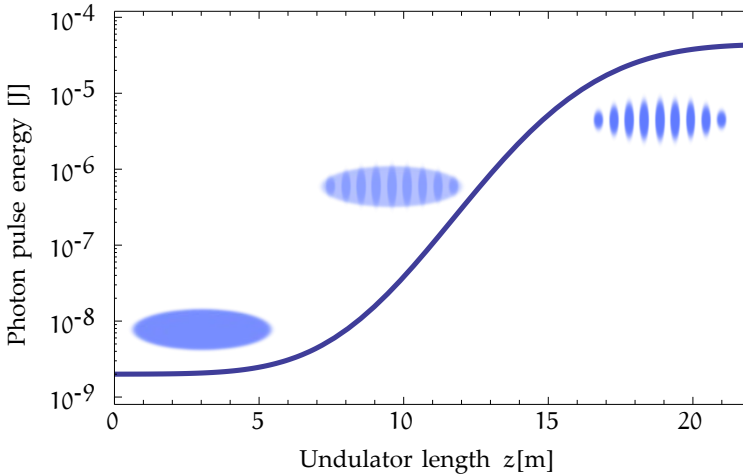


Figure 2.14: Exponential gain of the photon pulse energy by the SASE process. The development of microbunches in the electron cloud is indicated. Reproduced from [85].

Since the entire process starts up from shot noise in the initial electron beam, it has a statistical character and thus, it is called self-amplified spontaneous emission. Individual SASE FEL pulses differ in their intensity, temporal structure and spectral distribution [94] and show a relatively broad spectral range [95]. This issue can be overcome by seeding radiation which induces microbunching before the electrons enter the undulator section. For that purpose an optical laser can be employed [96] or, in a self-seeding scheme, undulator radiation filtered by a monochromator reduces the relative bandwidth by a factor of 40-50 with respect to SASE [97].

In the history of optics, light was first imagined as corpuscles which propagated along light rays. In the year 1704 Newton followed that picture but also attributed wave properties to the nature of light [98] which had been particularized by Huygens some years before [99]. About a century later, only the wave nature of light could explain interference effects observed by Young in his famous double slit experiment [100]. In 1865 Maxwell finally announced a unified mathematical description of light as an electromagnetic wave [101]. However, after some decades it turned out that light carries energy in terms of quanta, as proposed by Einstein to explain the photoelectric effect [102]. Thus, depending on the situation, light can be regarded as both, as a wave to describe its propagation and as a particle to characterize the interacting with matter.

In the frame of this work, light beams are characterized in terms of ray and wave optics. In the following, basic matrix calculations will be introduced describing the propagation of light rays through optical systems. Furthermore, the wavefront and coherence properties of electromagnetic waves are discussed. Finally, the Wigner distribution function is introduced that unifies the entire propagation properties of a light beam.

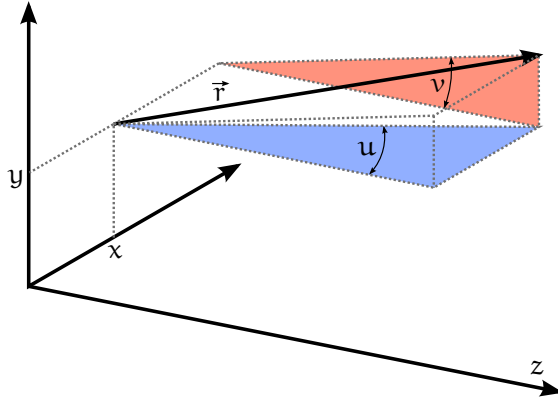
Mainly, this chapter is based on literature by Bastiaans [103, 104, 105, 106] and Mandel and Wolf [107]. A deeper insight into the topic is provided by Torre [108].

3.1 MATRIX METHODS IN RAY OPTICS

In the frame of geometric optics, a light ray in three-dimensional space is described by the vector

$$\vec{r} = \begin{pmatrix} \vec{x} \\ \vec{u} \end{pmatrix} = \begin{pmatrix} x \\ y \\ u \\ v \end{pmatrix} \quad (3.1)$$

with the spatial vector $\vec{x} = (x, y)$ perpendicular to the optical axis z , and the angular pointing direction $\vec{u} = (u, v)$ as depicted in figure 3.1 [109].

Figure 3.1: Definition of the ray vector \vec{r} .

Within the paraxial approximation, the propagation of a light ray \vec{r} through static and lossless systems, e.g., through free space or ideal lenses, corresponds to a matrix multiplication

$$\vec{r}' = \mathcal{S} \cdot \vec{r} \quad \text{with} \quad \mathcal{S} = \begin{pmatrix} \mathcal{A} & \mathcal{B} \\ \mathcal{C} & \mathcal{D} \end{pmatrix} \quad (3.2)$$

where \mathcal{A} , \mathcal{B} , \mathcal{C} and \mathcal{D} are 2x2 sub-matrices. A collection of ray transformation matrices \mathcal{S} is given in the [appendix](#). The propagation matrix \mathcal{S} follows the symplecticity relation [104]

$$\mathcal{S} \cdot \mathcal{J} \cdot \mathcal{S}^T = \mathcal{J} \quad \text{with} \quad \mathcal{J} = \begin{pmatrix} 0 & \mathbb{1} \\ -\mathbb{1} & 0 \end{pmatrix} \quad \text{and} \quad \mathbb{1} = \begin{pmatrix} 1 & 0 \\ 0 & 1 \end{pmatrix} \quad (3.3)$$

and thus, \mathcal{S} contains up to ten independent entries. For astigmatically aligned systems, \mathcal{A} , \mathcal{B} , \mathcal{C} and \mathcal{D} are diagonal matrices reducing the maximum number of independent entries to eight. From equation (3.3) it follows $\det(\mathcal{S}) = 1$.

A light beam, i.e., an ensemble of light rays \vec{r}_i , is described by its centered second order moments comprised in the beam matrix [104]

$$\mathcal{M} = \begin{pmatrix} \langle x^2 \rangle & \langle xy \rangle & \langle xu \rangle & \langle xv \rangle \\ \langle xy \rangle & \langle y^2 \rangle & \langle yu \rangle & \langle yv \rangle \\ \langle xu \rangle & \langle yu \rangle & \langle u^2 \rangle & \langle uv \rangle \\ \langle xv \rangle & \langle yv \rangle & \langle uv \rangle & \langle v^2 \rangle \end{pmatrix}. \quad (3.4)$$

The entries of \mathcal{M} are defined by the Wigner distribution function as it will be discussed in section 3.4. From the beam matrix, a number of fundamental propagation parameters can be derived [109], as summarized for the horizontal direction in equation (3.5). Equivalent relations hold for the vertical direction by replacing x and u by y and v .

$$\begin{aligned}
 \text{Local beam diameter} & \quad d_x = 4\sqrt{\langle x^2 \rangle} \\
 \text{Beam divergence angle} & \quad \theta_x = 4\sqrt{\langle u^2 \rangle} \\
 \text{Waist position} & \quad z_{0,x} = -\frac{\langle xu \rangle}{\langle u^2 \rangle} \\
 \text{Waist diameter} & \quad d_{0,x} = 4\sqrt{\langle x^2 \rangle - \frac{\langle xu \rangle^2}{\langle u^2 \rangle}} \\
 \text{Rayleigh length} & \quad z_{R,x} = 4\sqrt{\frac{\langle x^2 \rangle}{\langle u^2 \rangle} - \frac{\langle xu \rangle^2}{\langle u^2 \rangle^2}} \\
 \text{Beam quality factor} & \quad M_x^2 = \frac{4\pi}{\lambda} \sqrt{\langle x^2 \rangle \langle u^2 \rangle - \langle xu \rangle^2} \quad (3.5)
 \end{aligned}$$

Combining these equations in a suitable way, the divergence angle can be formulated as

$$\theta_x = \frac{d_{0,x}}{z_{R,x}} \quad (3.6)$$

and the beam quality factor in terms of

$$M_x^2 = \frac{\pi}{4} \cdot \frac{d_{0,x} \theta_x}{\lambda}. \quad (3.7)$$

Propagation of the beam matrix \mathcal{M} through an optical system \mathcal{S} corresponds to the matrix operation [104]

$$\mathcal{M}' = \mathcal{S} \cdot \mathcal{M} \cdot \mathcal{S}^T. \quad (3.8)$$

Here, the example of a free space propagation $\mathcal{S}_{\text{prop}}(z) \cdot \mathcal{M} \cdot \mathcal{S}_{\text{prop}}^T(z)$ serves to describe the local beam diameter along the optical axis in terms of the hyperbolic function

$$d_x(z) = d_{0,x} \sqrt{1 + \left(\frac{z - z_{0,x}}{z_{R,x}} \right)^2} \quad (3.9)$$

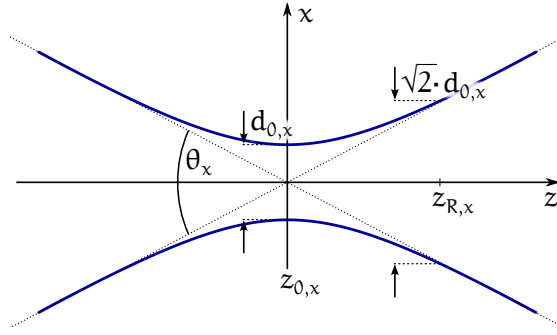


Figure 3.2: Local beam diameter $d_x(z)$ close to the waist position $z_{0,x}$ with the propagation parameters: waist diameter $d_{0,x}$, Rayleigh length $z_{R,x}$ and divergence angle θ_x .

which is illustrated for the region around the horizontal waist position $z_{0,x}$ in figure 3.2 (for $S_{\text{prop}}(z)$ see the [appendix](#)).

In the frame of a beam propagation through astigmatically aligned optical systems \mathcal{S} , the beam quality factor M_x^2 is an invariant for one-dimensional and separable beams, i.e., beams where all mixed moments vanish [109]. For the limiting case of a Gaussian beam [110] it holds $M^2 = 1$, otherwise $M^2 > 1$. In case of non-separable beams, the more general quantity $M^4 = (4\pi/\lambda)^2 \sqrt{\det(\mathcal{M})}$ is conserved. Practically, knowledge of the M^2 value for a particular beam allows the estimation of the waist diameter after propagation through optical systems.

If the mixed moment $\langle xy \rangle$ does not vanish, the principal axis system of the near-field is rotated by the azimuth angle Θ_{xy} as indicated in figure 3.3. The same applies to the far-field if $\langle uv \rangle \neq 0$ resulting in an azimuth angle Θ_{uv} which can be different from Θ_{xy} .

$$\begin{aligned} \text{Near-field azimuth angle} \quad \Theta_{xy} &= \frac{1}{2} \arctan \left(\frac{\langle xy \rangle}{\langle y^2 \rangle - \langle x^2 \rangle} \right) \\ \text{Far-field azimuth angle} \quad \Theta_{uv} &= \frac{1}{2} \arctan \left(\frac{\langle uv \rangle}{\langle v^2 \rangle - \langle u^2 \rangle} \right) \quad (3.10) \end{aligned}$$

In order to transform a beam matrix \mathcal{M} into the principal axis system of the near-field, the rotation matrix $S_{\text{rot}}(\Theta_{xy})$ needs to be applied which is given in equation (A.4). Subsequent derivation of the beam diameters d'_x and d'_y defines the variance ellipse of the near field, as it is depicted in figure 3.3.

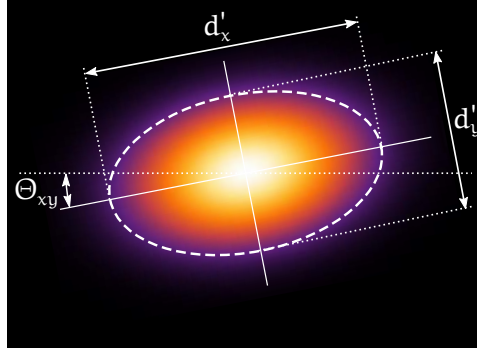


Figure 3.3: Arbitrary near-field intensity distribution $I(\vec{x})$ with the variance ellipse which is defined by the beam diameters d'_x and d'_y in the principal axis system and the azimuth angle Θ_{xy} .

3.2 THE WAVEFRONT

Regarding a light beam as an electromagnetic wave, the wavefront $w_{z_0}(x, y)$ describes a continuous surface perpendicular to the mean transport direction of energy at position z_0 of the optical axis. Mathematically, it is defined as $w_{z_0}(x, y)$ that minimizes the expression [111]

$$\iint I_{z_0}(x, y) \cdot \left| \vec{S}_{\perp}(x, y, z_0) - \vec{\nabla} w_{z_0}(x, y) \right|^2 dx dy \quad (3.11)$$

with the two-dimensional Nabla operator $\vec{\nabla} = (\partial_x, \partial_y)$ and the transverse, intensity normalized Poynting vector

$$\vec{S}_{\perp}(x, y, z_0) = \frac{1}{I_{z_0}(x, y)} \begin{pmatrix} S_x(x, y, z_0) \\ S_y(x, y, z_0) \end{pmatrix}$$

which represents the energy flux direction of an electromagnetic field in a plane defined by $z = z_0$ [112].

Apparently, expression (3.11) is minimized by

$$\vec{S}_{\perp}(x, y, z_0) = \vec{\nabla} w_{z_0}(x, y). \quad (3.12)$$

Assuming an electromagnetic beam with the phase distribution $\varphi(x, y, z)$ described by

$$\vec{E}(x, y, z) = \vec{E}_0(x, y, z) e^{i\varphi(x, y, z)} \quad (3.13)$$

it can be shown that within the paraxial approximation $|\partial_z E_j| \ll |kE_j|$, the transverse, intensity normalized Poynting vector is [113]

$$\vec{S}_\perp(x, y, z_0) = \frac{1}{k} \vec{\nabla} \varphi(x, y, z_0) \quad (3.14)$$

with the wave number $k = 2\pi/\lambda$. Thus, with equations (3.12) and (3.14) the gradient of wavefront and phase are proportional to each other and the following relation is found

$$w_{z_0}(x, y) = \frac{1}{k} \varphi(x, y, z_0) + c_0. \quad (3.15)$$

However, there are special cases for which equation (3.15) does not hold, i.e., if $\varphi(x, y, z)$ shows discontinuities such as a phase vortex. In that case, $w_{z_0}(x, y)$ would not exhibit a continuous surface standing in contrast to its definition. Here, minimizing expression (3.11) leads to a plane wavefront.

3.2.1 Polynomial expansion of the wavefront

In order to classify a wavefront $w(x, y)$ it is convenient to express it as a composition of the contained aberrations. Especially for circular beams, a suitable complete sequence of orthogonal polynomials is given by the Zernike polynomials which are defined in polar coordinates [110]

$$\begin{aligned} Z_n^m(\rho, \Theta) &= R_n^m(\rho) \cos(m\Theta) \\ Z_n^{-m}(\rho, \Theta) &= R_n^m(\rho) \sin(m\Theta) \end{aligned} \quad (3.16)$$

where m and n are non-negative integers with $n \geq m$. $R_n^m(\rho)$ are the radial polynomials which are given by

$$\begin{aligned} (n-m) \text{ even :} \\ R_n^m(\rho) &= \sum_{k=0}^{(n-m)/2} \frac{(-1)^k (n-k)!}{k! (\frac{n+m}{2} - k)! (\frac{n-m}{2} - k)!} \rho^{n-2k} \\ (n-m) \text{ odd :} \\ R_n^m(\rho) &= 0. \end{aligned} \quad (3.17)$$

The definition range is confined by the unit circle $0 \geq \Theta \geq 2\pi$ and $0 \geq \rho \geq 1$. The first ten Zernike polynomials are depicted in figure 3.4 each representing an aberration.

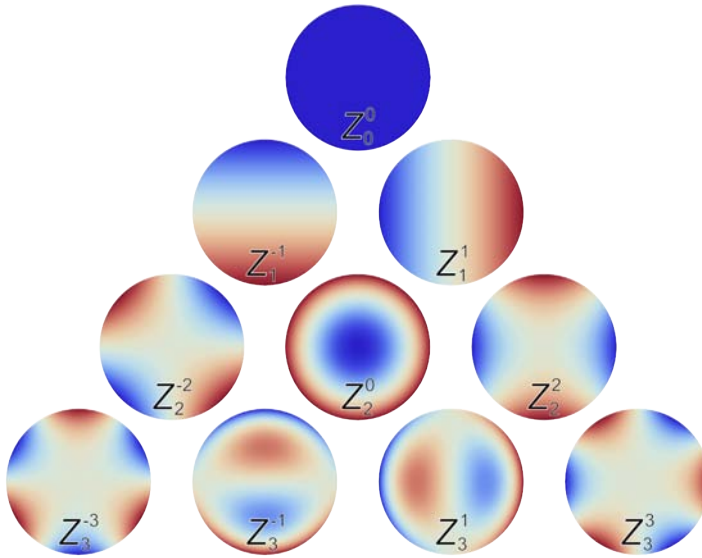


Figure 3.4: The first ten Zernike polynomials (from top to bottom, left to right): piston, y-tilt, x-tilt, diagonal astigmatism, defocus, aligned astigmatism, trefoil, y-coma, x-coma, trefoil.

With the complete set of functions Z_n^m it is possible to represent any wavefront $w(x, y)$ in the form

$$w(x, y) = a_0 \cdot Z_0^0(x, y) + a_1 \cdot Z_1^{-1}(x, y) + a_2 \cdot Z_1^1(x, y) + \dots \quad (3.18)$$

The relative value of the coefficients a_i resembles the strength of the corresponding aberration.

3.3 COHERENCE PROPERTIES

The coherence properties of a light beam characterize the degree of correlations within its electric field, i.e., whether the complex valued time curve of $E(\vec{x}, t)$ at different positions \vec{x} and times t resemble each other. Coherence is required in order to generate interference effects with an electromagnetic beam. Vice versa, the degree of coherence can be measured by analyzing this phenomenon. The most prominent example of a corresponding approach is Young's experiment where two elementary waves are superimposed on a distant screen [100]: the better the visibility of interference fringes, the higher the coherence between both waves.

The mathematical tool to quantify the coherence within a beam is the cross correlation function between the complex electric fields $E(\vec{x}_1, t + \tau)$ and $E(\vec{x}_2, t)$. Here, the *mutual coherence function* (MCF) or *mutual intensity* Γ is formulated in terms of the center vector $\vec{x} = (x, y)$ and the distance vector $\vec{s} = (s_x, s_y)$ between both points \vec{x}_1 and \vec{x}_2 as indicated in figure 3.5 [114]

$$\Gamma(\vec{x}, \vec{s}, \tau) = \frac{1}{2} c \epsilon_0 \left\langle E\left(\vec{x} - \frac{\vec{s}}{2}, t + \tau\right) E^*\left(\vec{x} + \frac{\vec{s}}{2}, t\right) \right\rangle \quad (3.19)$$

where $\langle \dots \rangle$ indicates the average over time, $*$ denotes the complex conjugate, c is the speed of light and ϵ_0 the vacuum permittivity. Γ has the dimension of an intensity and in general, it is a complex valued function. In particular, if $\vec{s} = 0$ both points of the electric field coincide and for a vanishing time delay τ , Γ results in the intensity

$$\Gamma(\vec{x}, 0, 0) = I(\vec{x}).$$

In the following, the time delay τ is omitted since here, only the *spatial* coherence properties are under investigation.

A corresponding dimensionless quantity normalized by the intensities $\sqrt{I(\vec{x}_1) \cdot I(\vec{x}_2)}$ is given by the *local degree of coherence*

$$\gamma(\vec{x}, \vec{s}) = \frac{\Gamma(\vec{x}, \vec{s})}{\sqrt{\Gamma(\vec{x} - \vec{s}/2, 0) \Gamma(\vec{x} + \vec{s}/2, 0)}}. \quad (3.20)$$

γ is complex valued too and the value of $|\gamma|$ ranges between 0 and 1. $|\gamma| = 1$ corresponds to full coherence, $|\gamma| = 0$ to complete incoherence and if $0 < |\gamma| < 1$ the electric fields are said to be partially coherent.

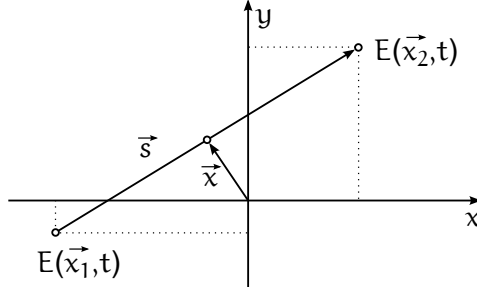


Figure 3.5: To the definition of the mutual coherence function: the positions \vec{x}_1 and \vec{x}_2 are expressed by center and distance vector $\vec{x} = (\vec{x}_1 + \vec{x}_2)/2$ and $\vec{s} = (\vec{x}_2 - \vec{x}_1)$.

Since $\Gamma(\vec{x}, \vec{s})$ and $\gamma(\vec{x}, \vec{s})$ might describe rather complex correlations on a four-dimensional phase space, it is convenient to introduce characteristic quantities resembling the properties of both functions. The spatial decay of the MCF with increasing $|\vec{s}|$ is given by the coherence lengths l_x and l_y confining a region which can be regarded as mutually coherent [115]

$$l_x = \sqrt{8 \frac{\int (s_x - \langle s_x \rangle)^2 |\Gamma(\vec{x}, \vec{s})|^2 d^2x d^2s}{\int |\Gamma(\vec{x}, \vec{s})|^2 d^2x d^2s}} \quad (3.21)$$

with $d^2x = dx dy$ and $d^2s = ds_x ds_y$. Correspondingly, l_y is derived. Both of these quantities are real valued. Finally, the *global degree of coherence*

$$\kappa = \frac{\int |\Gamma(\vec{x}, \vec{s})|^2 d^2x d^2s}{(\int |\Gamma(\vec{x}, 0)| d^2x)^2} \quad (3.22)$$

unifies the coherence properties of a beam in a single real value, ranging between 0 for an incoherent beam and 1 for a fully coherent beam.

3.3.1 Gaussian Schell-model beam source

A simple mathematical model function of Γ is given within the Gaussian Schell-model, which is of fundamental importance in the field of beam characterization. In good approximation, it can be applied to a large number of experimental laser beams that exhibit arbitrary degrees of coherence. In the following, the model will be employed to derive a relation between coherence length, waist

diameter and global degree of coherence. Since here, the mutual coherence function is separable, i.e. $\Gamma_{GS}(\vec{x}, \vec{s}) = \Gamma_x(x, s_x) \cdot \Gamma_y(y, s_y)$, the following discussion is based on the two-dimensional distribution $\Gamma_x(x, s_x)$. However, equivalent relations hold for $\Gamma_y(y, s_y)$.

The mutual coherence function of a monochromatic Gaussian Schell-model beam at its waist position is given by [107]

$$\Gamma_x(x, s_x) = \sqrt{I_0} \cdot \exp\left(-\frac{x^2}{2\sigma_x^2}\right) \cdot \exp\left(-\frac{(s_x/2)^2}{2\sigma_{s_x}^2}\right) \quad (3.23)$$

with $\sigma_x \geq \sigma_{s_x}$ both real valued. The Gaussian distribution Γ_x decreases in x - and s_x -direction with the standard deviations σ_x and σ_{s_x} . Employing equations (3.5) and (3.21), σ_x and σ_{s_x} can be identified with beam diameter d_x and coherence length l_x according to

$$d_x = 4\sigma_x \quad \text{and} \quad l_x = 4\sigma_{s_x}. \quad (3.24)$$

Normalization of the mutual coherence function following equation (3.20) leads to the local degree of coherence

$$\begin{aligned} \gamma_x(s_x) &= \exp\left(-\frac{(s_x/2)^2}{2} \left(\frac{1}{\sigma_{s_x}^2} - \frac{1}{\sigma_x^2}\right)\right) \\ &= \exp\left(-\frac{(s_x/2)^2}{2\sigma_{\gamma_x}^2}\right) \end{aligned} \quad (3.25)$$

which apparently does not depend on x . The newly introduced real valued standard deviation σ_{γ_x} is related to beam diameter d_x and coherence length l_x by

$$\frac{1}{(4\sigma_{\gamma_x})^2} = \frac{1}{l_x^2} - \frac{1}{d_x^2}. \quad (3.26)$$

Here, the restriction $d_x \geq l_x$ ensures that σ_{γ_x} is a real quantity (compare definition (3.23)). Consequently, for a beam with a specific diameter d_x , the following intervals for coherence length l_x and standard deviation σ_{γ_x} can be formulated:

- Width of local degree of coherence $\sigma_{\gamma_x} = 0 \dots \infty$
- Coherence length $l_x = 0 \dots d_x$.

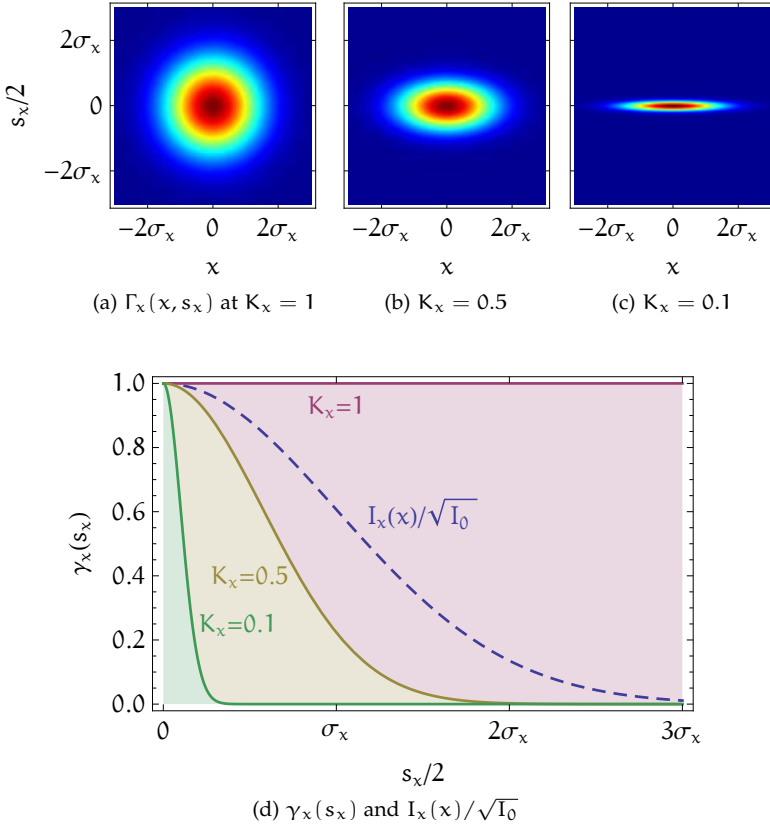


Figure 3.6: Coherence functions in the Gaussian Schell-model at constant beam diameter and various degrees of coherence K_x .
 (a)-(c): Mutual coherence function $\Gamma_x(x, s_x)$.
 (d): Local degree of coherence $\gamma_x(s_x)$. The intensity distribution $I_x(x)/\sqrt{I_0}$ is valid for arbitrary K_x .

For a completely incoherent beam both quantities vanish and $\gamma_x \equiv 0$ for all $s_x > 0$. Full coherence is represented by $\sigma_{\gamma_x} \rightarrow \infty$ and $l_x \rightarrow d_x$ and thus, the local degree of coherence spans until infinity $\gamma_x \equiv 1$. This case poses also the upper limit for the coherence length, since values larger than the beam diameter $l_x > d_x$ would result in a complex valued σ_{γ_x} .

Computation of the global degree of coherence leads to the simple relation

$$K = \frac{\sigma_{s_x}}{\sigma_x} \cdot \frac{\sigma_{s_y}}{\sigma_y} = \frac{l_x}{d_x} \cdot \frac{l_y}{d_y}. \tag{3.27}$$

Obviously, K only depends on the ratios between coherence length and beam diameter. Since here the beam is separable, the global degree of coherence K is understood as a product of its horizontal and vertical value $K_x = \frac{l_x}{d_x}$ and $K_y = \frac{l_y}{d_y}$.

The mutual coherence function $\Gamma_x(x, s_x)$ and local degree of coherence $\gamma_x(x, s_x)$ are depicted in figure 3.6 for a beam with constant beam diameter $d_x = 4\sigma_x$ and three different degrees of coherence K_x . In the chosen representation, $\Gamma_x(x, s_x)$ shows a circular shape in case of full coherence. A lower degree of coherence involves a shorter coherence length l_x and thus, the extent of $\Gamma_x(x, s_x)$ is reduced in s_x -direction.

Sub-figure 3.6(d) shows the local degree of coherence $\gamma_x(s_x)$ for three different values of K_x . The intensity distribution $I_x(x)/\sqrt{I_0}$ is represented by a dashed curve and holds for arbitrary degrees of coherence. Here, the width of $\gamma_x(s_x)$ is not restricted by the beam diameter but exceeds it for $K_x > 1/\sqrt{2}$ and approaches infinity for $K_x = 1$.

3.4 THE WIGNER DISTRIBUTION FUNCTION

In the year 1932, Eugene Paul Wigner introduced the Wigner function as a quasiprobability distribution of a quantum mechanical particle depending on location \mathbf{x} and momentum \mathbf{p} [116]. Later on, applications of the Wigner function were found in other scientific fields too, such as in signal analysis and ultrafast optics, where the phase space is comprised of time t and frequency f [117, 118]. In optics, it is used to describe beam propagation in terms of ray ensembles [103, 105]. Since this formalism also includes interference effects, the Wigner distribution function bridges the gap between ray and wave optics [108].

The Wigner distribution function (WDF) of a quasi-monochromatic paraxial beam is defined as two-dimensional Fourier transform of the mutual coherence function [104]

$$h(\vec{\mathbf{x}}, \vec{\mathbf{u}}) = \left(\frac{k}{2\pi}\right)^2 \int \Gamma(\vec{\mathbf{x}}, \vec{\mathbf{s}}) e^{-ik\vec{\mathbf{u}} \cdot \vec{\mathbf{s}}} d^2s \quad (3.28)$$

where $k = 2\pi/\lambda$ denotes the mean wave number. The corresponding back-transformation yields the MCF again

$$\Gamma(\vec{\mathbf{x}}, \vec{\mathbf{s}}) = \int h(\vec{\mathbf{x}}, \vec{\mathbf{u}}) e^{ik\vec{\mathbf{u}} \cdot \vec{\mathbf{s}}} d^2u \quad (3.29)$$

with $d^2u = dudv$. The value of $h(\vec{\mathbf{x}}, \vec{\mathbf{u}})$ is always real since $\Gamma(\vec{\mathbf{x}}, \vec{\mathbf{s}})$ is symmetric with respect to the $\vec{\mathbf{s}}$ -coordinate $\Gamma(\vec{\mathbf{x}}, \vec{\mathbf{s}}) = \Gamma^*(\vec{\mathbf{x}}, -\vec{\mathbf{s}})$.

Walther, who first introduced the Wigner distribution function in the context of optics [119], denoted it as *generalized radiance*. This implies the interpretation of $h(\vec{\mathbf{x}}, \vec{\mathbf{u}})$ as amplitude of a ray passing through the point $\vec{\mathbf{x}}$ and having the direction $\vec{\mathbf{u}}$ [105]. However, $h(\vec{\mathbf{x}}, \vec{\mathbf{u}})$ is not necessarily non-negative what limits the interpretation as a radiance to a certain extent.

Nevertheless, the integrals of $h(\vec{\mathbf{x}}, \vec{\mathbf{u}})$ have a clear physical meaning and result in near-field $I(\vec{\mathbf{x}})$, far-field $\hat{I}(\vec{\mathbf{u}})$ and the total power P of the beam [104]

$$\begin{aligned} I(\vec{\mathbf{x}}) &= \int h(\vec{\mathbf{x}}, \vec{\mathbf{u}}) d^2u \\ \hat{I}(\vec{\mathbf{u}}) &= \frac{1}{(2\pi)^2} \int h(\vec{\mathbf{x}}, \vec{\mathbf{u}}) d^2x \\ P &= \int h(\vec{\mathbf{x}}, \vec{\mathbf{u}}) d^2x d^2u. \end{aligned} \quad (3.30)$$

The moments of the Wigner distribution are derived by [104]

$$\langle x^i y^j u^m v^n \rangle = \frac{1}{P} \int x^i y^j u^m v^n \cdot h(\vec{x}, \vec{u}) d^2x d^2u \quad (3.31)$$

with the integer variables i, j, m and n . The first-order moments $\langle x \rangle$, $\langle y \rangle$, $\langle u \rangle$ and $\langle v \rangle$ define the centroid of the WDF with respect to the corresponding variable. Choosing the coordinate system properly, these moments vanish, which is assumed in the following. The second-order moments with $i + j + m + n = 2$ are comprised in the beam matrix \mathcal{M} which is discussed in section 3.1. Here, the most descriptive quantities are $\langle x^2 \rangle$ and $\langle u^2 \rangle$ resulting in local diameter $d_x = 4\sqrt{\langle x^2 \rangle}$ and divergence angle $\theta_x = 4\sqrt{\langle u^2 \rangle}$ of the beam. These values represent the extent of $h(\vec{x}, \vec{u})$ in x - and u -direction. Further beam parameters, e.g., waist diameter or Rayleigh length are derived with the relations summarized in equation (3.5).

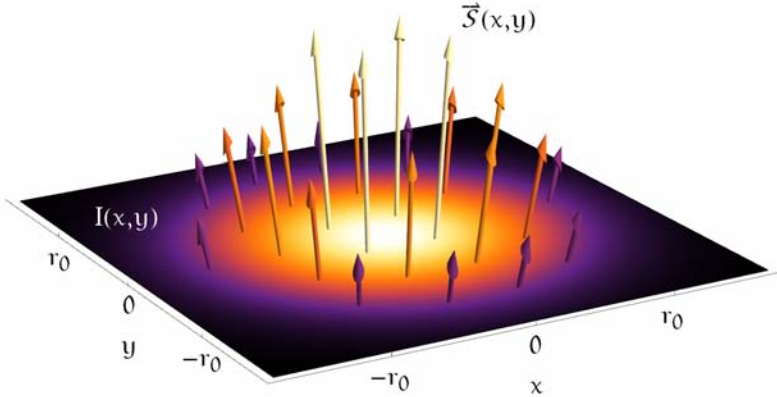


Figure 3.7: The Wigner distribution function contains both, the spatial intensity distribution $I(x, y)$ and directional information in terms of the local Poynting vector $\vec{S}(x, y)$. The illustration shows an arbitrary divergent Gaussian Schell-model beam with beam radius $r_0 = d_0/2$.

The transverse, intensity normalized Poynting vector $\vec{S}'(x, y)$ is derived by [108]

$$\vec{S}'_{\perp}(x, y) = \frac{\lambda^2}{P} \int \vec{u} \cdot h(\vec{x}, \vec{u}) d^2u \quad (3.32)$$

and with that the local wavefront is determined by relation (3.11). The third component of the three-dimensional Poynting vector $\vec{S}(x, y)$

is given by $S_z(x, y) = I(x, y) \sqrt{1 - |\vec{S}_\perp(x, y)|^2}$. An illustration of a Wigner distribution is given in figure 3.7 for an arbitrary divergent beam where spatial and directional intensity information are combined.

Finally, application of Parseval's theorem to equation (3.22) yields the global degree of coherence formulated in terms of the Wigner distribution

$$K = \frac{\lambda^2}{p^2} \int h(\vec{x}, \vec{u})^2 d^2x d^2u. \quad (3.33)$$

3.4.1 Wigner distribution function of a Gaussian Schell-model beam

The Wigner distribution function h_{GS} of a Gaussian Schell-model beam source is specified by the mutual coherence function Γ_{GS} which is discussed in section 3.3.1. Since $h_{GS} = h_x(x, u) \cdot h_y(y, v)$ is separable, the following discussion focuses on the two-dimensional distribution $h_x(x, u)$. However, equivalent relations hold for $h_y(y, v)$. Γ_x is transformed into the WDF by combining equations (3.23) and (3.28)

$$h_x(x, u) = \sqrt{h_0} \cdot \exp\left(-\frac{x^2}{2\sigma_x^2}\right) \cdot \exp\left(-\frac{u^2}{2\sigma_u^2}\right). \quad (3.34)$$

Here, a new standard deviation σ_u is introduced that quantifies the decay of the Gaussian distribution along the angular axis u . In other words, σ_u defines the divergence $\theta_x = 4\sigma_u$ of the beam. Interestingly, it results that the divergence θ_x of the beam is inversely proportional to its coherence length l_x

$$\sigma_u = \frac{\lambda}{(4\pi)} \cdot \frac{1}{\sigma_s} \quad \text{or} \quad \theta_x = \frac{\lambda}{(\pi/4)} \cdot \frac{1}{l_x}. \quad (3.35)$$

Computing the horizontal component of the global degree of coherence $K = K_x \cdot K_y$ gives a direct connection to the beam quality factor M_x^2

$$K_x = \frac{4}{\pi} \cdot \frac{\lambda}{d_{0,x}\theta_x} = \frac{1}{M_x^2}. \quad (3.36)$$

This equation provides a clear interpretation of the coherence with respect to the Wigner distribution: K_x is proportional to the inverse of the phase space volume $V_x = \pi \cdot d_{0,x}\theta_x$. Thus, the smaller

the extent of h_x in spatial and angular direction, the larger is the coherence. With $K_x \leq 1$, this relation also defines the smallest possible phase space that a beam can occupy

$$\pi \cdot d_{0,x} \theta_x \geq 4\lambda \quad (3.37)$$

which is only reached by a fully coherent beam.

3.4.2 Propagation of the Wigner distribution function

Propagation of the Wigner distribution through first-order optical systems follows the matrix formalism of section 3.1. The ray transformation (3.2) with the system matrix \mathcal{S} from an input plane to an output plane reads [105, 120]

$$h_{\text{in}}(\vec{x}, \vec{u}) = h_{\text{out}}(\mathcal{A}\vec{x} + \mathcal{B}\vec{u}, \mathcal{C}\vec{x} + \mathcal{D}\vec{u}) \quad (3.38)$$

or, as a back-transformation with the inverse \mathcal{S}^{-1}

$$h_{\text{in}}(\mathcal{D}\vec{x} - \mathcal{B}\vec{u}, -\mathcal{C}\vec{x} + \mathcal{A}\vec{u}) = h_{\text{out}}(\vec{x}, \vec{u}). \quad (3.39)$$

In that context, an important and simple example is the propagation through free space by a distance z with $\mathcal{A} = \mathbb{1}$, $\mathcal{B} = z \cdot \mathbb{1}$, $\mathcal{C} = 0$ and $\mathcal{D} = \mathbb{1}$ (see the [appendix](#)). A known Wigner distribution function h then transforms as

$$h(\vec{x}, \vec{u})|_z = h(\vec{x} - z \cdot \vec{u}, \vec{u})|_{z=0} \quad (3.40)$$

where $|_z$ denotes the z -position of the respective Wigner distribution. This transformation represents a shear in \vec{x} -direction. The WDF of a Gaussian Schell-model beam $h_x(x, u)$ (see equation (3.34)) is illustrated in figure 3.8 at different propagation distances z . Obviously, the shear transformation affects near-field and local beam diameter while far-field and beam divergence stay unchanged. Convergent and divergent beam are identified by the inclination of the Wigner distribution.

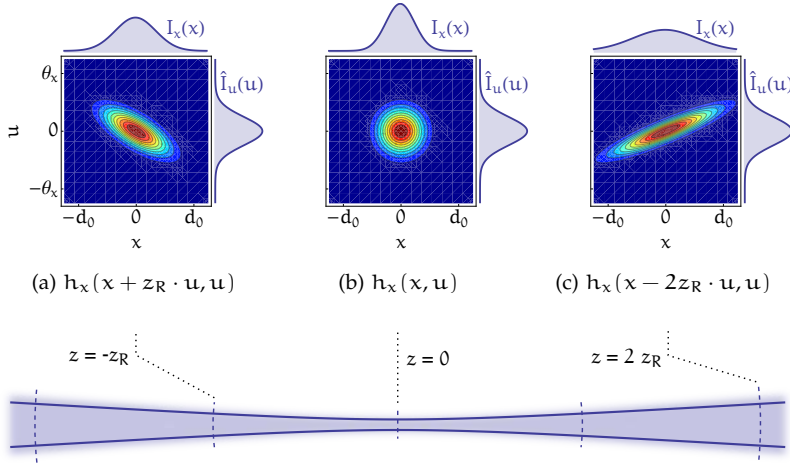


Figure 3.8: Free propagation of the Wigner distribution function $h_x(x, u)$ depicted for a Gaussian Schell-model beam. While the far-field $\hat{I}(u)$ of the beam stays unchanged, the near-field $I(x)$ is affected by the shear transformation of the Wigner distribution.

3.4.3 Reconstruction of the Wigner distribution function for separable and non-separable beams

In the following, a link between the WDF and measurable intensity data is provided. Formulating expression (3.39) in Fourier space (implied by $\tilde{\cdot}$) yields [120]

$$\tilde{h}_{\text{in}}(\mathcal{A}^T \vec{q} + \mathcal{C}^T \vec{j}, \mathcal{B}^T \vec{q} + \mathcal{D}^T \vec{j}) = \tilde{h}_{\text{out}}(\vec{q}, \vec{j}) \quad (3.41)$$

where \vec{q} and \vec{j} are the reciprocal coordinates corresponding to \vec{x} and \vec{u} and T denotes the transpose of a matrix. With the relation $\tilde{h}(\vec{q}, 0) = \tilde{I}(\vec{q})$ this leads to [121]

$$\tilde{h}_{\text{ref}}(\mathcal{A}^T \vec{q}, \mathcal{B}^T \vec{q}) = \tilde{I}_{\mathcal{A}, \mathcal{B}}(\vec{q}). \quad (3.42)$$

The derived equation corresponds to the *projection slice theorem of tomography* which states that in Fourier space, intensity profiles represent slices of the Wigner distribution function, as defined by the transformation matrices \mathcal{A} and \mathcal{B} [122, 123]. In other words, intensity information of a beam can be employed to reconstruct its a priori unknown Wigner distribution. Particularly, a distribution $\tilde{I}_{\mathcal{A}, \mathcal{B}}$

can be mapped directly into the corresponding two-dimensional plane in the reciprocal Wigner space. Now, in order to recover the phase space information entirely, many different planes need to be accessed. This involves an optical system which offers a suitable variation of the system matrices \mathcal{A} and \mathcal{B} . Two possible realizations will be presented in detail in section 6. In the following, the basic example of a free-space propagation is described which is sufficient to reconstruct the Wigner distribution of separable beams.

In general, i.e., for *non-separable* beams, equation (3.42) poses a four-dimensional problem. However, in the case of *separability*, the Wigner distribution beam can be formulated in terms of a product

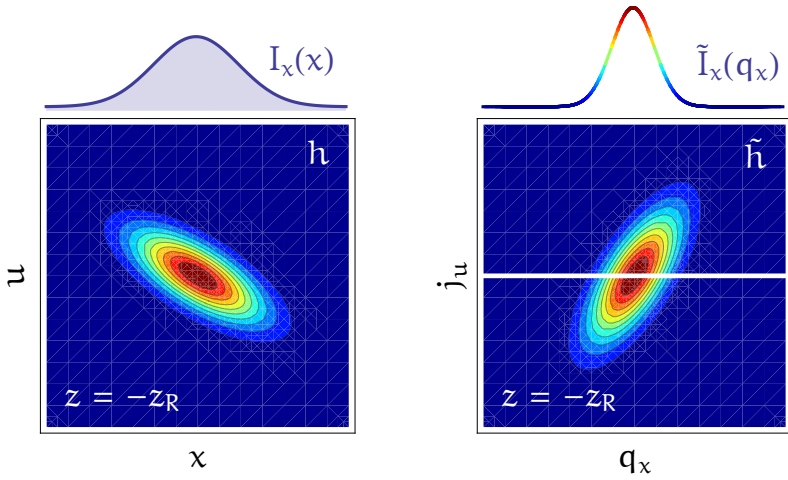
$$h(x, y, u, v) = h_x(x, u) \cdot h_y(y, v) \quad (3.43)$$

and relation (3.42) splits into two independent two-dimensional problems. Correspondingly, the intensity distribution follows the same notation $I(x, y) = I_x(x) \cdot I_y(y)$. Considering a beam propagation through free space, this results in

$$\begin{aligned} \tilde{h}_x(q_x, z \cdot q_x)|_{z=0} &= \tilde{I}_x(q_x)|_z \\ \tilde{h}_y(q_y, z \cdot q_y)|_{z=0} &= \tilde{I}_y(q_y)|_z. \end{aligned} \quad (3.44)$$

With a sufficient number of intensity profiles captured at different positions z , the reciprocal Wigner phase space can be recovered. Subsequently, the Wigner distribution function is derived at the reference position $z = 0$ by a Fourier back-transform.

The principle of this tomographic reconstruction is shown in figure 3.9. The basic relations between Wigner distribution and the near-field profile are illustrated in real space and Fourier space. The entire reconstruction procedure is described step-by-step with experimental data in chapter 6.

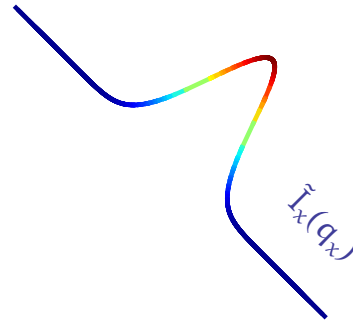
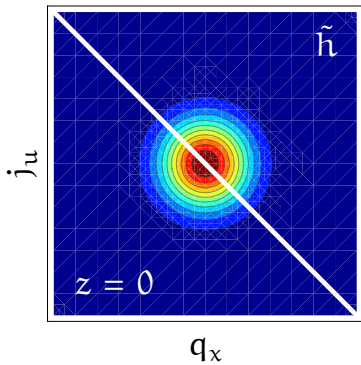


(a) In real space the near field intensity profile results from an integration of the Wigner distribution

$$\int h_x(x, u) du|_{-z_R} = I_x(x)|_{-z_R}.$$

(b) In Fourier space the intensity represents a slice of the Wigner distribution

$$\tilde{h}_x(q_x, 0)|_{-z_R} = \tilde{I}_x(q_x)|_{-z_R}.$$



(c) With respect to the Wigner distribution at reference position $z = 0$, the intensity distribution at position $z = -z_R$ represents a different slice according to

$$\tilde{h}_x(q_x, -z_R \cdot q_x)|_{z=0} = \tilde{I}_x(q_x)|_{-z_R}.$$

Figure 3.9: Scheme of the reconstruction of the Wigner distribution function. It is shown how the near-field profile at a position $z = -z_R$ is related to the Wigner distribution at the reference position $z = 0$.

BRILLIANCE IMPROVEMENT OF A LASER-PRODUCED PLASMA SOURCE

A high brilliance of laser-produced plasma sources goes along with a high particle density of the target material. Of course, this requirement is met by solid and liquid target concepts. Nevertheless, when the electron density of the plasma reaches its critical value n_c given in equation 2.5, the incident laser beam is reflected and the heating process stops. In that case, the density of solid or liquid targets is even too high and needs to be lowered by a less intense pre-pulse [56]. Furthermore, these target concepts always have the drawback of a debris production demanding additional technical efforts for its mitigation.

Here, the focus is put on gaseous targets providing clean, versatile and compact sources but at a comparatively low brilliance. Typically, the resulting plasma reaches electron densities which are one or two magnitudes below the critical density [54]. Thus, in order to enhance the brilliance of these sources, the possibility is explored to increase the particle density of the supersonic gas jet. The basic idea is to generate shock waves which involve a local density increase up to a factor of 6 as discussed in section 2.1.2. In particular, the barrel shock structure evolves when applying a low pressure atmosphere to the jet. Focusing a strong laser pulse into this enhanced density region, a plasma is produced which is brighter and smaller than before.

In the following, the setup of a laser-produced plasma source employing a jet target is described. Afterwards, the experimental techniques to characterize gas jet and soft x-ray radiation are explained. Finally, the results are presented which comprise a qualitative and quantitative characterization of the observed shock structures and the beneficial effect on the plasma generation.

This chapter is based on a previous publication [50] and has been revised and extended partly.

4.1 THE LASER-PRODUCED SOFT X-RAY SOURCE

The setup of a standard soft x-ray source based on gas targets is used [8]. It basically consists of a piezo-electrically operated Proch-Trickl gas valve [124] mounted on a vacuum chamber, and a driving Nd:YAG laser which emits radiation at the fundamental wavelength 1064 nm with a pulse energy of 800 mJ and a pulse duration of 6 ns (InnoLas SpitLight 600). The intensity profile of the unfocused laser beam, measured by a CCD camera (Lumenera Lu160M), reveals a beam diameter of 5.9 mm (derived with equation (3.5)), corresponding to a mean power density of $4.9 \cdot 10^8 \text{ W cm}^{-2}$. Plasma production takes place as soon as a critical power density of $\approx 10^{12} \text{ W cm}^{-2}$ is reached in the focused beam at a sufficiently large particle density [125]. This initiates the first ionization of the target gas followed by avalanche ionization, creating large numbers of free electrons.

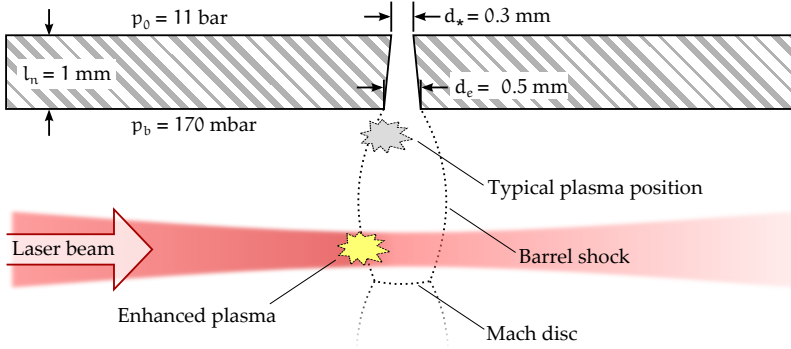


Figure 4.1: Principle of plasma generation employing jet targets: typically the plasma is generated close to the nozzle under vacuum conditions. Applying a background pressure p_b induces the barrel shock structure which enhances plasma generation due to a local density increase.

The target gas is expanded through a divergent nozzle of conical shape. Over a length of $l_n = 1 \text{ mm}$ its diameter increases from the throat diameter $d_* = 0.3 \text{ mm}$ to the exit diameter $d_e = 0.5 \text{ mm}$. The nozzle is opened for a period of 1 ms, generating an underexpanded supersonic jet that expands from stagnation pressure $p_0 = 11 \text{ bar}$ into vacuum, i.e., the background pressure p_b is as low as 10^{-4} mbar . The laser is focused into the gas as soon as the jet flow is steady. The position where the plasma is produced is located $500 \mu\text{m}$, i.e., one diameter d_e behind the nozzle exit (see the typical plasma position indicated in figure 4.1). Although the density is

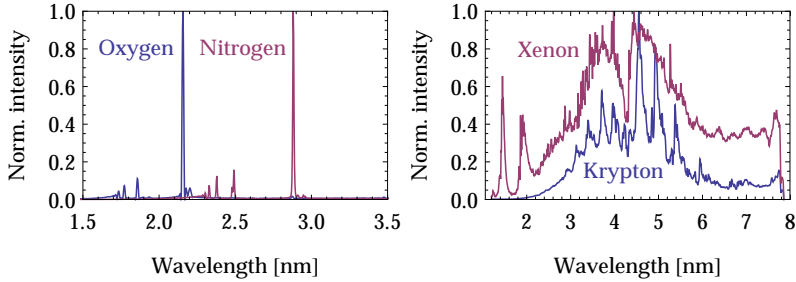


Figure 4.2: Characteristic emission spectra of various target gases, captured with a soft x-ray spectrometer.

highest at the nozzle exit the plasma should not be generated closer to the nozzle because of growing degradation effects.

By employing different target species, various spectra can be obtained in the EUV and soft x-ray range. Noble gases with high atomic numbers such as xenon, argon or krypton are broadband emitters, while oxygen or nitrogen each produce several narrow lines. Corresponding spectra can be found in figure 4.2, produced by a system comparable to that described above and captured with a soft x-ray spectrometer, which is described in detail in [8]. Here, nitrogen is used in combination with a titanium filter, resulting in a monochromatic emittance at $\lambda = 2.88$ nm in the water window, corresponding to the transition $1s^2 - 1s2p$ of the valence electron of the N^{5+} ion [126].

In the approach pursued in this work, the background pressure p_b is increased to several tens of mbar in order to generate a barrel shock in the supersonic jet. For this purpose, helium is utilized as background gas due to its high transmissivity of photons generated by the plasma. In addition, the optical path length of the resulting soft x-rays through helium is minimized by differential pumping. Another advantage of using helium as a surrounding gas is its large first ionization energy (24.6 eV) compared to that of nitrogen (14.5 eV) [127]. Thus, the critical power density to drive ionization by the incident laser beam is higher for helium, which ensures that only the target species nitrogen is ionized. Right behind the shock system generated in the jet, the particle density increases. In this manner, regions involving high densities of the target gas are obtained at comparably large distances from the nozzle. Thus, the plasma can be generated further away from the nozzle exit, and degradation effects are minimized.

4.2 GAS JET AND SOFT X-RAY DIAGNOSTICS

In order to characterize the supersonic gas jet and the evolving shock structure, two different methods are employed: the Schlieren technique for highly resolved qualitative imaging of density gradients and wavefront measurements with a Hartmann-Shack sensor in order to quantify the density distribution, but at a lower resolution. Both methods are described in detail in the following subsections 4.2.1 and 4.2.2.

The plasma is imaged by a pinhole camera and the number of the resulting soft x-ray photons is determined with a calibrated photo diode. A description of these tools follows in subsection 4.2.3.

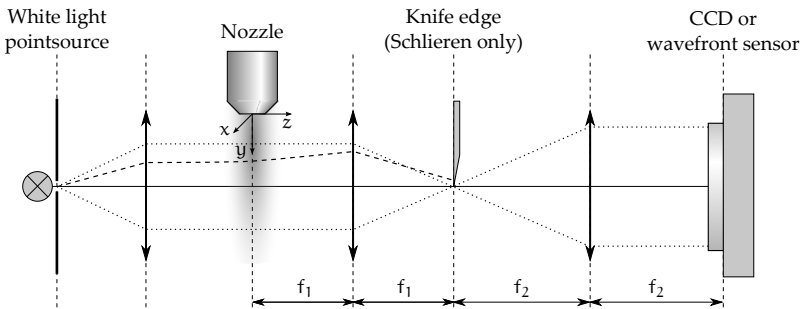


Figure 4.3: Experimental setup for Schlieren and wavefront measurements. The dotted lines represent the path of unrefracted light. The dashed line indicates a light ray which is refracted by varying distribution of gas density below the nozzle, thus hitting the knife edge and darkening the image. In order to monitor wavefront deformations, the CCD camera is replaced by a Hartmann-Shack sensor and the knife edge is removed.

4.2.1 Schlieren imaging

Schlieren imaging is a common technique in fluid dynamics which enables the qualitative measurement of density gradients [128]. The experimental setup is schematically shown in figure 4.3. A pinhole with a diameter of $100\ \mu\text{m}$ is illuminated by white light, and a focusing lens collimates the resulting beam, which then travels in z -direction through the gas distribution of the jet target. The xy -plane at $z = 0$ is imaged by a $4f$ setup to a CCD camera (Lumenera Lu160M) and captured with an exposure time of $50\ \mu\text{s}$. The camera is synchronized with the gas jet at a repetition rate of $10\ \text{Hz}$. Here, imaging lenses with focal lengths of $f_1 = 160\ \text{mm}$ and $f_2 = 300\ \text{mm}$

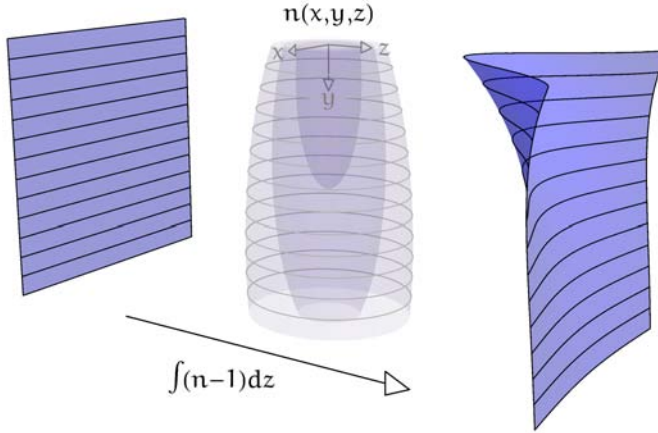


Figure 4.4: Wavefront deformation induced by the gas jet. The distribution of the optical density $n(x, y, z)$ increases the optical path length, resulting in the indicated wavefront deformation.

are used. A knife edge is moved close to the focal spot in between the two lenses, eliminating half of the spatial frequencies in the Fourier plane. The orientation of the blade determines which component of the density gradient will become visible. For example, as depicted in figure 4.3, a knife edge aligned with the x -axis generates contrast proportional to the gradient of the refractive index $\frac{\partial n}{\partial y}$ corresponding to the density gradient $\frac{\partial \rho}{\partial y}$. Note, however, that in the Schlieren images shown below, the knife edge is aligned with the y -axis so that density gradients within the jet are visualized in radial direction, thus emphasizing the barrel shock.

4.2.2 Wavefront monitoring

A Hartmann-Shack wavefront sensor [129, 130] is used to obtain quantitative information on the density distribution in the supersonic gas jet [59]. The experimental setup is mostly the same as that depicted in figure 4.3 for Schlieren imaging. However, the knife edge is removed and the CCD camera is replaced by the wavefront sensor. An initially plane wavefront of a test beam that travels through the target gas is deformed due to the spatial variation of the refractive index $n(x, y, z)$. The sensor splits the test beam into many sub-beams by an array of micro lenses, each producing a spot on a CCD camera (Lumenera Lu160M). The position of the spots contains the information of the local wavefront gradient. Thus, the

deformation of the wavefront can be recovered. The spatial resolution Δx of the deformation in the x -direction of a measured wavefront is equal to the pitch of the micro lens array $150 \mu\text{m}$ divided by the magnification factor $f_2/f_1 = 1.88$ of the $4f$ setup, yielding $\Delta x = 80 \mu\text{m}$.

The particle density distribution $N(x, y)$ in the nozzle plane $z = 0$ is recovered from a measured shape $w(x, y)$ of a deformed wavefront as follows. The test beam integrates $n(x, y, z)$ over the propagation direction z of the light beam, resulting in a difference $w(x, y)$ in the optical path, as illustrated in figure 4.4. Now it is assumed that in a plane corresponding to a constant $y = y_0$, $n(x, y_0, z)$ is approximated by a rotationally symmetric Gaussian shape with a maximum value $n_0(y_0) = n(0, y_0, 0)$. Then the deformation of the wavefront reads

$$\begin{aligned} w(x, y) &= \int [n(x, y, z) - 1] dz \\ &= \int [n_0(y) - 1] \cdot \exp\left(-\frac{x^2}{2\sigma(y)^2}\right) \cdot \exp\left(-\frac{z^2}{2\sigma(y)^2}\right) dz \\ &= [n_0(y) - 1] \cdot \sqrt{2\pi} \sigma(y) \cdot \exp\left(-\frac{x^2}{2\sigma(y)^2}\right). \end{aligned} \quad (4.1)$$

The standard deviation $\sigma(y)$ of $n(x, y, z)$ is determined from the shape of the measured deformation of the wavefront $w(x, y)$ by a Gaussian fit. The distribution of the refractive index in the plane $z = 0$ containing the jet axis is recovered by

$$n(x, y, 0) - 1 = \frac{w(x, y)}{\sqrt{2\pi} \sigma(y)}. \quad (4.2)$$

Conversion of the refractive index $n(x, y, 0)$ into a particle density N is done by using the Lorentz-Lorenz formula [110]

$$\frac{n^2 - 1}{n^2 + 2} = \frac{4}{3} \pi \alpha N, \quad (4.3)$$

where α , the polarizability of the considered gas particles, is derived using the values $n = 1.0002974$ and $N = 2.69 \cdot 10^{19} \text{cm}^{-3}$ for nitrogen under normal conditions [127] (at a temperature of 273.15 K and a pressure of 1013.25 mbar). In these calculations, the surrounding helium atmosphere is neglected because of its low refractive index which amounts to only a few percent as compared to that of the nitrogen jet.

4.2.3 Plasma characterization

Qualitatively, the plasma is characterized by a pinhole camera system as sketched in figure 4.5(a). It consists of a phosphor coated CCD camera (Lumenera Lu160M with 3 layers of phosphor P43 with a grain size of $\approx 1 \mu\text{m}$) in combination with a titanium-filtered pinhole (100 μm diameter, Ti-layer 200 nm thick). This way, the intensity distribution of radiation at the wavelength $\lambda = 2.88 \text{ nm}$ is captured. Here, the luminescent area A is approximated by an ellipsoidal shape with the semi-axes a and b . Then, $A = \pi a b$, where a and b are defined as the full-widths at half-maximum of the intensity in x - and y -direction. The uniformity of the plasma is characterized by its eccentricity $\epsilon = \sqrt{a^2 - b^2}/a$. Examples of the intensity images are shown in figure 4.9 in combination with the corresponding Schlieren images of the gas jet for the case of both, gas issuing into vacuum and gas issuing into a background gas and thus forming a barrel shock.

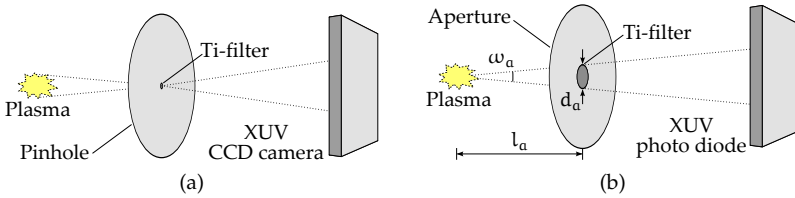


Figure 4.5: Principle of plasma characterization by pinhole camera (a) and diode measurement (b).

Quantitatively, the peak brilliance Br of the plasma is derived by

$$Br = \frac{N_{\text{ph}}}{\tau \Omega A} \quad (4.4)$$

with the pulse duration τ , the solid angle Ω and the source area A . The number of photons N_{ph} with a wavelength of $\lambda = 2.88 \text{ nm}$ is determined by a calibrated XUV photo diode (International Radiation Detectors, AXUV100) which is equipped with a titanium filter (thickness 200 nm, applied to a nickel mesh with transmissivity of 0.89). As shown in figure 4.5(b), only these photons reach the detector which propagate within a cone confined by a circular aperture with diameter d_a in a distance l_a to the plasma. Thus, the solid an-

gle is defined by the corresponding opening angle $\omega_a = 2 \tan \frac{d_a/2}{l_a}$ of the cone [131]

$$\Omega = 4\pi \sin^2 \frac{\omega_a}{4}. \quad (4.5)$$

In good approximation, the lifetime of the plasma is assumed to be $\tau = 6$ ns, which equals the duration of the exciting laser pulse. Finally, the luminescent area A is determined with a pinhole camera as described above.

4.3 EXPERIMENTAL RESULTS

First, the gas jet and the effect of a background pressure on the resulting flow structure are investigated using the techniques described in the previous section. The derived results are compared to theoretical relations discussed in section 2.1.2. Subsequently, the effect of the barrel shock on the plasma generation is explored and the brilliance improvement of the soft x-ray source is quantified.

4.3.1 Characterization of the target gas jet

Depending on the stagnation and background pressure, the gas jet may form various shapes, which are discussed in the following. In previous studies of laser-produced soft x-ray sources the nozzle was operated in the range $p_0 = 11 \dots 17$ bar at a background pressure of $p_b = 10^{-4}$ mbar, i.e., practically without any background gas. In this case, the emerging flow is in the scattering regime and does not show any discontinuities. Independently of p_0 the density distribution has a maximum value at the nozzle exit and rapidly falls off in all directions. Corresponding Schlieren images are taken with the knife edge aligned with the y -axis and can be found in figure 4.6 for the pressure range $p_0 = 11 \dots 17$ bar.

With rising background pressure, particle collisions increasingly affect the gas jet and retard its free expansion. At a certain distance from the nozzle, this results in a shock which is directly connected to a local decrease of the Mach number M . At the same time, the local particle density increases. This becomes evident in regions in the Schlieren images that show strong changes in intensity, implying high density gradients. As can be seen, for example, in figure 4.6(b), the shape of the resulting shock structure resembles a barrel, why it is referred to as a barrel shock. In the downstream direction, the barrel shock is terminated by the Mach disk, which is indicated

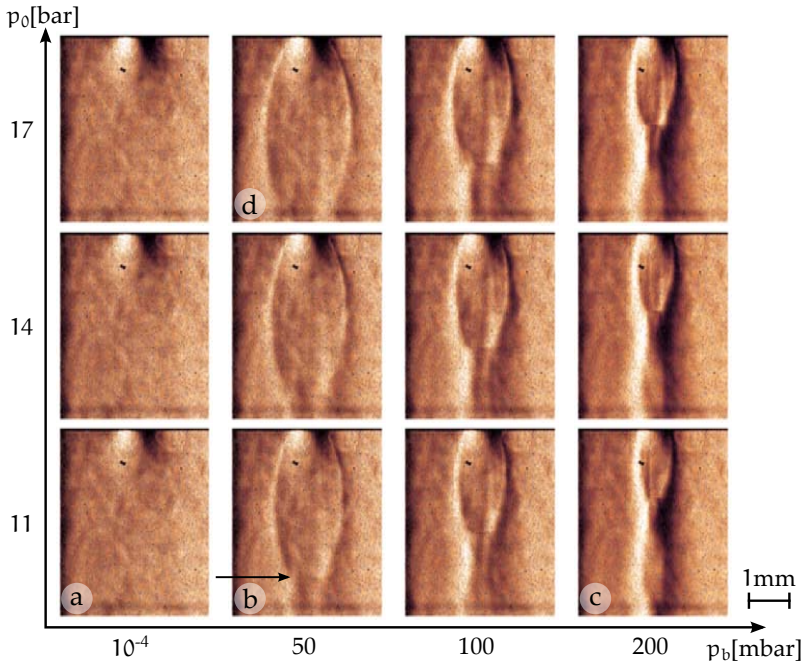


Figure 4.6: Schlieren images indicating the supersonic flow structure of a N_2 jet as a function of stagnation and background pressure (flow direction: top \rightarrow bottom).

(a) Scattering regime, no internal structures evolve; (b) continuum regime with barrel shock structure, the Mach disk is indicated by the arrow; (b) \rightarrow (c) shock structure contracts for increasing background pressure; (b) \rightarrow (d) shock structure inflates for increasing stagnation pressure.

in the Schlieren image by an arrow. In the present Schlieren pictures, the Mach disk is reproduced only weakly because the knife edge was aligned perpendicular to the disk and only density gradients parallel to the disk were detected.

Increasing p_b , as from figure 4.6(b) to 4.6(c), results in a confinement of the gas flow towards the nozzle axis - the lateral shocks approach each other and the Mach disk moves upstream. In contrast to this, increasing p_0 has the opposite effect, i.e., the radius of the barrel shock and the width σ of the density distribution increase and the Mach disk moves downstream, see figures 4.6(b)-(d). These two opposite effects allow generation of the same shock structure at different combinations of the pressures, provided that the ratio p_0/p_b stays constant.

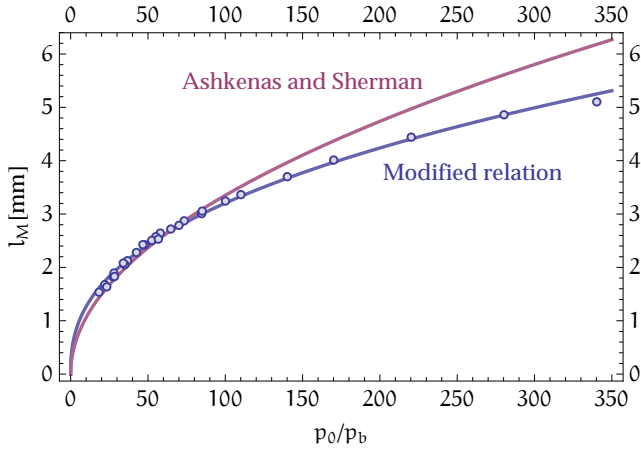


Figure 4.7: Distance between Mach disk and nozzle exit for various pressure ratios. The points are derived from Schlieren images, the violet curve represents the empirical relation (2.11) from Ashkenas and Sherman [61] and the blue curve represents the modified relation given in equation (4.6) with $\alpha = 0.4034$.

From Schlieren images as shown in figure 4.6, the distance l_M between Mach disk and nozzle throat is derived for pressure ratios in the range $18 \leq p_0/p_b \leq 340$. In figure 4.7, the resulting data set is compared to the empirical relation (2.11)

$$l_M = 0.67 \cdot d_e \left(\frac{p_0}{p_b} \right)^{1/2}$$

which has been derived by Ashkenas and Sherman [61] for a non-divergent nozzle. Apparently, the experimental results deviate from the depicted curve, especially for large pressure ratios. Most likely, this can be attributed to a different nozzle geometry as in the present situation. Here, a divergent orifice initially guides the supersonic expansion of the gas before it expands freely into the helium atmosphere. For that case, a relation of the form

$$l_M = d_e \left(\frac{p_0}{p_b} \right)^\alpha \quad (4.6)$$

reveals good agreement with the measured shock distances as it is evident in figure 4.7. By a least-squares fit routine [132] the exponent is derived to $\alpha = 0.4034$.

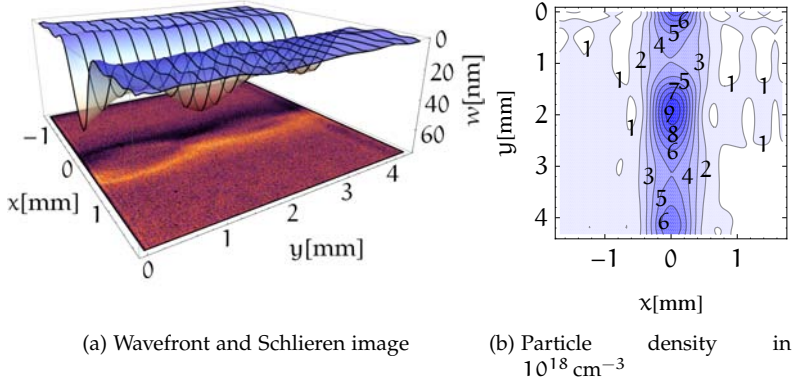


Figure 4.8: (a) Combination of quantitative wavefront and qualitative Schlieren image of the N_2 jet expanding from $p_0 = 11$ bar into a He atmosphere with $p_b = 170$ mbar. (b) Density distribution $N(x, y)$ of the N_2 jet in the plane $z = 0$, which results from the wavefront as described in section 4.2.2.

In figure 4.8, wavefront and Schlieren measurements are compared with each other for a stagnation pressure of $p_0 = 11$ bar and a background pressure of $p_b = 170$ mbar. The results of both techniques are well consistent. The particle density $N(x, y)$ shows the mean gas distribution inside the jet. In the downstream direction, along the nozzle axis, N first decreases to $N_{\min} = 4.0 \cdot 10^{18} \text{ cm}^{-3}$ and then increases again up to a maximum value of $N_{\max} = 9.8 \cdot 10^{18} \text{ cm}^{-3}$. Subsequently, the wave-like behavior of the particle density is repeated at lower density values. The observed maxima coincide approximately with the positions where the lateral shocks interfere, forming a Mach disk.

Employing the relations of gas dynamics introduced in section 2.1.2, a rough theoretical estimate of the particle density N_{\max} ahead and behind the Mach disk is now compared to the results obtained with the wavefront sensor. Corresponding to the experimental situation, the density distribution along the symmetry axis of the gas jet is depicted in terms of its stagnation value ρ_0 in figure 2.7. There, a normal shock induces a density increase from $\rho_{\min} = 0.039 \rho_0$ to $\rho_{\max} = 0.170 \rho_0$ in a distance of $l_M = 2.7$ mm to the nozzle throat. For the current pressure ratio of $p_0/p_b = 64.7$, this coincides with the position of the Mach disk.

In order to derive absolute density values, the stagnation density ρ_0 of the nitrogen jet is required. Following the ideal gas law

$p_0 = \rho_0 R_{sp} T_0$ results in $\rho_0 = 12.65 \text{ kg/m}^3$ with the specific gas constant for nitrogen $R_{sp, N_2} = 296.8 \text{ J}/(\text{kg} \cdot \text{K})$ [127], the temperature $T_0 = 293 \text{ K}$ and pressure $p_0 = 11 \text{ bar}$ inside the vessel. Finally, particle densities ahead and behind the Mach disk are evaluated with the molecular mass of nitrogen $m_{N_2} = 4.653 \cdot 10^{-26} \text{ kg}$ [127]. A comparison between the theoretical estimation and the measured values is given in table 4.1.

Table 4.1: Particle density ahead (N_{\min}) and after (N_{\max}) the barrel shock, given on the symmetry axis of the jet. Comparison between theoretical estimate and measurement.

	Theor. estimate	Measurement
$N_{\min} [10^{18} \text{ cm}^{-3}]$	10.6	4.0
$N_{\max} [10^{18} \text{ cm}^{-3}]$	46.1	9.8

The estimated values are of the same order of magnitude but larger than the experimental results. This discrepancy can be attributed to the spatial resolution of the wavefront sensor which is not able to resolve the high density value right behind a shock. Furthermore, the estimate provides an upper limit of the particle density, since in a simplification, a conical source flow has been assumed. In fact, the stream lines of the flow are bended in lateral direction, stronger than the cone geometry presumes. Consequently, this results in a higher rarefaction of the gas and the typical bulbous barrel shock. This explains why values of the estimated particle densities, both of the maximum and the minimum, are higher than the corresponding measured values.

4.3.2 Characterization of the plasma enhancement

The effect of an increase in target gas density on the plasma generation is illustrated in figure 4.9 for a stagnation pressure of $p_0 = 11 \text{ bar}$. Taking advantage of the barrel shock, obviously the brightness of the plasma is raised, whereas its size has decreased in the direction of the incident laser beam. Due to the increased target density, there are more emitters of soft x-ray radiation in the same volume. Besides, the absorption of laser energy is raised. Thus, the power density of the beam decreases more rapidly below its critical value and no further atoms are ionized. This confines the size of the plasma in the beam direction and explains its smaller size. Another mechanism causing the reduced size might be plasma defocusing

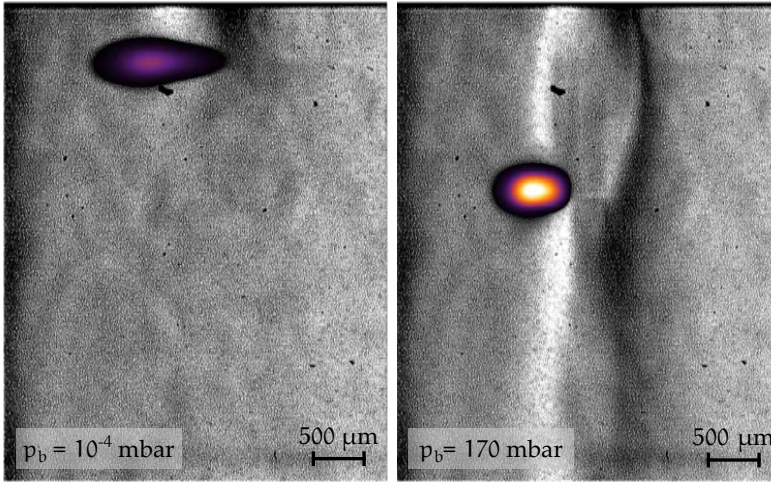


Figure 4.9: Pinhole camera images of the plasma superimposed on Schlieren images of gas jet at $p_0 = 11$ bar. Left: under vacuum conditions $p_b = 10^{-4}$ mbar. Right: with ambient He atmosphere $p_b = 170$ mbar. Both plasma images are an average of 30 single-shots.

[133]. Due to an increased plasma density, a stronger defocusing effect can be expected, limiting the ionization region.

During the experiments it turned out that generation of a plasma right below the Mach disk, where the density is expected to be at a maximum, is not the optimal position. It was found that even brighter and smaller plasmas occur when the laser is focused onto the edge of the jet at a location slightly above the Mach disk and after the barrel shock (see figure 4.9). This behavior may be caused by reabsorption of soft x-rays by the surrounding nitrogen particles. The barrel shock is enclosed by a thin supersonic compressed layer, which becomes thicker at the Mach disk [19], leading to increased reabsorption.

In order to study the brilliance improvement depending on the location of plasma generation with respect to shock structures in the jet, the latter were varied by changing the background pressure at a constant stagnation pressure ($p_0 = 11$ bar). By lowering p_b , the radius of the barrel shock is increased; conversely, with increasing p_b , the radius of the barrel shock decreases. Thus, with the location of the focus of the laser beam fixed, its relative location with respect to high-density regions behind the shock is changed. In figure 4.10, intensity distributions of the plasma are shown for various

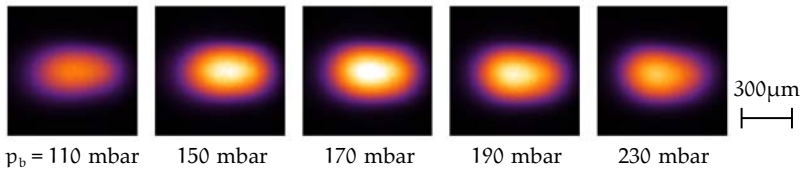


Figure 4.10: Pinhole camera images of the plasma at a stagnation pressure of $p_0 = 11$ bar for various background pressures p_b as given below the individual figure. The average of 30 single-shots is shown.

background pressures p_b . In this, the location of plasma generation is kept constant. An optimum is found at $p_b = 170$ mbar (see also figure 4.9).

Unexpectedly, increasing both p_0 and p_b while preserving the pressure ratio p_0/p_b , does not lead to a considerable further increase of the brilliance of the source. Approaching high pressure values ($p_0 \rightarrow 17$ bar), quite the reverse happens: the plasma appears even darker. It can be assumed that, in fact, more soft x-ray photons are generated since the target density is increased. However, the density of the background gas is increased as well, which leads to higher reabsorption of the generated photons. The latter effect seems to dominate the former. It is expected that further efforts at differential pumping can shorten the path length of the soft x-rays through the outer helium gas so that the brilliance of the source can further be increased.

Now, parameters characterizing the plasma in the optimal case are compared with those of a plasma produced near the nozzle exit with a jet in the scattering regime. In both cases the same stagnation pressure of $p_0 = 11$ bar is considered. Regarding the shape of the resulting plasma, which is represented by its luminescent area, it can be seen that the radiating area is reduced by a factor of 0.71 to $A = 0.063 \text{ mm}^2$, and its eccentricity decreases slightly from $\epsilon = 0.91$ to $\epsilon = 0.80$ when a barrel shock is present. This results in better brilliance and improves the coherence properties due to a smaller source size and a more uniform shape. The number of photons emitted per pulse and solid angle from the nitrogen plasma at a wavelength of $\lambda = 2.88 \text{ nm}$ is raised by a factor of 7.1 to a value of $1.2 \cdot 10^{13} \text{ sr}^{-1}$. Based on these values the peak brilliance can be computed. One finds an improvement by a factor of 10 to a value of $\text{Br} = 3.15 \cdot 10^{16} \text{ photons}(\text{mm}^2 \text{ mrad}^2 \text{ s})^{-1}$. This clearly

demonstrates the advantage of utilizing the density increase across a barrel shock system. An overview of the characteristic parameters of the plasma is given in table 4.2.

Table 4.2: Comparison of plasma emission characteristics at $\lambda = 2.88$ nm obtained with a nitrogen jet issuing into vacuum (no barrel shock) and into a background gas (with barrel shock).

	Without barrel shock	With barrel shock	Factor
Radiating area [mm ²]	0.088	0.063	0.71
Eccentricity [1]	0.91	0.80	0.88
Photons/(solid angle · pulse) [sr ⁻¹]	$1.66 \cdot 10^{12}$	$1.18 \cdot 10^{13}$	7.10
Peak brilliance [mm ⁻² mrad ⁻² s ⁻¹]	$3.15 \cdot 10^{15}$	$3.15 \cdot 10^{16}$	10.0

The high harmonic generation process converts electromagnetic radiation into harmonics corresponding to integer multiples of the fundamental frequency. All individually quasi-monochromatic harmonics propagate collinearly with the incident laser beam. The latter can be efficiently blocked by a thin metal filter which is transparent to the generated EUV radiation [134]. In order to prepare a beam which contains only a few or even single harmonics, multilayer mirrors with a wavelength-selective reflectivity are used [135]. Similarly, a reflection grating acts on the HHG beam by separating the harmonics into different diffraction angles [136]. Both techniques can be combined with curved surfaces to refocus the divergent HHG radiation to a probe position. However, such devices are always a source of wavefront aberrations in case of slight misalignments. As a result the radiation is not concentrated into the smallest possible focus and the intensity on the probe does not reach its optimum value.

In this chapter, the propagation of single harmonics is studied after passing a monochromator arrangement that aims to conserve the pulse length. Aberrations contained in the resulting beam are identified by the measurement of wavefronts and intensity profiles.

In a second part, the wavefront sensor is used for the alignment of a toroidal grating that acts as both, as a monochromator and as a focusing optic. Corresponding to the experiment, the astigmatic aberration induced by that element is studied theoretically by matrix methods.

Partly, the content of this chapter has been published already [137]. All experiments have been conducted in close collaboration with C. Ropers and S. Zayko at the HHG source of the University of Göttingen.

5.1 CHARACTERIZATION OF HIGH HARMONIC BEAM

5.1.1 *Experimental setup*

The setup of the investigated HHG source is schematically depicted in figure 5.1. A titanium sapphire laser generates ultra-short pulses of infrared radiation which are focused into an argon filled capillary (pulse energy 0.5 mJ, pulse length 40 fs, mean wavelength 800 nm, repetition rate 1 kHz). In the noble gas, the highly non-linear HHG process results in odd harmonics up to the 51st order. After the conversion, the fundamental beam is absorbed by a mesh-less aluminum filter of 200 nm thickness. However, radiation in the spectral range $17 \text{ nm} < \lambda < 60 \text{ nm}$ passes the filter (transmissivity > 0.6) [138]. A toroidal grating generates a row of individual foci for each harmonic (Jobin Yvon, reference number 540 00 910, sagittal radius $R_s = 104.9 \text{ mm}$, tangential radius $R_t = 1000 \text{ mm}$, groove density $g = 550 \text{ mm}^{-1}$, focal length in 0. order $f_{\text{tor}} = 160 \text{ mm}$). In $-1.$ diffraction order, a slit allows propagation of single harmonics while all others are blocked. In the investigated setup, an identical toroidal grating ensures the preservation of the ultra-short pulse duration [139]. It focuses and diffracts the beam again, whereby in $+1.$ diffraction order the optical path difference is compensated. Throughout the entire setup, ultra high vacuum conditions are maintained, whereas the fundamental laser beam is coupled into the system via a vacuum window.

For all demonstrated experiments, the 25th harmonic has been selected corresponding to a wavelength of $\lambda = 32 \text{ nm}$.

In the present investigation, two diagnostic tools are employed for beam characterization, an EUV sensitive CCD camera and a Hartmann type wavefront sensor [140, 113]:

- The chip of the CCD camera contains 1392×1040 square pixels with an edge length of $6.45 \mu\text{m}$ which provide a dynamic range of 14 bit (SHT MR285MC). By a coating of a $4 \mu\text{m}$ thick phosphor layer (P43 with a grain size $\approx 1 \mu\text{m}$) EUV radiation is converted into visible light. A movable support allows manual positioning of the system in a range of 200 mm around the focal position. During the experiment, intensity profiles are captured at 40 different equidistant positions within an exposure time of 8 s, thus comprising 8000 pulses of HHG radiation.

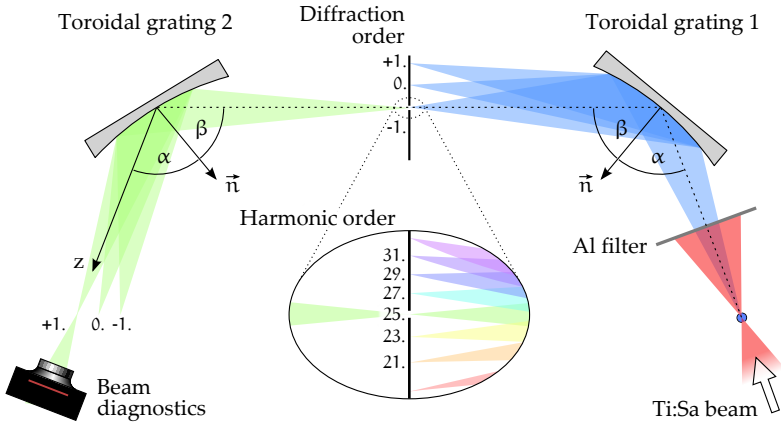


Figure 5.1: Setup of HHG source with two toroidal gratings in an arrangement for compensation of the optical path difference. \vec{n} denotes the normal vector of the toroidal surface and the indicated angles are $\alpha = 72.55^\circ$ and $\beta = 69.45^\circ$.

- o The Hartmann sensor is a combination of a back-thinned CCD chip (Princeton Instruments PI-MTE: 1300B, 1340×1300 square pixels, edge length $20 \mu\text{m}$, dynamic range 16 bit) with a pinhole array in a distance of 95 mm to the chip (pinhole diameter $75 \mu\text{m}$, pinhole pitch $250 \mu\text{m}$). The device is placed 420 mm behind the expected focal position of the HHG beam. In order to accumulate a sufficient signal, an illumination time of 200 s is necessary.

When the EUV beam reaches the pinhole array, it is divided into many small sub-beams which then propagate individually in the direction of the local Poynting vector, each producing a spot on the CCD chip. The wavefront is then reconstructed by a comparison between the resulting spot distribution and a reference distribution which is produced by a plane wave. A detailed description of the principle of that sensor is found in [113]. Here, an absolute reference is employed that is generated numerically with Gaussian spots which are separated by $250 \mu\text{m}$ in both directions, horizontally and vertically.

5.1.2 Evaluation of intensity profiles

A selection of intensity profiles of the 25th harmonic beam is shown in figure 5.2. Here, the z -coordinate denotes the distance to the second grating. The vertical and horizontal focus positions are represented by sub-figures 5.2(b) and 5.2(c), corresponding to $z =$

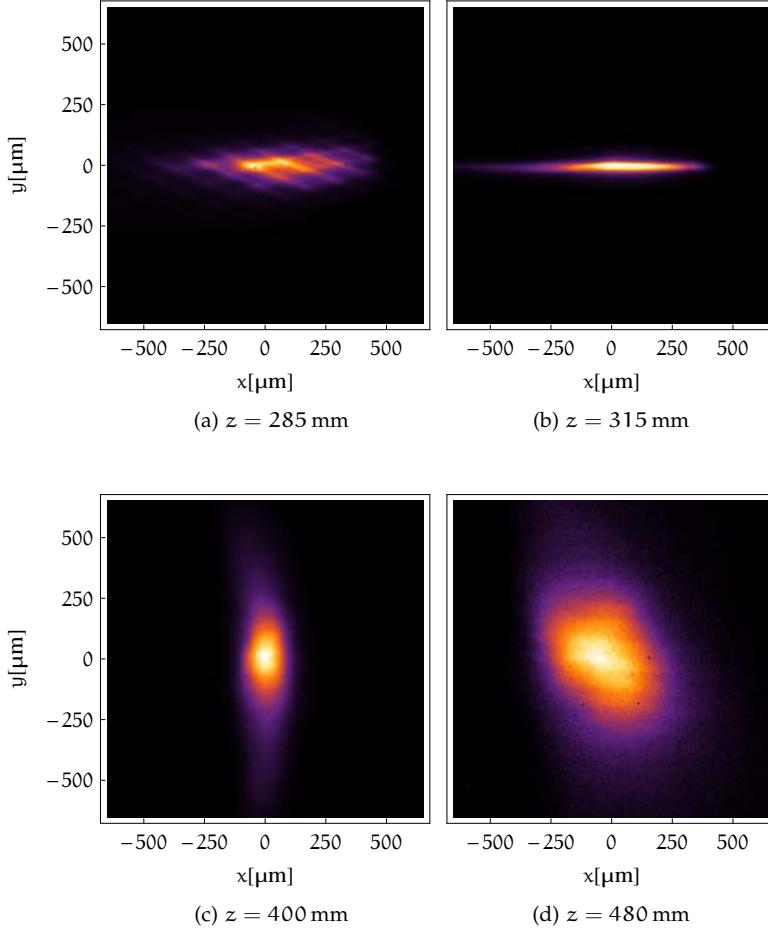


Figure 5.2: Normalized intensity profiles of the 25th harmonic ($\lambda = 32$ nm) at arbitrary positions, where (b) and (c) represent vertical and horizontal focus position, respectively.

315 mm and $z = 400$ mm. Apparently, both positions do not coincide, revealing a strong astigmatic aberration.

Regarding the first intensity profile at $z = 285$ mm, a substructure of diagonal bright lines is evident. This pattern vanishes in the following beam profiles. It is possible that the grid structure is present on the surface of the first toroid and is imaged by the second toroid to the camera. Following the lens equation [141], the corresponding imaging plane is found at $z = 213$ mm which is close to the position of the observed profile. Likewise, it is possible that this pattern is originating from the aluminum filter.

After computing the second order moments $\langle x^2 \rangle$ and $\langle y^2 \rangle$ of the intensity distributions, the local beam diameters d_x and d_y are derived by equation (3.5). A least squares fit routine [132] employing hyperbolic functions $d_x(z)$ and $d_y(z)$ as given in equation (3.9) yields waist position z_0 , waist diameter d_0 and beam divergence θ separately for horizontal and vertical direction. An overview of the beam parameters is given later in table 5.1 and an illustration of these results is shown in figure 5.3. Additionally, the figure comprises the mean irradiance, which is derived by $P_0/A(z)$, where P_0 is an arbitrary beam power and $A(z) = \frac{\pi}{4} d_x(z) d_y(z)$ is the beam area approximated by an ellipse.

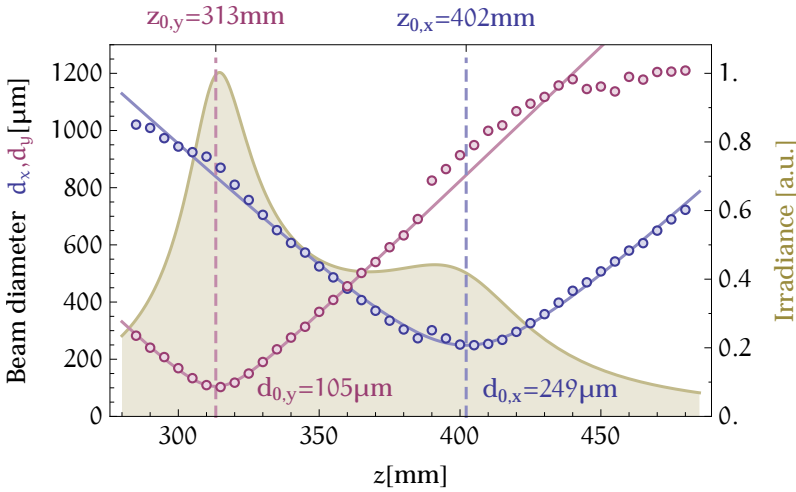


Figure 5.3: Local beam diameters of the 25th harmonic ($\lambda = 32$ nm) in proximity of the focus positions. Blue and violet dots represent measured values, the corresponding lines show the hyperbolic fit functions $d_x(z)$ and $d_y(z)$. The mean irradiance depicted in yellow color is computed employing $d_x(z)$ and $d_y(z)$.

The experimental data shows a small inconsistency at $z = 390$ mm, which can be explained by the experimental procedure. During the measurement a spacer has been employed to double the accessible interval and thus, the vacuum chamber had to be vented. Afterwards, the situation might slightly differ. Besides, for large beam diameters $d_x > 1000$ μm the experimental values are below the hyperbolic prediction, which can be attributed to the noise level of the camera: if the beam size increases, the signal-to-noise ratio decreases and regions with weak intensity become undetectable resulting in an underestimation of the diameter.

The results reveal a strong astigmatic aberration which is resembled by a difference in waist positions of $\Delta z = z_{0,x} - z_{0,y} = 89$ mm. As a consequence, the photons are not concentrated into the smallest possible spot and the irradiance does not reach its optimum value. The course of the computed mean irradiance nicely unveils the most intense beam position which is situated shortly behind the vertical waist position. In case of a coincidence of both waist positions, the attainable flux density would increase by a factor of 3.3. This can be realized by an adjustment of the toroidal grating which will be discussed in the upcoming section 5.2.

It is evident, that the waist diameter in horizontal direction $d_{0,x} = 249$ μm is significantly larger than in vertical direction $d_{0,y} = 105$ μm . This fact stands in contrast to the expectations: independently from the astigmatic aberration, the optical system should produce similar waist diameters. Considering the transport of a non-monochromatic beam through the arrangement, it results that a finite spectral width leads to the observed spatial broadening. This phenomenon is also denoted as *spatial chirp*. In the following, the effect is demonstrated considering a comparable collinear setup where the toroidal gratings are replaced by optical elements that combine the action of a lens and a transmissive grating, as shown in figure 5.4.

The optical path through the depicted system is described in terms of a two-dimensional light ray $\vec{r} = (x, u)$. While the lens modifies the angle u depending on the distance x to the optical axis, the grating changes u , independently of x , according to the grating equation [1], which reads in the paraxial approximation

$$u' = u + m g \lambda \quad (5.1)$$

where u is the incidence angle, u' the diffraction angle (both with respect to the optical axis), m the diffraction order and g the grating constant.

In summary, three different transformations act on \vec{r} :

- Propagation by a distance z $\begin{pmatrix} x \\ u \end{pmatrix} \rightarrow \begin{pmatrix} 1 & z \\ 0 & 1 \end{pmatrix} \begin{pmatrix} x \\ u \end{pmatrix}$
- Lens with focal length f $\begin{pmatrix} x \\ u \end{pmatrix} \rightarrow \begin{pmatrix} 1 & 0 \\ -1/f & 1 \end{pmatrix} \begin{pmatrix} x \\ u \end{pmatrix}$
- Grating $\begin{pmatrix} x \\ u \end{pmatrix} \rightarrow \begin{pmatrix} x \\ u + m g \lambda \end{pmatrix}$

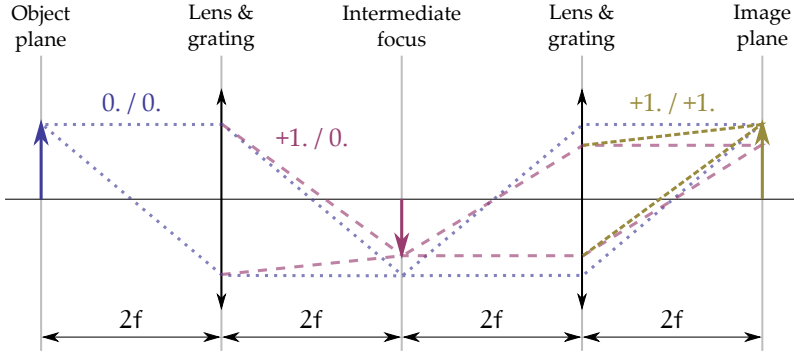


Figure 5.4: Optical path through an arrangement of two identical focusing gratings for different diffraction orders. A 1-to-1 imaging is achieved if both gratings operate in the same order. In case of differing orders (e.g. +1./0.), a light ray is imaged to a wavelength dependent position.

Applying a propagation by $2f$ to the initial light ray \vec{r} , followed by the lens matrix, the grating transformation and another propagation by $2f$ leads to a modified light ray at the intermediate position between both optical elements. A repetition of these transformations results in the ray vector \vec{r}' at the expected focal position behind the system. In case that both gratings operate in 0^{th} order, a 1-to-1 imaging is achieved and $\vec{r} = \vec{r}'$. Considering both gratings acting in different combinations of diffraction orders, a light ray originating from position x is imaged as follows:

- +1./0. order $x \rightarrow x - 2 f g \lambda$
- +1./-1. order $x \rightarrow x - 4 f g \lambda$
- +1./+1. order $x \rightarrow x$

Apparently, light that follows the path of +1./0. diffraction order is imaged from its initial position x to a wavelength dependent location $x - 2 f g \lambda$. This implies that the focus of a non-monochromatic beam becomes broadened depending on its spectrum. Counterintuitively, in +1./-1. order this effect is not compensated but doubled. In contrast, a ray that is diffracted in +1./+1. order undergoes a 1-to-1 imaging, as sketched in figure 5.4.

Now, an estimation is given for the lateral chirp due to the spectral properties of the HHG radiation as observed in the experiment. In the literature, harmonic pulses of the 27th order generated by a comparable laser system are observed to have a finite spectral width of 0.24 eV corresponding to $\Delta\lambda/\lambda = 0.006$ [142, 143]. For the present

wavelength of $\lambda = 32$ nm this results in a bandwidth of $\Delta\lambda = 0.2$ nm. The linear dispersion relation in a distance l_{gr} to a grating is [141]

$$D = \frac{\Delta\lambda}{\Delta x} = \frac{\cos \beta}{m g l_{gr}} \quad (5.2)$$

where β denotes the deflection angle, m is the diffraction order and g the groove density. For the current geometry, it takes values of $D = -1.99 \frac{\text{nm}}{\text{mm}}$ and $D = 1.7 \frac{\text{nm}}{\text{mm}}$ in respective focal planes of first and second grating. Note, that the deflection angle is different for both gratings (69.45° and 72.55°). This results in a total spatial broadening of $\Delta x = 100 \mu\text{m} + 120 \mu\text{m}$, i.e., the spectrum of a single point is projected to a $220 \mu\text{m}$ broad intensity distribution. In order to quantify the broadening of the entire focal spot, each point of it must be considered. Mathematically, this resembles a convolution. Convoluting two Gaussians with the standard deviation σ_1 and σ_2 , respectively, results in a Gaussian with the standard deviation $(\sigma_1^2 + \sigma_2^2)^{1/2}$. Applying that relation to assess the diameter of the chirped intensity distribution leads to

$$\sqrt{d_{0,y} + \Delta x} = 244 \mu\text{m} \quad (5.3)$$

standing in excellent agreement to the observed value of $d_{0,x} = 249 \mu\text{m}$.

5.1.3 Results from wavefront measurement

Under the same experimental settings as during the caustic scan, the beam of the 25th harmonic is investigated by the wavefront sensor, too. From the measured spot pattern the employed evaluation software [144] computes the wavefront in terms of a linear superposition of the Zernike polynomials. Under the assumption of full coherence, beam parameters such as waist diameter, divergence or astigmatic waist difference are derived [145]. In the following these properties are compared to the results from the precedent caustic scan.

The wavefront of the 25th harmonic is depicted in figure 5.5 where tilt and defocus terms have been subtracted. The surface resembles a saddle indicating a dominant astigmatic aberration. The related difference in waist positions is computed to $\Delta z = 91$ mm, standing in good agreement to the value $\Delta z = 89$ mm which is obtained by

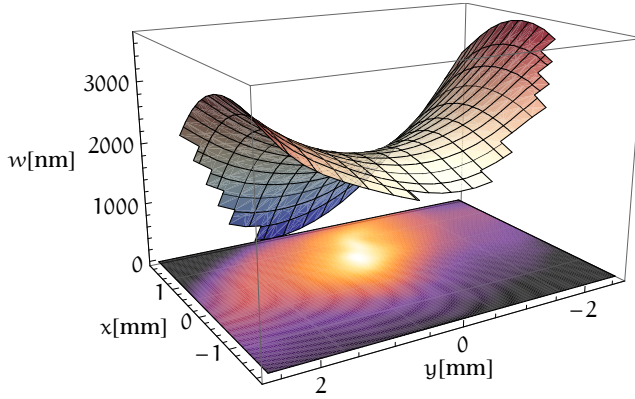


Figure 5.5: Wavefront of the 25th harmonic in a distance of 420 mm behind the expected focus position of the system, where tilt and defocus aberrations have been subtracted. Below, the intensity profile of the HHG beam is indicated.

the evaluation of intensity profiles. Waist diameter and beam divergence are derived as well, and a comparison of the beam parameters resulting from caustic and wavefront measurement is given in table 5.1.

Both techniques agree well to each other in all parameters except for the horizontal waist diameter $d_{0,x}$. Compared to the wavefront measurement, the value resulting from the caustic scan is twice as large. Again, this discrepancy can be attributed to the lateral chirp introduced by the gratings. For the wavefront sensor the focus behind the second grating appears as a virtual source which is horizontally broadened due to dispersion. This effectively reduces the horizontal degree of coherence. Nonetheless, the beam parameters are derived from the wavefront under the assumption of full

Table 5.1: HHG beam parameters for the 25th harmonic ($\lambda = 32$ nm). Comparison between results from caustic scan and wavefront measurement.

	Astigmatic waist difference	Waist diameter	Divergence
	Δz [mm]	$d_{0,x} / d_{0,y}$ [μm]	θ_x / θ_y [mrad]
Caustic	89	249 / 105	9.0 / 9.4
Wavefront	91	124 / 136	8.9 / 8.5

coherence and thus, the obtained waist diameter becomes underestimated for the x -direction.

This effect can nicely be illustrated by the individual spots which are captured by the wavefront sensor. The Hartmann sensor can be considered as an array of pinhole cameras. Illuminated by the HHG beam, each sub-aperture produces an image of the virtual source on the CCD camera, see figure 5.6. Apparently, the grating configuration that preserves the pulse length (-1./+1. order) leads to spots which appear horizontally elongated. With a higher resolution, this would resemble the spectrum of the 25th harmonic. In contrast, choosing 0. diffraction order for both gratings, no dispersion is introduced to the beam and the spots become round.

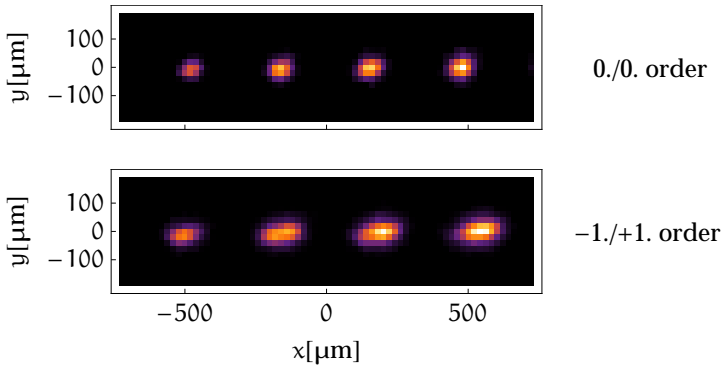


Figure 5.6: Individual images of the 25th harmonic captured by different sub-apertures of the wavefront sensor, i.e., images of the virtual source behind the monochromator. Below, a chirped pulse results in broadened spots resembling the finite spectral bandwidth. Above, the chirp is avoided by choosing 0. diffraction order for both gratings.

5.2 ALIGNMENT OF TOROIDAL GRATING

The alignment of a single grating is demonstrated experimentally by online measurements of the wavefront. Subsequently, simple calculations employing matrix methods provide a theoretical validation of the observed results.

5.2.1 The experiment

In a prospective application, the HHG radiation of the investigated setup should be employed for coherent diffractive imaging experiments. For this, an ultra-short EUV pulse length is not necessary unless ultrafast dynamic processes shall be investigated. Thus, in the following the intermediate focus is provided as sample position where at least 20 times more photons are available (the diffraction efficiency of the grating into $-1.$ or $+1.$ order amounts to less than 5%). Additionally, with a single grating, the linear dispersion is reduced by $\approx 50\%$ leading to a smaller horizontal waist diameter. In order to further optimize that simplified setup, aberrations in the 25th harmonic are characterized by the wavefront sensor as sketched in figure 5.7. Here, due to the increased beam intensity, the highly sensitive back-illuminated camera is replaced by a phosphor coated CCD offering smaller pixels. Detailed specifications of both cameras are given in section 5.1.1.

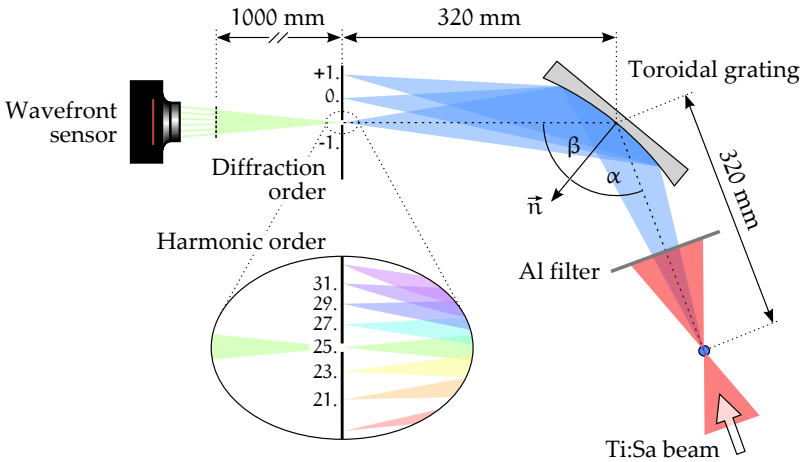


Figure 5.7: Setup of HHG source with a single toroidal grating acting as monochromator. \vec{n} denotes the normal vector of the toroidal surface.

During online monitoring of the wavefront, the incidence angle α between the HHG beam and the normal of the toroid is slightly increased in steps of $\Delta\alpha = 0.05^\circ$. The deflection angle β changes according to the grating equation [1]

$$\sin \beta - \sin \alpha = m g \lambda \quad (5.4)$$

with diffraction order m and groove density g . In the course of this alignment procedure, the effective radius of the optic decreases in tangential direction and it increases in sagittal direction. As a consequence, the beam experiences a stronger horizontal focusing and a weaker vertical focusing. For a certain incidence angle α_0 , both focal distances equal each other and the foci coincide. A selection of three wavefronts captured at different angles α is depicted in figure 5.8.

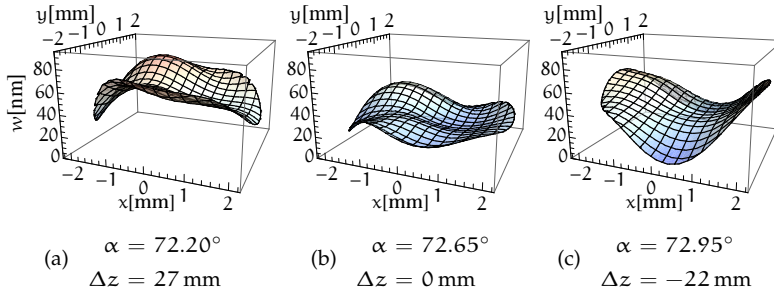


Figure 5.8: HHG wavefront of 25th harmonic for different incidence angles α with the resulting astigmatic waist difference Δz . Here, tilt and defocus terms are subtracted.

Apparently, already small variations of the incidence angle lead to a significant change of the astigmatic aberration. The curvature of the wavefront indicates that at an incidence angle of $\alpha = 72.20^\circ$, the beam is horizontally divergent and vertically convergent. At $\alpha = 72.95^\circ$ the situation appears vice versa. Thereby, the astigmatic waist difference Δz changes its value from 27 mm to -22 mm. In between, at $\alpha = 72.65^\circ$ the focusing of the optic is well balanced and Δz vanishes. However, the wavefront is not entirely flat due to remaining higher order aberrations.

5.2.2 Comparison between experiment and theory

In the following, the astigmatic waist difference $\Delta z(\alpha)$ is estimated theoretically by matrix methods and then compared to the experimental results.

The fundamental laser beam is assumed to be Gaussian with a local diameter of 8 mm before it is focused into the argon filled capillary (focal length 200 mm). Thus, the divergence is $\approx 8/200 = 40$ mrad and with equation (3.7) and $M^2 = 1$, the focus diameter is derived to $d_0 = 25 \mu\text{m}$. The 25th harmonic is assumed to exhibit the

same source diameter and a divergence which is 25 times smaller than that of the incident laser beam

$$d_0 = 25 \mu\text{m} \quad ; \quad \theta = 1.6 \text{ mrad.} \quad (5.5)$$

With these properties, the HHG beam matrix \mathcal{M}_0 introduced in equation (3.4) is derived at source position, where all mixed moments vanish. Now, ray transformation matrices as given in the appendix are applied to the beam matrix \mathcal{M}_0 corresponding to the experimental situation. First, \mathcal{M}_0 is propagated to the optic by $\mathcal{S}_{\text{prop}}(320 \text{ mm})$. Then, the toroidal grating $\mathcal{S}_{\text{tg}}(\alpha)$ acts on the beam and a subsequent propagation by $\mathcal{S}_{\text{prop}}(z)$ finally yields the system matrix $\mathcal{S}(z, \alpha)$ that transforms a beam \mathcal{M}_0 from source position to a distance z behind the optic (according to equation (3.8))

$$\begin{aligned} \mathcal{S}(z, \alpha) &= \mathcal{S}_{\text{prop}}(z) \cdot \mathcal{S}_{\text{tg}}(\alpha) \cdot \mathcal{S}_{\text{prop}}(320 \text{ mm}) \\ \mathcal{M}(z, \alpha) &= \mathcal{S}(z, \alpha) \cdot \mathcal{M}_0 \cdot \mathcal{S}(z, \alpha)^{\text{T}}. \end{aligned} \quad (5.6)$$

Here, the beam matrix is propagated to the detector position $z = 1320 \text{ mm}$. With $\mathcal{M}(1320 \text{ mm}, \alpha)$ the waist positions $z_{0,x}(\alpha)$ and $z_{0,y}(\alpha)$ are derived by relation (3.5) and the astigmatic waist difference $\Delta z(\alpha) = z_{0,x}(\alpha) - z_{0,y}(\alpha)$ is computed. The resulting function $\Delta z(\alpha)$ is depicted in figure 5.9 as solid blue line together with the values resulting from measured wavefronts. At specific positions, two values appear due to a repetition of the measurement.

The theoretical waist difference $\Delta z(\alpha)$ appears slightly above the experimental values. Although the relative incidence angle is adjusted very precisely, its absolute value might contain a small error. A least squares fit routine [132] results a deviation of $\Delta\alpha = -0.1^\circ$. The resulting shifted function $\Delta z(\alpha - \Delta\alpha)$ is plotted in figure 5.9 in dashed style revealing good agreement to the measurement. Now, the incidence angle for a vanishing waist difference is derived to $\alpha_0 = 72.69^\circ$. It is expected, that for this angle the photons of the beam are focused into the smallest beam area. In the following, the achievable intensity depending on the incidence angle is estimated in arbitrary units.

Following relation (3.5), from matrix $\mathcal{M}(z, \alpha)$ the local beam diameters $d_x(z, \alpha)$ and $d_y(z, \alpha)$ are derived. Approximating the beam area $A(z, \alpha) = \frac{\pi}{4} d_x(z, \alpha) d_y(z, \alpha)$ by an ellipse, the mean irradiance at position z is $I(z, \alpha) = P_0/A(z, \alpha)$ with an arbitrary beam power P_0 . Now for a specific incidence angle α , the position z_{max} is derived which yields the maximum value of $I(z, \alpha)$. This achievable

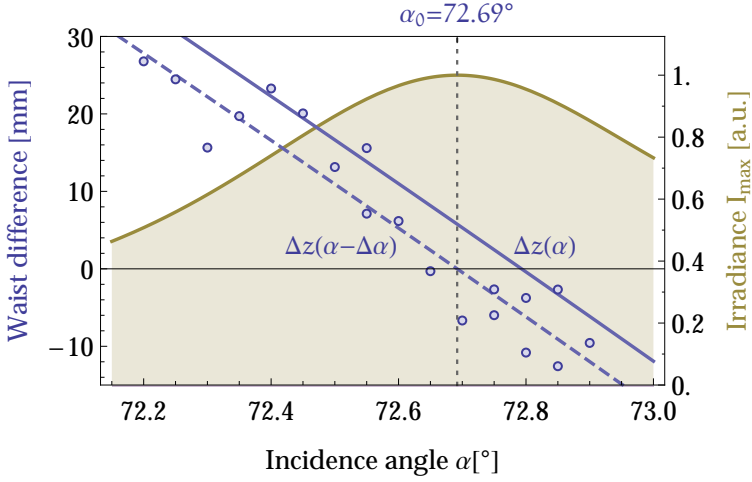


Figure 5.9: Astigmatic waist difference against incidence angle. The theoretical curve $\Delta z(\alpha)$ (solid blue line) lies slightly above the experimental values (blue dots). With a shift of $\Delta\alpha = -0.1^\circ$ best agreement is obtained (dashed blue line). The achievable irradiance $I_{\max}(\alpha)$ is depicted in yellow color.

irradiance $I_{\max}(\alpha)$ is depicted together with the astigmatic waist difference in figure 5.9 where the coordinate shift by $\Delta\alpha$ is included.

As expected, the highest photon flux is obtained for an incidence angle of $\alpha_0 = 72.69^\circ$ where the astigmatic aberration disappears. It is revealed that already a small misalignment of 0.5° reduces the achievable intensity by 50%. For CDI experiments this means that carefully aligning the toroidal grating can reduce the necessary exposure time by a factor of two. Furthermore, phase distortions of the illumination function are minimized which helps to suppress reconstruction errors for phase objects.

COHERENCE MEASUREMENTS AT THE FREE-ELECTRON LASER FLASH

A high degree of coherence is a peculiar feature of laser beams, including the EUV radiation generated at FELs. Ultra high intensities can only be achieved with coherent radiation due to constructive interference of photons. Furthermore, a fully coherent beam can be focused into the smallest possible, diffraction limited spot. Apart from that, the principle of many experiments relies on this particular property. A coherent beam strongly supports multi-photon processes [146, 147, 148] and it is the necessary condition to produce interference effects. The latter play an elementary role in coherent diffractive imaging [13], ptychography [17] and related techniques [149, 14].

Existing coherence studies pose simplifying assumptions on the FEL beam [23, 24, 25], e.g., that it can be described by the Gaussian Schell-model. Here, the four-dimensional mutual coherence function (MCF) is determined for the photon beam of FLASH without theoretical restrictions. In that approach, experimental intensity profiles of the focused FEL beam are employed to reconstruct the Wigner distribution function (WDF) which is the two-dimensional Fourier transform of the MCF.

In the following, the measurement at FLASH and the reconstruction of the Wigner distribution function are described. The obtained results are presented and compared to existing studies. The applied algorithm is critically tested by synthetic beams providing an error estimation. Furthermore, an extension of the experimental principle is proposed which is demonstrated with different TEM modes of a near IR laser.

This chapter is based on a previous publication [150] and has been revised and extended partly. All experiments at FLASH have been conducted in close collaboration with B. Keitel, E. Plönjes and M. Kuhlmann.

6.1 EXPERIMENT AT FLASH

FLASH is a single-pass free electron laser based on the SASE (self-amplification of spontaneous emission) process. It provides highly intense, short-pulsed radiation in the wavelength range $47 \dots 4.2$ nm [93, 151, 152]. Since the exponential amplification process in a SASE FEL starts from shot noise generated by the electron bunch, the photon radiation itself is of stochastic nature and individual pulses differ in their intensity, temporal structure, and spectral distribution.

The measurements have been performed at beamlines BL2 and BL3 of FLASH with the FEL operating in single pulse mode at 10 Hz repetition rate. The bunch charge of the electron beam was set to values between $0.44 \dots 0.54$ nC and the soft x-ray photon beam was generated with pulse energies in the range of $30 \dots 50$ μ J. Two circular apertures are positioned in the photon beam 18.8 m and 23.3 m behind the center of the last undulator, i.e., the expected source position (see figure 6.9). During the experiments always two apertures of equal size were used, available diameters are 10 mm, 5 mm, 3 mm and 1 mm. A general description of the FLASH user facility can be found in [94].

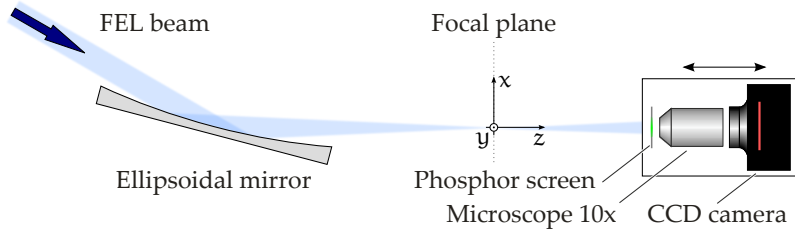


Figure 6.1: Setup for measurement of intensity profiles at FLASH in top view.

During the measurement campaign at beamline BL3, the FLASH beam was tuned to a fundamental wavelength of 24.7 nm. The beam was attenuated by two filters, a 200 nm thick, meshless Zr filter and a 198 nm thick, meshless Al filter to prevent saturation of the phosphor screen in the experimental setup, shown in figure 6.1 and described below. Thus, based on previous studies on the spectral composition of the FLASH beam [153, 93] and the theoretical filter transmissions [138], 80% of the beam energy are attributed to the fundamental wavelength, 18% to the third harmonic and 2% to the fifth harmonic. Since the fundamental dominates for this attenuation scheme, the beam is treated as monochromatic at $\lambda = 24.7$ nm. During the measurements at BL2 ($\lambda = 25.8$ nm) a 101 nm thick Al

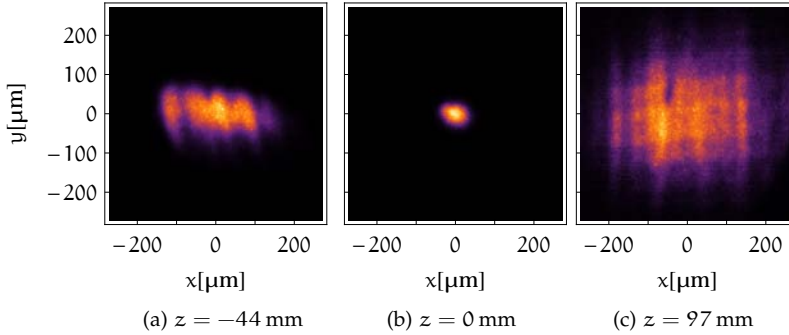


Figure 6.2: Intensity profiles of the photon beam at FLASH at a wavelength of 24.7 nm, captured at BL3.

filter together with a 420 nm thick Si filter were used, both self-supporting. This filter combination leads to a strong suppression of the harmonics and nearly 100% of the transmitted beam energy is concentrated in the fundamental wavelength.

The experimental setup is shown schematically in figure 6.1. The entire EUV beam path from undulator to the depicted screen is kept under ultra high vacuum condition. At both beamlines BL2 and BL3, the incoming FEL beam is focused by the ellipsoidal beamline mirror producing a focal spot 2 m behind the center of the mirror [94]. The body of these mirrors consists of Zerodur and the optical surface is coated by a 45 nm thick carbon layer. The specifications from the manufacturer (Zeiss) are: semi axes $X = Y = 624 \pm 30$ mm and $Z = 36500 \pm 100$ mm, surface roughness < 0.5 nm (rms), tangential slope error < 0.3 arcsec (rms) and sagittal slope error < 1.0 arcsec (rms). A phosphorous screen (thickness 4 μm , grain size 1 μm), which is movable under vacuum, intercepts the beam at various positions along the caustic. Thus, the beam profiles are converted into visible wavelengths. The screen is imaged by a $10\times$ magnifying objective to a CCD camera with 1280×1024 pixels, each 6.45 μm in size and with a dynamic range of 12 bit (Lumenera Lm165M). Since single pulse exposures lead to saturation effects of the phosphor screen the exposure time is 1500... 1800 ms comprising between 15 and 18 pulses depending on the attenuation scheme for the corresponding measurement. A motorized translation stage allows for an automated movement of the detector in beam direction which covers a range of up to ± 11 Rayleigh lengths around the beam waist, corresponding to 250 mm. An entire measurement involves 145 different positions z_i being distributed as

$$z_i = z_R \tan \phi_i$$

with the mean Rayleigh length z_R and equidistant angles ϕ_i . This represents tight sampling close to beam waist becoming coarser further out. For the reconstruction of the Wigner distribution this results in a uniform mapping of the phase space.

6.2 RECONSTRUCTION OF THE WIGNER DISTRIBUTION FUNCTION

Based on the relations of section 3.4.3, the reconstruction of the 2D Wigner distribution function $h_x(x, u)$ is discussed under the assumption of a separable beam since this procedure can be illustrated in a descriptive fashion. Equivalent steps are taken for non-separable beams, but in a 4D phase space. In the following these two methods are also denoted as *2D-evaluation* and *4D-evaluation*.

At the beginning, the intensity distributions $I(x, y)|_z$ are processed in terms of a background correction. A dark image is subtracted and an additional offset of a few counts eliminates the remaining noise signal. A selection from the 145 background corrected beam profiles is shown in figure 6.2. Corresponding to the caustic evaluation in section 5.1.2, waist position z_0 and Rayleigh length z_R are derived in terms of mean values for x - and y -direction, i.e., $z_0 = 1/2 \cdot (z_{0,x} + z_{0,y})$. In the following, the position z_0 is chosen as the origin of the z -axis.

6.2.1 2D-evaluation for separable beams

The reconstruction procedure is illustrated in figure 6.3 in terms of the following steps:

- (a) Each intensity profile is transformed into a 1D distribution by the integration

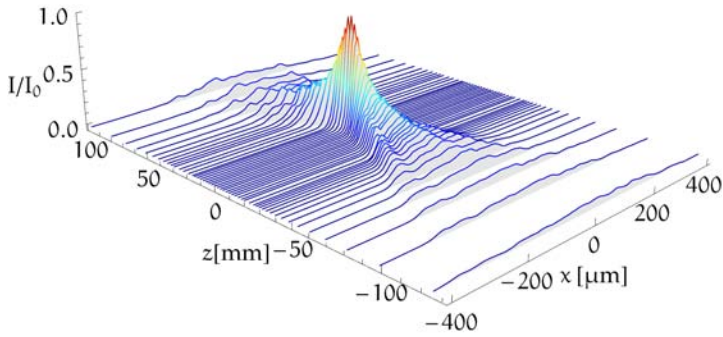
$$I_x(x)|_z = \int I(x, y)|_z dy.$$

- (b) A Fourier transform is applied to the individual 1D intensity profiles

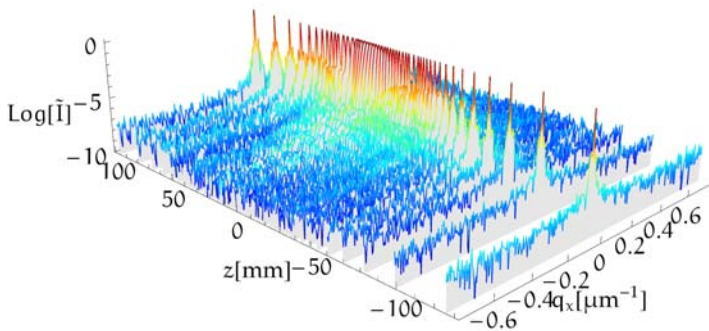
$$\tilde{I}_x(q_x)|_z = \mathcal{F}[I_x(x)]_z.$$

- (c) The projection slice theorem for free beam propagation (see section 3.4.3)

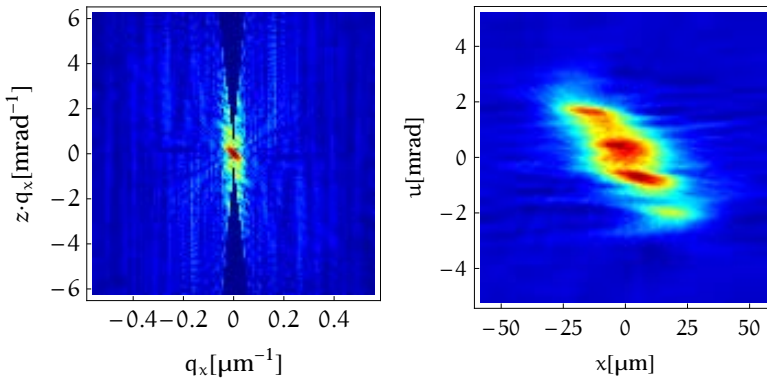
$$\tilde{h}_x(q_x, z \cdot q_x) = \tilde{I}_x(q_x)|_z$$



(a) 1D intensity profiles $I_x(x)|_z = \int I(x, y)|_z dy$ at positions z .



(b) Fourier transformed intensity profiles $\tilde{I}_x(q_x)|_z$ shown in logarithmic scaling.



(c) WDF in reciprocal space $\tilde{h}_x(q_x, z \cdot q_x)$ after mapping, shown in logarithmic scaling.

(d) A Fourier back-transformation results the WDF $h_x(x, u)$ in real space.

Figure 6.3: Reconstruction of the Wigner distribution function for separable beams. For better visibility, some intensity profiles close to focal position are omitted. In the reciprocal Wigner space depicted in (c), individual lines with slope z represent the Fourier transformed intensity profiles.

is employed to map the resulting data sets $\tilde{I}_x|_z$ into the reciprocal phase space of the WDF. A two-dimensional regular grid is generated that contains 129^2 cells. Now, the values of each distribution $\tilde{I}_x|_z$ are assigned to corresponding lines in \tilde{h}_x with the slope z . The arithmetic average is applied to cells, where more than one value is allocated. In order to achieve a uniform distribution, the z -values are rescaled by the mean Rayleigh length z_R [109]. The corresponding program code which was developed for Wolfram Mathematica is given in chapter A.2.

- (d) A 2D Fourier back-transformation of the obtained matrix

$$h_x(x, u) = \mathcal{F}^{-1} [\tilde{h}_x(q_x, j_u)]$$

finally results the WDF in real space. The edge length of a cell in spatial direction is given by the effective pixel size of the detector Δx . The width of a cell in angular direction is derived by $\Delta u = \Delta x / z_R$.

6.2.2 4D-evaluation for non-separable beams

In case of a non-separable beam, basically the same actions are performed as described above, but in a higher dimensional space. The same data set of 2D intensity profiles is employed, but here, they are not converted into 1D distributions. The phase space is four-dimensional and is constituted by a regular grid of 129^4 cells. Considering a beam propagating through free space again, the Fourier transformed 2D intensity profiles represent planes with the slope z in the reciprocal 4D Wigner space. Particularly, the following steps lead to the reconstruction of the Wigner distribution:

- (a) A Fourier transform is applied to the individual 2D intensity profiles

$$\tilde{I}(\vec{q})|_z = \mathcal{F} [I(\vec{x})]_z.$$

- (b) The projection slice theorem for free beam propagation (see section 3.4.3)

$$\tilde{h}(\vec{q}, z \cdot \vec{q}) = \tilde{I}(\vec{q})|_z$$

is employed to map the resulting data sets $\tilde{I}|_z$ into the reciprocal phase space of the WDF. The corresponding program code is given in chapter A.2.

- (c) A 4D Fourier back-transformation of the obtained matrix

$$h(\vec{x}, \vec{u}) = \mathcal{F}^{-1} [\tilde{h}(\vec{q}, \vec{j})]$$

finally results the WDF in real space.

It should be noted that the present optical system serves to scan a three-dimensional volume of the radiation field only. Thus, gaps will remain in the 4D phase space after the mapping, possibly introducing an error in the reconstruction. This issue can be addressed by an interpolation of the empty cells, assigning the mean value of those adjacent entries which are non-zero. However, still certain beam properties like the twist parameter [154] can not be recovered. Thus, a more sophisticated optical system needs to be designed providing access to the entire 4D phase space of the beam. A possible solution is presented in section 6.5.

6.3 RESULTS

Here, the experimental results are presented for the FLASH beam, first, under typical beamline settings. The 4D Wigner distribution function is reconstructed for a non-separable beam and additionally, under the assumption of separability. First, the discussion is focused on the beam propagation and the difference between both evaluation methods. Then, the coherence properties are presented in comparison with existing studies that employ Young's double pinhole [23]. Furthermore, it is demonstrated how the coherence of the FEL beam is improved by smaller apertures.

6.3.1 *Propagation properties of the FLASH beam*

The following discussion is based on measurements at BL3, at a wavelength of 24.7 nm with the largest apertures of 10 mm diameter, which practically not influence the FEL beam. The position of these apertures is indicated in figure 6.9. A selection of the obtained beam profiles is shown in figure 6.2. While close to focal position the intensity appears uniformly distributed, a horizontal modulation develops for increasing distances. It is assumed that this can be attributed to a slight corrugation of the surface of the ellipsoidal beamline mirror which is currently under investigation [155]. Thus, due to the orientation of the long axis, especially the horizontal propagation characteristics are affected.

The 4D Wigner distribution function of the investigated FEL beam is represented by the projections $h_x(x, u)$ and $h_y(y, v)$ in figure 6.4. This way, the beam propagation is visualized separately for horizontal and vertical direction. A comparison of this derived projection with the 2D Wigner distribution for separable beams reveals complete conformity (compare with figure 6.3).

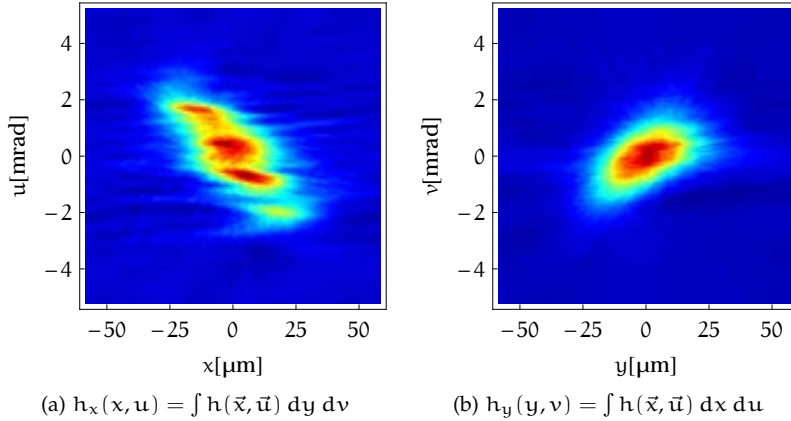


Figure 6.4: Wigner distribution function of the FLASH beam at a wavelength of 24.7 nm, captured at BL3. The figure shows projections of the 4D distribution.

Apparently, while $h_x(x, u)$ is distributed smoothly in spatial direction x , it shows a stripe structure in angular direction u . This feature resembles the uniform near-field profile and the developing horizontal modulation when approaching the far-field. In contrast, $h_y(y, v)$ is distributed rather Gaussian like for both axes y and v corresponding to the vertical properties of near- and far-field. Qualitatively, an astigmatic aberration can already be identified due to different inclinations of the distributions h_x and h_y . While horizontally, the beam appears convergent, in vertical direction it is divergent and thus, both foci do not coincide.

h is real, since the value of $P = \int h(\vec{x}, \vec{u}) d^2x d^2u$ reveals a real part on the order of 1 and an imaginary part on the order of 10^{-18} . Hence, the derived mutual coherence function follows hermitian symmetry [108].

Table 6.1: Beam propagation parameters of FLASH as resulting from the WDF ($\lambda = 24.7$ nm). The results under assumption of a separable beam are compared to those for a non-separable beam.

Evaluation method	Waist diameter	Divergence	Beam quality factor
	$d_{0,x} / d_{0,y}$ [μm]	θ_x / θ_y [mrad]	M_x^2 / M_y^2
Separable	50 / 40	5.1 / 3.7	8.1 / 4.8
Non-separable	52 / 41	5.2 / 3.6	8.6 / 4.6

From the 4D Wigner distribution, the 4×4 beam matrix \mathcal{M} is derived by computing the second order moments. In a next step, the positions of the foci is derived to $z_{0,x} = 8.9$ mm and $z_{0,y} = -8.9$ mm. Thus, the astigmatic aberration can be quantified in terms of the waist difference $\Delta z = 17.8$ mm which is equivalent to $1.7 z_R$, where z_R is the mean Rayleigh length. The remaining beam propagation parameters resulting from \mathcal{M} are summarized in table 6.1 together with the values that result under assumption of a separable beam. At first sight, a comparison between both evaluation methods implies that the beam can be regarded as separable. However, the presented parameters are essentially the same since they do not depend on the mixed moments such as $\langle xy \rangle$ or $\langle yu \rangle$. In fact, the Wigner distributions derived for separable and non-separable beam differ from each other which will become clear in the following.

In order to verify the computed Wigner distribution, it is propagated to different z -positions by relation (3.40) and then the local near-field is reconstructed by equation (3.30). A comparison between the resulting intensity distributions with the experimental data reveals to what extent the WDF is consistent with the real beam properties. This validation is conducted for both evaluation methods, for separable and non-separable beams. The results are found in figure 6.5, where all reconstructions are constituted by 129×129 pixels and the measured distributions have higher resolutions.

Obviously, the assumption of a separable beam allows a reproduction of intensity profiles, but in a simplified fashion. In contrast, the algorithm that assumes non-separability nicely restores also small features, although the resolution is significantly lower compared to the experimental data. In more detail, this can be seen in figure 6.6, where horizontal sections of the profile at $z = -44$ mm are depicted. While at position $y = -7 \mu\text{m}$ both reconstructions agree well to the measured distribution, in greater distances the 2D reconstruction results in significant deviations.

The presented comparison between both evaluation methods reveals that the FLASH beam has to be treated as non-separable in order to describe it properly. However, in the following section the coherence properties are studied also under assumption of a separable beam, revealing to what extent both methods differ.

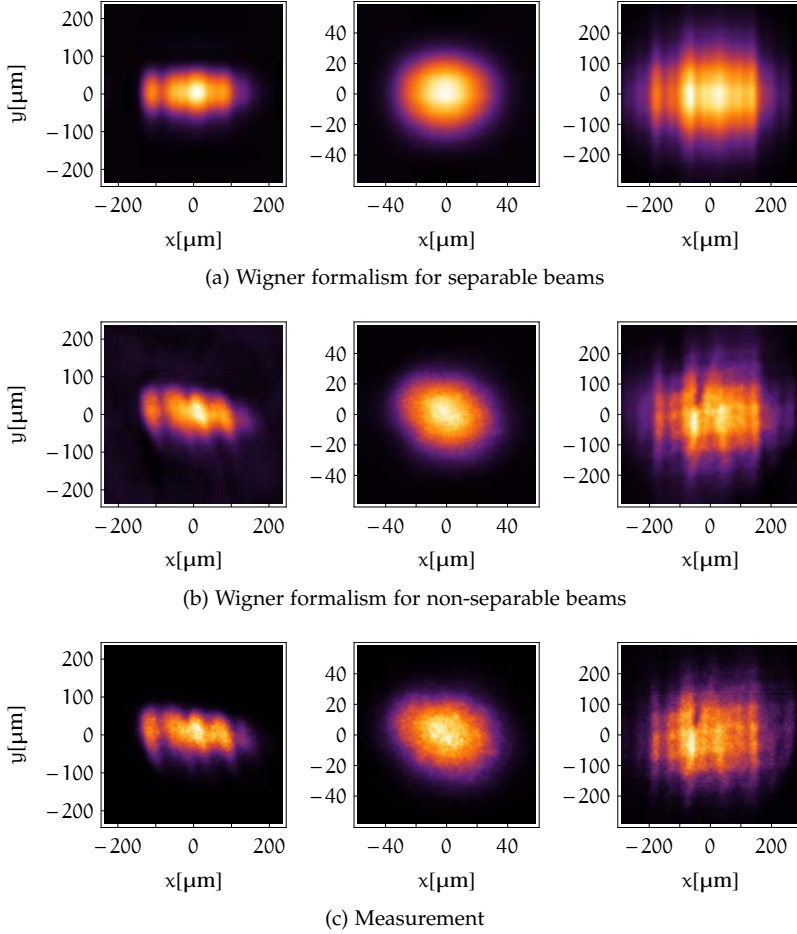


Figure 6.5: Reconstruction of intensity profiles from the WDF (a), (b) in comparison with measured data (c) at z -positions -44 mm, 0 mm and 97 mm (from left to right). Apparently, only the formalism for non-separable beams results in a satisfying reproduction of the FLASH beam.

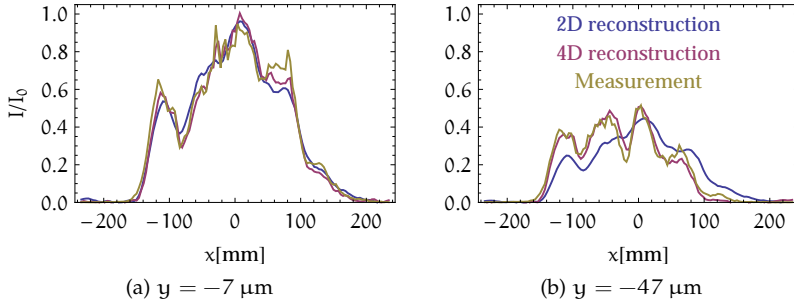


Figure 6.6: Horizontal sections $I(x)$ of the intensity profile at $z = -44$ mm resulting from the reconstruction for separable and non-separable beam together with measured data.

6.3.2 Coherence properties of the FLASH beam

The mutual coherence function results from a 2D Fourier transformation of the WDF (see equation (3.29)) and is given in terms of sections $|\Gamma_x(x, s_x)|$ and $|\Gamma_y(y, s_y)|$ in figure 6.7. While for $s_x = 0$ and $s_y = 0$ these distributions represent the intensity $I(x, 0)$ and $I(0, y)$ at mean waist position, for increasing s_x and s_y the decay of the coherence is revealed. Equation (3.21) is employed to quantify the coherence lengths l_x and l_y which are summarized in table 6.2 based on the 2D- and the 4D-evaluation. Since especially, the relation between these values and the beam size is relevant, the local beam diameters d_x and d_y are listed in table 6.2, too. In figure 6.10, the central coherent part of the FLASH beam is indicated by the black ellipse whereas the white ellipse confines the intensity distribution. The computed values indicate that the coherent fraction of the beam amounts to $l_x/d_x = 0.13$ and $l_y/d_y = 0.22$ in horizontal and vertical direction, respectively.

One-dimensional sections $|\gamma_x(s_x)|$ and $|\gamma_y(s_y)|$ represent the local degree of coherence in figure 6.8. The standard deviation of these distributions is derived by Gaussian fit functions as indicated in the figure by solid curves.

Finally, employing equation (3.33) the global degree of coherence is computed for a separable and a non-separable beam. All mentioned coherence parameters of the FLASH beam are summarized in table 6.2, as resulting from 2D- and 4D-Wigner evaluation and from Young's experiment by Singer *et al.* [23].

Comparing both Wigner methods, apparently, the assumption of a separable beam results in smaller coherence parameters while the local beam diameter is rather the same. Thus, this simplification

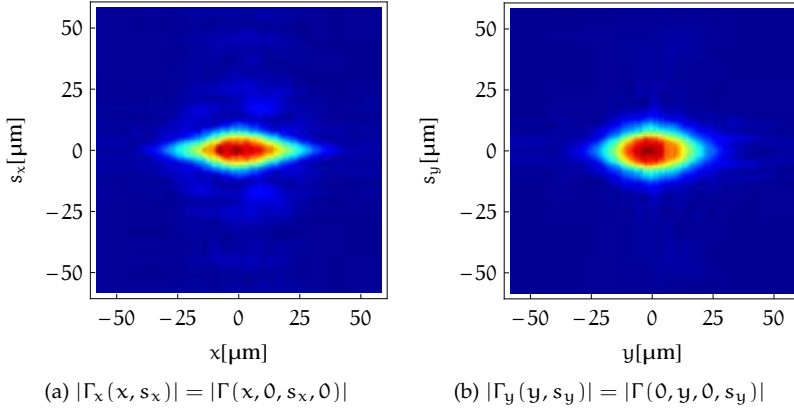


Figure 6.7: Mutual coherence function of the FLASH beam at a wavelength of 24.7 nm, captured at BL3. The figure shows sections in terms of absolute values resulting for a non-separable beam.

results in an underestimation of the global degree of coherence K by approximately 60%. As demonstrated in the precedent section, the FLASH beam should be treated as non-separable in order to resemble all propagation features in an adequate fashion. Hence, for further discussions, only those parameters are used that are derived by the 4D-evaluation.

Considering the results from the 4D-WDF with respect to the double pinhole experiment, coherence length l and standard deviation σ_γ reveal similar values. Contrarily, the local beam diameter that is evaluated by Singer *et al.* through PMMA imprints is significantly lower than the value resulting from the Wigner evaluation. At the three times shorter wavelength of 8.0 nm for Young's experiment compared to 24.7 nm in the present case, a significantly smaller beam diameter is to be expected.

However, the multi pulse exposure in the Wigner experiment might lead to an overestimation due to a pointing instability. On the other hand, the evaluation of PMMA imprints can also result in underestimated beam sizes [145]. In any case, the global degree of coherence is strongly dependent on the derived beam diameter, as relations (3.27) and (3.36) reveal. As a consequence, the value $K = 0.032$ derived from the 4D Wigner distribution is one order of magnitude lower than the result $K = 0.42 \pm 0.09$ from Singer *et al.*.

The difference between the results for the global degree of coherence is surprisingly large. One possible reason for that discrepancy might be that the coherence properties have changed between

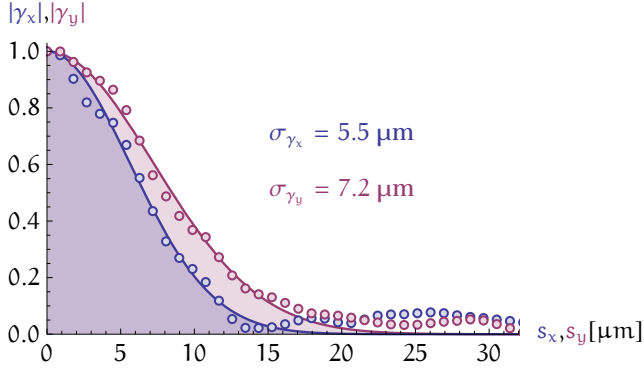


Figure 6.8: Local degree of coherence at mean waist position of the FEL beam given in terms of the sections $|\gamma_x(s_x)| = |\gamma(0, 0, s_x, 0)|$ and $|\gamma_y(s_y)| = |\gamma(0, 0, 0, s_y)|$. The standard deviations σ_{γ_x} and σ_{γ_y} result from the depicted Gaussian fit functions. Evaluated for a non-separable beam.

both experiments. Note, that the wavelength during Young's experiment (8.0 nm) has been significantly lower than during the Wigner measurements (24.7 nm). Possibly, this has an effect on the global degree of coherence.

Besides, it should be clarified that the applied Wigner formalism characterizes a large ensemble of individual pulses. Thus, pulse-to-

Table 6.2: Coherence parameters of FLASH at mean waist position in comparison between Wigner formalism and Young's double pinhole experiment [23] (Young's experiment: $\lambda = 8.0$ nm, Wigner formalism: $\lambda = 24.7$ nm, in both cases 10 mm diameter apertures are employed).

	2D-Wigner	4D-Wigner	Young's experiment
Loc. beam diameter d_x / d_y [μm]	63 / 54	67 / 53	17 / 17
Coherence length l_x / l_y [μm]	7.5 / 9.7	9.0 / 11.6	10.0 / 12.2
Standard deviation $\sigma_{\gamma_x} / \sigma_{\gamma_y}$ [μm]	4.0 / 5.1	5.5 / 7.2	6.2 / 8.7
Degree of coherence K	0.020	0.032	0.42

pulse fluctuations in the coherence properties, as expected due to the statistical SASE process, are averaged to *mean* values.

In contrast, during Young's experiment individual pulses are analyzed and many different values for the local degree of coherence have been found. These fluctuations could be due to a pointing instability but could also well be attributed to inherent coherence fluctuations. However, in the Singer experiment only the most coherent pulses have been employed for evaluation which results in the *best* coherence properties that can be expected for the FLASH beam.

In section 6.4, an estimation is provided for these beam instabilities and the resulting error in the Wigner evaluation.

6.3.3 Influence of apertures

In this section, the coherence properties of the FLASH beam should be improved by application of circular apertures and thus by a confinement of the beam divergence. The position of these apertures is shown in figure 6.9. As routinely used by FLASH users, diameters from 10 mm down to 1 mm are employed. The effect on the beam properties is studied by the derivation of the non-separable Wigner distribution function at mean waist position.

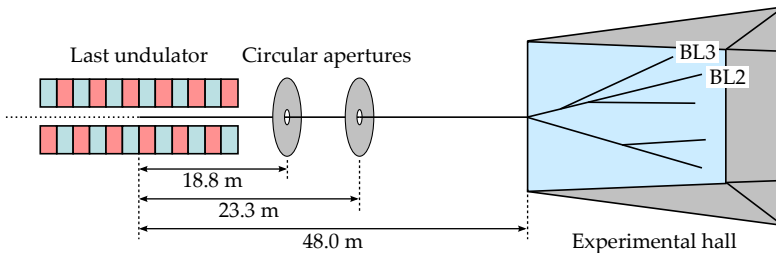


Figure 6.9: Sktech of the beam line at FLASH with the position of the circular apertures. In all experiments, two apertures of equal size are employed. The available diameters are 10 mm, 5 mm, 3 mm and 1 mm.

The results are summarized in table 6.3. As can be expected [156], employing smaller apertures leads to improved coherence properties. Mainly, this is due to a reduction of the beam's divergence θ . Therefore, the Wigner distribution occupies less phase space in angular direction and, as a consequence of the well-known Fourier relations, the extent of the mutual coherence function scales up in *s*-direction, i.e., the coherence length l grows. Since therefore, the fraction l/d increases, also the global degree of coherence is raised.

As the measurements at BL₃ reveal, the waist diameter stays more or less constant when applying smaller apertures. Thus, only the divergence is influenced while the source properties of FLASH stay unaffected.

Table 6.3: Coherence parameters of FLASH for various sizes of apertures. The values result from measurement campaigns at beamlines BL₃ and BL₂ and the corresponding Wigner analysis for non-separable beams. Note the difference between the local beam diameter d_x , given at mean waist position and the waist diameter $d_{0,x}$, which deviate from each other due to the astigmatic aberration.

Aperture	10 mm	5 mm	3 mm	1 mm
Beamline	3	3	3	2
λ [nm]	24.7	24.7	24.7	25.8
$d_{0,x} / d_{0,y}$ [μm]	52 / 41	48 / 42	51 / 43	38 / 34
d_x / d_y [μm]	67 / 53	65 / 52	60 / 48	42 / 38
θ_u / θ_v [mrad]	5.2 / 3.6	5.1 / 3.3	3.8 / 2.8	2.5 / 2.3
l_x / l_y [μm]	9.0 / 11.6	9.1 / 11.7	10.2 / 12.6	15.3 / 18.3
K	0.032	0.034	0.056	0.198

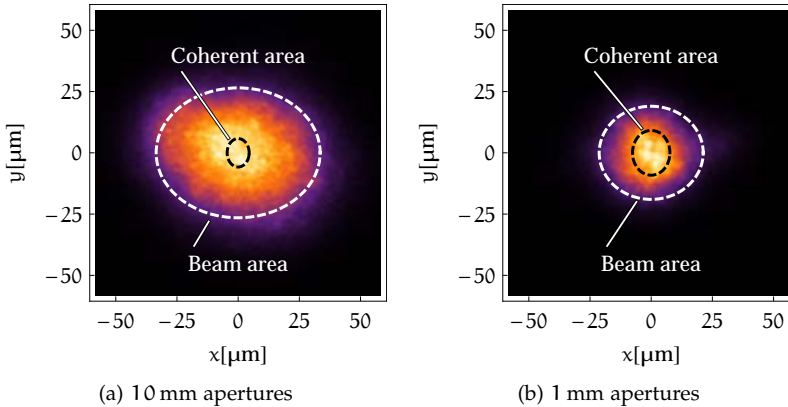


Figure 6.10: Coherent fraction of the FEL beam at mean waist position, based on the 4D Wigner evaluation. Smaller apertures increase the coherent area whereas the beam size decreases.

For the smallest aperture with a diameter of 1 mm, the coherence lengths are increased by a factor of ≈ 1.6 . In this case, also the waist diameters have decreased to $\approx 78\%$ of its previous value, what can be attributed to the situation at a different beamline (BL2): although the FEL operating parameters were reproduced nearly as before, the beam properties might slightly differ since the beamline optic was not the same. As a benefit from both, a reduction of beam divergence and local beam diameter, the global degree of coherence is increased by a factor of 6 to a value of $K = 0.198$.

An illustration of the discussed beneficial effect is shown in figure 6.10 where beam area and coherent area are indicated by ellipses. These results are especially relevant for experiments that require certain coherence properties. For instance, in order to achieve successful CDI results, the coherence length should be at least twice as large as the extent of the sample [20]. Thus, in a certain range, the FLASH beam can be optimized to fulfill the experimental needs by an appropriate aperture.

6.4 ERROR ESTIMATIONS

As previously mentioned, the investigated FEL beam poses two issues in the context of the applied Wigner algorithm: beam fluctuations and non-separability. In the following, both effects are investigated and corresponding errors are estimated for the derived beam parameters.

6.4.1 *Beam fluctuations*

In a previous section, the global degree of coherence K has been derived from the WDF. Surprisingly, the computed value is one order of magnitude lower compared to the result from Young's experiment. One possible reason for this discrepancy lies in beam fluctuations due to the statistical SASE process. It can be observed that both, beam position and beam diameter vary from pulse to pulse.

Since single FEL pulses saturate the employed phosphor screen, an accumulation of > 15 attenuated pulses is required to achieve a linear response. In connection with a beam instability, this averaging results in broadened waist diameter and divergence angle. As a consequence, the Wigner distribution occupies a larger phase space and the coherence K becomes underestimated.

Here, single pulse exposures are investigated in order to quantify the pointing stability of the FLASH beam and the associated error in K . In fact, these measurements were conducted in the

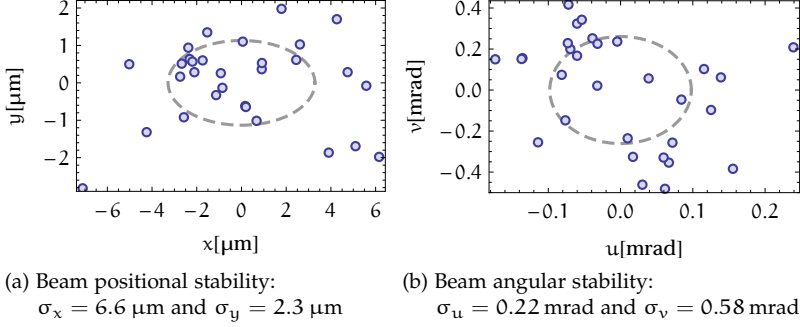


Figure 6.11: Pointing stability of the FLASH beam. The diameters of the ellipses correspond to positional stability σ_x , σ_y and angular stability σ_u , σ_v .

non-linear regime of the phosphor screen. However, for the following estimations this effect plays a minor role and can be neglected. The experiment was carried out at BL2 at a photon wavelength of 13.5 nm with 10 mm apertures. A series of 30 single pulses is obtained for both, the near-field at $z = 0$ and the far-field which is approached by $z = 114 \text{ mm} = 11.6 z_R$. For all intensity profiles, the beam position and beam diameter is evaluated by the second order moments method [157]. The results for the far-field are converted into angular information through a division by the distance z . In the following, first the pointing stability is characterized and then the fluctuation of the beam diameter is evaluated.

The pointing stability of the FLASH beam is visualized in figure 6.11 in terms of point clouds that comprise the individual beam centroids for near- and far-field. From these data sets, the beam positional stability σ_x , σ_y and beam angular stability σ_u , σ_v is derived by computing the standard deviation [158]. Ellipses with corresponding diameters illustrate these values.

It is assumed, that the fluctuations observed at BL2 are similar to those at BL3, where most of the coherence measurements were conducted. Now, in order to correct the previously obtained beam diameters $d_{0,x}$, $d_{0,y}$ and divergences θ_x , θ_y from the broadening due to the pointing stability, the values of σ_x , σ_y , σ_u and σ_v are subtracted. This way, the overrated phase space volume is rectified.

Now the global degree of coherence is derived by

$$K = \frac{16\lambda^2}{\pi^2} \cdot \frac{1}{d_{0,x} d_{0,y} \theta_x \theta_y} \quad (6.1)$$

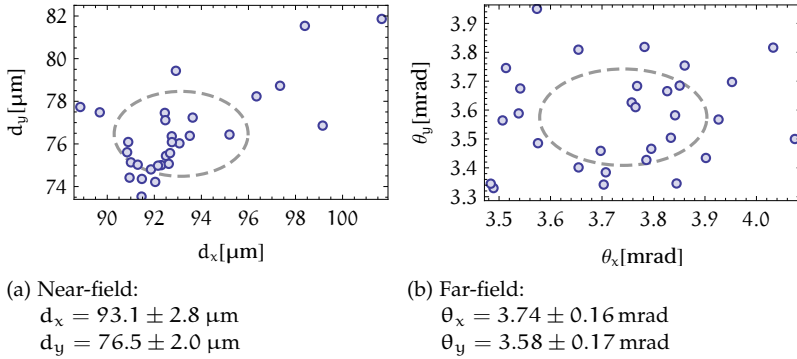


Figure 6.12: Fluctuations of beam diameter and divergence. The half-axes of the ellipse correspond to the standard deviations of the data sets.

with both, the corrected beam propagation parameters and the uncorrected. It turns out, that taking the pointing stability into account results in a 1.5 times larger value for K . This is a rather moderate effect, only partly causing the observed difference between the results from Wigner and double pinhole experiment.

The variation of the beam diameters d_x , d_y and divergences θ_x , θ_y are illustrated in figure 6.12 together with the corresponding averages and standard deviations. The observed fluctuations are rather low and amount to $\approx 3\%$ and $\approx 5\%$ of the mean values in the near-field and far-field, respectively.

Applying the Gaussian law of error propagation to equation (6.1), a standard deviation ΔK can be estimated for the global degree of coherence employing the relative uncertainties $\frac{\Delta d_x}{d_x}$, $\frac{\Delta d_y}{d_y}$, \dots

$$\begin{aligned} \Delta K &= \sqrt{\left(\frac{\Delta d_x}{d_x}\right)^2 + \left(\frac{\Delta d_y}{d_y}\right)^2 + \left(\frac{\Delta \theta_x}{\theta_x}\right)^2 + \left(\frac{\Delta \theta_y}{\theta_y}\right)^2} \cdot K \\ &= 0.08 \cdot K. \end{aligned} \quad (6.2)$$

From these rough estimations the following facts can be concluded:

- The pointing variations lead to an underestimation of the coherence K , the real value is 50% larger.
- Beam fluctuations allow the determination of K within an uncertainty level of 8%.

Thus, based on the 4D Wigner evaluation, the global degree of coherence for the FLASH beam can now be specified by

$$K = 0.048 \pm 0.004 \quad (6.3)$$

for a wavelength of 24.7 nm and apertures of 10 mm diameter. Apparently, these estimations do not explain the large difference in K with respect to Young's experiment (see table 6.2). Consequently, pointing instability and coherence fluctuations can not be the main reason for this discrepancy. As already mentioned in section 6.3.2, an explanation for the remaining difference could be that beam diameters are evaluated differently (Young - PMMA imprints \leftrightarrow Wigner - phosphor screen). Furthermore, the double pinhole experiment has been conducted at a significantly lower wavelength (8.0 nm) as compared to the measurement of the Wigner distribution (24.7 nm). Thus, the coherence might have been lower in the latter case.

6.4.2 Coverage of phase space

The presented results reveal that the FLASH beam is non-separable and hence, the corresponding 4D Wigner formalism needs to be applied. In that case, a four-dimensional distribution is reconstructed from a three-dimensional intensity measurement. Thus, gaps will remain in the reciprocal phase space leading to a computed Wigner distribution which possibly deviates from the true Wigner distribution. This issue is addressed by the interpolation procedure described in section 6.2 but cannot entirely be eliminated. Therefore, the error of the derived beam properties due to the incomplete data set should be classified.

For that purpose, a set of intensity profiles of a Gaussian Schell-model beam is generated to benchmark the applied procedures. Here, the same wavelength, waist positions, waist diameters and divergences are used as present during the measurements at FLASH. It can be expected that this simulated beam occupies a comparable phase space as the FEL beam, and that the gaps remaining after the mapping procedure are similar. The accuracy of the algorithm is then estimated by a comparison between the computed coherence parameters and their theoretical values.

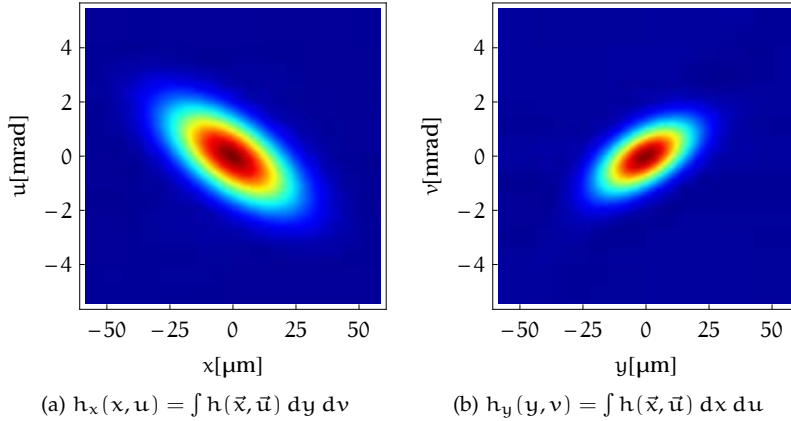


Figure 6.13: Wigner distribution function of a Gaussian Schell-model beam, simulated with beam parameters as found for the FLASH beam. The figure shows projections of the 4D distribution.

The intensity distribution of a Gaussian Schell-model beam is given by [107]

$$I(x, y, z) = \frac{I_0}{d_x(z) d_y(z) / (d_{0,x} d_{0,y})} \cdot \exp \left[\frac{-8 x^2}{d_x(z)^2} + \frac{-8 y^2}{d_y(z)^2} \right] \quad (6.4)$$

with the local beam diameter $d_x(z)$, as given in equation (3.9). $I(x, y, z)$ is evaluated with the same discretization and at the same positions as during the experiment at FLASH, resulting in 145 intensity profiles with a pixel size of $0.645 \mu\text{m}$. From the design parameters λ , $d_{0,x}$ and θ_u , the global degree of coherence is derived by $K = K_x \cdot K_y$ with $K_x = \frac{4}{\pi} \cdot \frac{\lambda}{d_{0,x} \theta_u}$ and the coherence length by $l_x = K_x \cdot d_x$ [107]. An overview of these values is given in table 6.4.

The computed Wigner distribution function of the Gaussian Schell-model beam is depicted in terms of projections in figure 6.13. It has been derived from the simulated intensity profiles with the 4D formalism, i.e., without the assumption of a separable beam. Apparently, the reconstruction does not show any artifacts. This is still the case when a noise level is included, which is comparable to the experimental data. Thus, the structures in the corresponding distribution derived for the FLASH beam shown in figure 6.4 are very likely not due to numerical errors and can be attributed to physical properties.

In Table 6.4 all beam parameters derived for the Gaussian Schell-model beam are summarized. It is revealed that from the Wigner

Table 6.4: Beam parameters of a synthetic Gaussian Schell-model beam, derived by the four-dimensional Wigner formalism. Design parameters are chosen corresponding to previous results for the FLASH beam as summarized in table 6.1.

	Design parameters	Wigner evaluation
$d_{0,x} / d_{0,y}$ [μm]	52 / 41	52 / 42
θ_u / θ_v [mrad]	5.2 / 3.6	4.7 / 3.0
M_x^2 / M_y^2	8.6 / 4.6	7.7 / 4.0
l_x / l_y [μm]	8.1 / 11.1	8.1 / 11.0
K	0.025	0.030

distribution function all predefined beam parameters can be recovered with acceptably small deviations. For instance, the procedure results in a global degree of coherence of 0.030 which is 20% above the theoretical value of 0.025. All other beam parameters are reproduced with better accuracy.

6.5 4D MEASUREMENT

The measurements at FLASH have unveiled non-separability of the investigated FEL beam which involves the need to scan its entire 4D phase space. However, the employed optical system suffices to access a 3D sub-manifold only. This issue can be overcome by a suitable extension of the experimental setup offering one further degree of freedom. In the following, a possible realization is proposed that includes a rotatable toroidal mirror. The system is tested employing a near IR laser with an adjustable resonator. Several TEM modes are investigated and the derived Wigner distributions are compared to theoretical predictions.

6.5.1 Experimental setup

In the visible range, a complete mapping of the 4D phase space of non-separable beams can be achieved by a combination of a spherical and a rotatable cylindrical lens [159]. Here, the experiment should be applicable especially to wavelengths in the EUV range, where no transmissive lenses are available. A convenient alternative is given by a toroidal mirror, acting as the only optical element. Figure 6.14 shows a possible arrangement, where the mirror reflects a laser beam under a small incidence angle. The subsequent beam propagation is captured in terms of intensity profiles by a movable CCD camera. Now, an additional degree of freedom is provided by a rotation of the toroidal mirror about its normal axis.

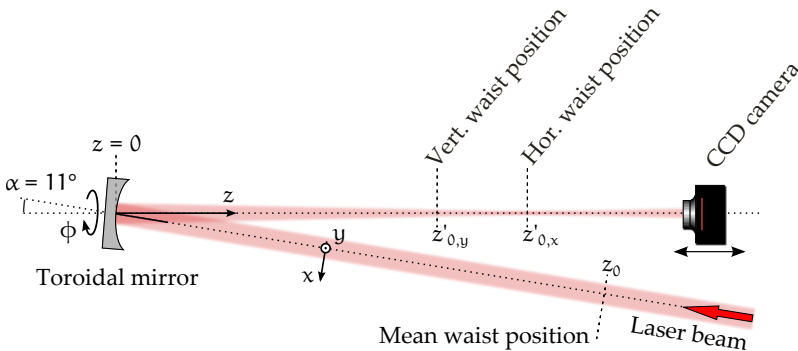


Figure 6.14: Setup for a 4D measurement of the Wigner distribution. A distinction is made between the *beam system* with $z < 0$ and the *camera system* with $z > 0$, whereas propagation parameters in the camera system are denoted by a '.

Here, the proposed arrangement is used to capture the WDF of a near IR beam provided by a diode pumped Nd:YVO₄ laser at the fundamental wavelength of $\lambda = 1064$ nm. With an adjustable hemispherical resonator, different TEM modes and their superpositions can be generated. The employed toroidal mirror is made of an aluminum alloy with the radii $R_1 = 300$ mm and $R_2 = 200$ mm at a surface roughness ≤ 12 nm and shape accuracy ≤ 1 μ m (as specified by the manufacturer LT Ultra). A motorized stage allows rotation within the range $\phi = -\pi \dots \pi$ about its symmetry axis. The CCD camera offers 1280×1024 pixels on a 2/3" chip with a dynamic range of 12 bit (Lumenera Lw160M). It is movable within distances of $z = 70$ mm \dots 200 mm to the mirror. In order to approach isotropic mapping in reciprocal phase space, two sets of z -positions are employed, distributed as

$$\begin{aligned} z_{x,i} &= \frac{z_R \tan \varphi_i - z_0}{1 - 2/R_1(z_R \tan \varphi_i - z_0)} \\ z_{y,i} &= \frac{z_R \tan \varphi_i - z_0}{1 - 2/R_2(z_R \tan \varphi_i - z_0)} \end{aligned} \quad (6.5)$$

with the mean Rayleigh length z_R in the beam system and equidistant angles φ_i . These relations result from $\tan \varphi = \mathcal{B}/\mathcal{A}$, where \mathcal{A} , \mathcal{B} are sub-matrices of the system matrix \mathcal{S} which is derived in the following discussion. φ is the angle of a target plane defined by the general mapping equation (3.42). Here, the reflection angle at the mirror has been approximated by $\alpha = 0$.

Practically, the z -positions (6.5) represent tight sampling of the beam waists behind the toroid, becoming coarser apart. During the experiment, 1000 intensity profiles are captured at 100 different z -positions with 10 equidistant rotation angles of the mirror.

6.5.2 Data evaluation

In order to retrieve the WDF from experimental data, the system needs to be described by an $\mathcal{A}\mathcal{B}\mathcal{C}\mathcal{D}$ -matrix. This is realized by

$$\begin{aligned} \mathcal{S}(\phi, z) &= \mathcal{S}_{\text{prop}}(z) \cdot \mathcal{S}_{\text{optic}}(\phi) \cdot \mathcal{S}_{\text{prop}}(-z_0) \\ \mathcal{S}_{\text{optic}}(\phi) &= \mathcal{S}_{\text{tilt}}(\alpha) \cdot \mathcal{S}_{\text{rot}}(\phi) \cdot \mathcal{S}_{\text{toroid}} \cdot \mathcal{S}_{\text{rot}}^{-1}(\phi) \cdot \mathcal{S}_{\text{tilt}}^{-1}(\alpha) \end{aligned} \quad (6.6)$$

representing the propagation from mean waist position in the beam system z_0 to the camera position z . With the system matrix $\mathcal{S}(\phi, z)$, equation (3.42) defines the mapping procedure of 2D

intensity information into the reciprocal 4D phase space. The corresponding program code which was developed for Wolfram Mathematica is given in chapter A.2. The reconstruction proceeds as described in section 6.2. Finally, the derived Wigner distribution function describes the laser beam at its mean waist position before being reflected by the mirror.

Before the reconstruction starts, mean waist position z_0 and Rayleigh length z_R in the beam system need to be determined. Thus, for the aligned case $\phi = 0$, the parameters z'_0 , z'_R and d'_0 are first derived in the camera system, separately for x - and y -direction as described in section 5.1.2. Then, a 2×2 beam matrix is generated at the horizontal waist position $z'_{0,x}$ by

$$\mathcal{M}'_x = \begin{pmatrix} (d'_{0,x}/4)^2 & 0 \\ 0 & (d'_{0,x}/4z'_{R,x})^2 \end{pmatrix}. \quad (6.7)$$

Transformation of \mathcal{M}'_x into the beam system is accomplished by the 2×2 propagation matrix $\mathcal{S}_x = \mathcal{S}_{\text{prop}}(z'_{0,x}) \cdot \mathcal{S}_{\text{optic}}(\phi = 0)$ and the propagation relation

$$\mathcal{M}_x = \mathcal{S}_x^{-1} \cdot \mathcal{M}'_x \cdot (\mathcal{S}_x^{-1})^T. \quad (6.8)$$

From the resulting beam matrix \mathcal{M}_x , the horizontal beam parameters $z_{0,x}$ and $z_{R,x}$ are derived by relation (3.5). Correspondingly, this procedure is applied for the vertical direction and then, mean values are computed for waist position and Rayleigh length in the beam system.

6.5.3 Experiment and theory

In this section, it should be proved, that the presented setup is capable of capturing the Wigner distribution function of complex and non-separable beams. The aim is to generate specific Hermite-Gaussian beams, also denoted as TEM modes, which can be described theoretically. This way, a comparison can be drawn between experimental results and theoretical descriptions.

The Wigner distribution function of a Hermite-Gaussian beam is given by $h_{nm}(\vec{x}, \vec{u}) = h_n(x, u) \cdot h_m(y, v)$ with [108]

$$h_n(x, u) = \frac{(-1)^n}{\pi} \exp \left[-\frac{8x^2}{d_{0,x}^2} - \frac{8u^2}{\theta_x^2} \right] L_n \left[2 \left(\frac{8x^2}{d_{0,x}^2} + \frac{8u^2}{\theta_x^2} \right) \right] \quad (6.9)$$

where $\theta_x = 4\lambda/(\pi d_{0,x})$ sets the divergence in relation to the waist diameter and L_n denotes the Laguerre polynomial of degree n . Single TEM modes result in a global degree of coherence $K = 1$ and in a high order, they exhibit complex intensity profiles as can be seen in figure 6.15. However, they are always separable. In contrast, the uncorrelated superposition of a TEM_{10} and a TEM_{01} beam

$$h_{\text{sp}}(\vec{x}, \vec{u}) = h_{10}(\vec{x}, \vec{u}) + h_{01}(\vec{x}, \vec{u}) \quad (6.10)$$

is non-separable. Here, the global degree of coherence is $K = 0.5$. In this case, the intensity profile shows a ring structure as depicted in figure 6.15(d).

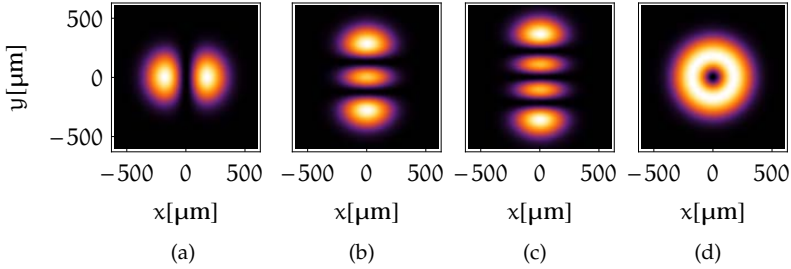


Figure 6.15: Intensity profiles of different TEM modes. The single modes TEM_{10} , TEM_{02} and TEM_{03} are shown in (a), (b) and (c). In (d), an uncorrelated superposition of a TEM_{10} and a TEM_{01} beam is depicted.

Wigner distribution functions of Hermite-Gaussian beams are depicted in figure 6.16 as derived from theory and experiment up to order $n = 3$. Qualitatively, it is revealed that the measured data sets suffice to successfully reconstruct the WDF of the chosen modes. Sub-figures 6.16(a) and 6.16(b) show the vertical and horizontal projection resulting for a TEM_{10} beam, corresponding to a Hermite-Gaussian mode of the order $n = 1$ and $m = 0$. Obviously, the 4D distribution separates properly into horizontal and vertical mode. Sub-figures 6.16(a) and 6.16(b) are produced from a TEM_{02} and TEM_{03} beam.

In summary, the theoretical distributions could well be reproduced in the experiment. However, numerical artifacts cannot entirely be avoided leading to small deviations from a perfect reconstruction. On the other hand, it is possible that the experimental beam contains tiny contributions of deviant modes or amplified spontaneous emission, too.

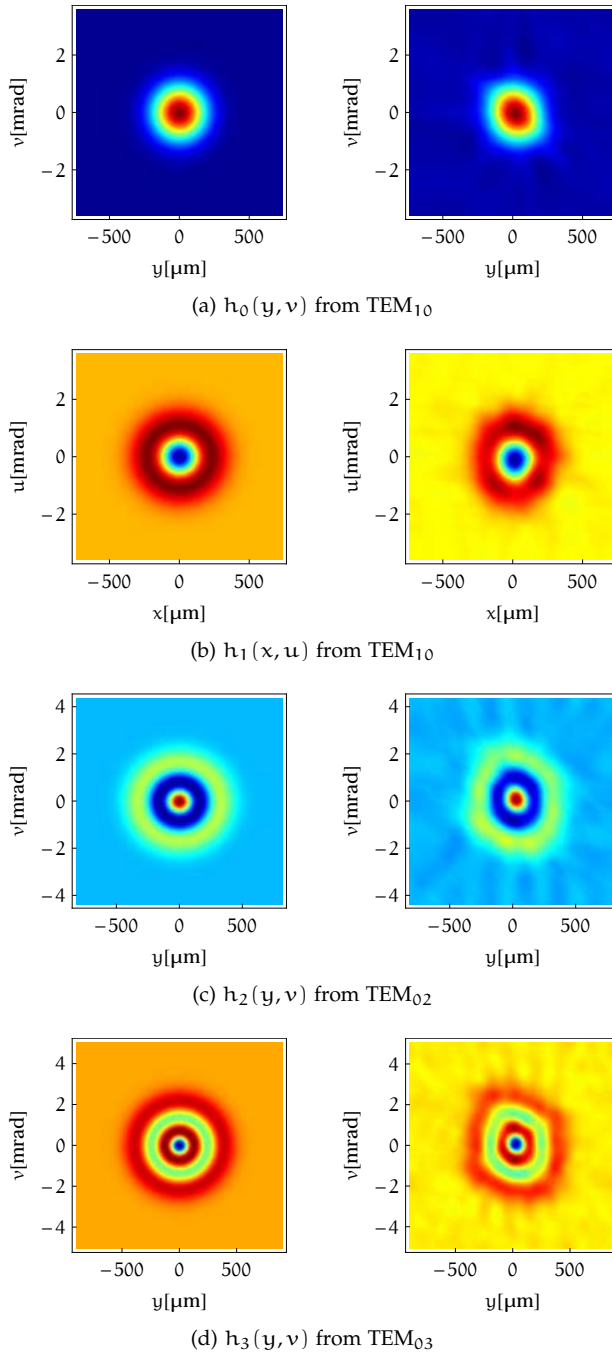


Figure 6.16: Wigner distribution functions of different Hermite-Gaussian beams in theory (left) and experiment (right). h_0 and h_1 represent horizontal and vertical projections from the 4D WDF of a TEM_{10} mode. h_2 and h_3 result from TEM_{02} and TEM_{03} beams.

The Wigner distribution function of the non-separable superposition $\text{TEM}_{10} + \text{TEM}_{01}$ is shown in figure 6.17. Projections of the 4D WDF are employed for visualization whereas in theory, both projections are identical. Thus, only the horizontal distribution is shown. Again, the theoretical prediction is well resembled by the measurement. Here, the experimental distributions appear slightly sheared in opposing directions indicating a small astigmatic aberration. This could be expected since the laser resonator was tweaked strongly in order to produce this particular beam.

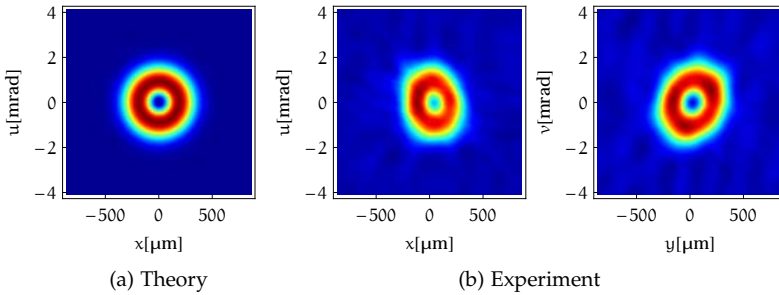


Figure 6.17: Wigner distribution function of the uncorrelated superposition $\text{TEM}_{10} + \text{TEM}_{01}$ in theory (a) and experiment (b). Projections from the 4D distribution are shown.

Quantitatively, the derived WDFs are characterized by the global degree of coherence K . Theoretical and experimental values of five different beams are given in table 6.5. A comparison shows good agreement, only small variations of below 10% can be found. As already mentioned, the investigated beams could contain small amounts of parasitic modes leading to a slight reduction of the coherence. The same effect arises from amplified spontaneous emission, which was weakly present during the experiment. Thus, it can well be that the accuracy of the algorithm is even better than 10%.

Table 6.5: Global degree of coherence K for different Hermite-Gaussian beams in theory and experiment.

	TEM_{00}	TEM_{10}	TEM_{02}	TEM_{03}	$\text{TEM}_{10} + \text{TEM}_{01}$
Theory	1	1	1	1	0.5
Experiment	0.95	1.06	0.98	0.90	0.46

Finally, the presented results prove the capability of the system to capture the Wigner distribution function of non-separable and complex beam structures. The use of a reflecting optic allows application to EUV and soft x-ray beams, as produced by FELs and synchrotrons. However, then the employed toroidal mirror has to meet additional requirements, i.e., surface roughness and shape accuracy should amount less than the wavelength of the investigated radiation.

SUMMARY

This work addresses EUV and soft x-ray radiation in terms of beam generation, transport and coherence. Knowledge and control of these three aspects are fundamental for corresponding applications, such as EUV lithography, spectral analysis of molecules or high resolution imaging in the water window with and without lenses. Mostly, these methods have been developed at large scale facilities as synchrotrons or FELs. However, further dissemination of such enabling technologies requires availability of simple and compact beam sources that provide a sufficient number of photons.

Thus, in a first part the brilliance enhancement of a clean laser produced plasma source is demonstrated for the generation of water window radiation. The idea is that by increasing the density of a gaseous Nitrogen target, a higher number of particles is ionized and more soft x-ray photons are produced. For that purpose, a low pressure ambient atmosphere is applied to the supersonic gas jet leading to a barrel shock. A plasma that is generated in an associated high density region becomes seven times brighter and slightly smaller and hence, the source brilliance increases by one order of magnitude. As a side effect, the erosion of the nozzle is minimized since the optimized plasma is situated in a nearly four times greater distance to it.

Generally, all applications of the plasma source benefit from that optimization. In particular, it facilitates the construction of a compact x-ray microscope with reasonable means [160]. Where so far, only sophisticated liquid targets resulted in acceptable exposure times, now a simple and clean target concept permits microscopic x-ray imaging at magnifications up to 500x within minutes.

Besides the provision of a sufficient number of photons, a proper beam transport is equally important to achieve an optimum intensity at sample position. With a Hartmann type wavefront sensor, this property is investigated at an HHG setup where toroidal gratings achieve both, spectral filtering and focusing of EUV radiation. In an online adjustment it is revealed that already a tiny misalignment of these optical elements leads to significant aberrations and a corresponding loss of intensity. A theoretical approach confirms the observed results. The conducted alignment increases the high-

est achievable intensity by a factor of two. For CDI experiments this procedure is also crucial in order to achieve a flat phase distribution at sample position which prevents reconstruction errors of phase shifting objects.

The last part of this work focuses on coherence properties of EUV beams. Employing the concept of the Wigner distribution function, this special property is characterized for the free-electron laser FLASH by capturing intensity profiles behind the ellipsoidal beam-line mirror. With respect to existing publications of interference experiments, this investigation results in a surprisingly low value for the global degree of coherence. The influence of pulse to pulse fluctuations and a possible lack of experimental data is studied. Nevertheless, these effects can not explain the observed discrepancy of one order of magnitude entirely. It is conceivable that this discrepancy is also a result of different wavelengths of the FEL beam, and that in fact, the coherence is lower at a higher wavelength as it was present during the Wigner measurement.

Since the employed setup provides access to a 3D sub-manifold of the 4D phase space only, an extension of the measurement by a rotatable toroidal mirror is proposed. The proper functionality is proved with complex and non-separable beams provided by a near IR laser that generates Hermite-Gaussian modes and their superpositions. A comparison is drawn between theoretical expectations and experimental results, revealing a good agreement. Application of the system to FEL sources can easily be accomplished, since only reflective optics are employed. In the future, the attainable knowledge of the entire mutual coherence function provides the basis for further developments in the field of coherent imaging. It enables successful CDI experiments with less coherent beams, it improves reconstruction procedures by providing an initial guess, and, by knowing the illumination function, the influence of aberrations can be eliminated.

APPENDIX

A.1 RAY TRANSFORMATION MATRICES

The following ray transformation matrices can be found in [161, 162, 108].

- Free propagation by a distance z

$$\mathcal{S}_{\text{prop}}(z) = \begin{pmatrix} 1 & 0 & z & 0 \\ 0 & 1 & 0 & z \\ 0 & 0 & 1 & 0 \\ 0 & 0 & 0 & 1 \end{pmatrix} \quad (\text{A.1})$$

- Cylindrical lens with focal lengths f_x and f_y

$$\mathcal{S}_{\text{lens}} = \begin{pmatrix} 1 & 0 & 0 & 0 \\ 0 & 1 & 0 & 0 \\ -1/f_x & 0 & 1 & 0 \\ 0 & -1/f_y & 0 & 1 \end{pmatrix} \quad (\text{A.2})$$

- Toroidal mirror with tangential radius R_t and sagittal radius R_s

$$\mathcal{S}_{\text{toroid}} = \begin{pmatrix} 1 & 0 & 0 & 0 \\ 0 & 1 & 0 & 0 \\ -2/R_t & 0 & 1 & 0 \\ 0 & -2/R_s & 0 & 1 \end{pmatrix} \quad (\text{A.3})$$

- Rotation by an angle ϕ about z-axis

$$\mathcal{S}_{\text{rot}}(\phi) = \begin{pmatrix} \cos(\phi) & -\sin(\phi) & 0 & 0 \\ \sin(\phi) & \cos(\phi) & 0 & 0 \\ 0 & 0 & \cos(\phi) & -\sin(\phi) \\ 0 & 0 & \sin(\phi) & \cos(\phi) \end{pmatrix} \quad (\text{A.4})$$

- Tilt by an angle α about y-axis

$$\mathcal{S}_{\text{tilt}}(\alpha) = \begin{pmatrix} \sqrt{\cos(\alpha)} & 0 & 0 & 0 \\ 0 & \frac{1}{\sqrt{\cos(\alpha)}} & 0 & 0 \\ 0 & 0 & \frac{1}{\sqrt{\cos(\alpha)}} & 0 \\ 0 & 0 & 0 & \sqrt{\cos(\alpha)} \end{pmatrix} \quad (\text{A.5})$$

- Toroidal grating with tangential radius R_t and sagittal radius R_s , incidence angle α and deflection angle β

$$\mathcal{S}_{\text{tg}} = \begin{pmatrix} M_{\text{mag}} & 0 & 0 & 0 \\ 0 & 1 & 0 & 0 \\ -2/R'_t & 0 & 1/M_{\text{mag}} & 0 \\ 0 & -2/R'_s & 0 & 1 \end{pmatrix} \quad (\text{A.6})$$

with

$$\begin{aligned} R'_t &= \frac{2 \cos(\alpha) \cos(\beta)}{\cos(\alpha) + \cos(\beta)} R_t \\ R'_s &= \frac{2}{\cos(\alpha) + \cos(\beta)} R_s \\ M_{\text{mag}} &= \frac{\cos(\beta)}{\cos(\alpha)} \\ \beta(\alpha) &= \arcsin(m \lambda g + \sin(\alpha)) \end{aligned}$$

where m denotes the diffraction order and g the groove density.

A.2 WIGNER RECONSTRUCTION ALGORITHM

Here, the program code is presented that is employed to reconstruct the Wigner distribution function from intensity profiles. This algorithm was developed within the environment of the Wolfram Mathematica 8 [132]. In order to preserve a reasonable length of this chapter, the focus is put on the core components of the program.

Module A.1: The function Mapping2D has three arguments: *distrib* is a list of one-dimensional, Fourier transformed discrete intensity profiles, where each profile is measured at a position z_i . *m* is a list of the positions z_i , divided by the mean Rayleigh length z_R . *hsize* is a positive integer that determines the size of the computed 2D array. Mapping2D returns a 2D array *h*, representing the Wigner distribution of a separable beam in Fourier space.

```

Mapping2D[distrib_, m_, hsize_] := Block[{matrix = Table[0, {z, 1, 2}, {k
    , 1, hsize}, {l, 1, hsize}]},

imax = Length[distrib[[1]]];

Do[
b = 1/2 * (hsize - m[[z]] * hsize);

If[-1 <= m[[z]] <= 1,

Do[
icoord = Round[(i - .5) / imax * hsize + .5];
jcoord = Round[m[[z]] * (i - .5) / imax * hsize + b + .5];
matrix[[1, jcoord, icoord]] = matrix[[1, jcoord, icoord]] + distrib[[z, i
    ]];
matrix[[2, jcoord, icoord]] = matrix[[2, jcoord, icoord]] + 1;
, {i, 1, imax}],

Do[
icoord = Round[((j - .5) / imax * hsize - b) / m[[z]] + .5];
jcoord = Round[(j - .5) / imax * hsize + .5];
matrix[[1, jcoord, icoord]] = matrix[[1, jcoord, icoord]] + distrib[[z, j
    ]];
matrix[[2, jcoord, icoord]] = matrix[[2, jcoord, icoord]] + 1;
, {j, 1, imax}
]
, {z, 1, Length[distrib]};

matrix[[2]] = Table[
If[matrix[[2, j, i]] != 0,

```

```

matrix[[2,j,i],
1]
,{j,1,Length[matrix[[2]]]}, {i,1,Length[matrix[[2,1]]]};

matrix[[1]]/matrix[[2]]

```

Module A.2: The function Mapping3D has three arguments: *fourier* is a list of two-dimensional, Fourier transformed discrete intensity profiles, where each profile is measured at a position z_i . *m* is a list of the positions z_i , divided by the mean Rayleigh length z_R . *hsize* is a positive integer that determines the size of the computed 4D array. Mapping3D returns a 4D array *h*, representing the Wigner distribution of a non-separable beam in Fourier space.

```

Mapping3D[fourier_, m_, hsize_] := Block[{h, hcount, ymax, xmax, b, k, l, i,
j},

h=ConstantArray[0.+0.I, {hsize, hsize, hsize, hsize}];
hcount=ConstantArray[0, {hsize, hsize, hsize, hsize}];

ymax=Length[fourier[[1]]];
xmax=Length[fourier[[1,1]]];

Do[

b=1/2*(hsize-m[[zi]]*hsize);

If[-1<=m[[zi]]<=1,

Do[
i=Round[(x-.5)/xmax*hsize+.5];
j=Round[(y-.5)/ymax*hsize+.5];
k=Round[(m[[zi]]*(x-.5))/xmax*hsize+b+.5];
l=Round[(m[[zi]]*(y-.5))/ymax*hsize+b+.5];
hcount[[l,k,j,i]]=hcount[[l,k,j,i]]+1;
h[[l,k,j,i]]=h[[l,k,j,i]]+fourier[[zi,y,x]];
,{y,1,ymax},{x,1,xmax}],

Do[
k=Round[(x-.5)/xmax*hsize+.5];
l=Round[(y-.5)/ymax*hsize+.5];
i=Round[((x-.5)/xmax*hsize-b)/m[[zi]]+.5];
j=Round[((y-.5)/ymax*hsize-b)/m[[zi]]+.5];
hcount[[l,k,j,i]]=hcount[[l,k,j,i]]+1;
h[[l,k,j,i]]=h[[l,k,j,i]]+fourier[[zi,y,x]];
,{y,1,ymax},{x,1,xmax}]]

```

```

]
,{zi,1,Length[fourier]}};

entries=Position[hcount,x_/;x>0];

Do[
h[[entries[[n,1]],entries[[n,2]],entries[[n,3]],entries[[n,4]]]=
  h[[entries[[n,1]],entries[[n,2]],entries[[n,3]],entries[[n
  ,4]]]/hcount[[entries[[n,1]],entries[[n,2]],entries[[n,3]],
  entries[[n,4]]]];
,{n,1,Length[entries]}};

h]

```

Module A.3: Here, the mapping procedure of the 4D Wigner measurement is described. First, the propagation matrices are defined and the system matrix \mathcal{S} is derived. Then, \mathcal{S} is evaluated for all captured intensity profiles with the corresponding parameters (α , R_1 , R_2 , ϕ , z_0 , z , see section 6.5.2) which are comprised in the list *parameters*. The derived system matrices are listed in the global variable Sn . The function Mapping4D has two arguments: *fourier* is a list of two-dimensional, Fourier transformed discrete intensity profiles. *hsize* is a positive integer that determines the size of the computed 4D array. Mapping4D returns a 4D array h , representing the Wigner distribution of a non-separable beam in Fourier space.

```

Sprop[z_] := {
{1, 0, z, 0},
{0, 1, 0, z},
{0, 0, 1, 0},
{0, 0, 0, 1}};

Stilt[\[Alpha]_] := {
{Sqrt[Sin[\[Alpha]]], 0, 0, 0},
{0, 1/Sqrt[Sin[\[Alpha]]], 0, 0},
{0, 0, 1/Sqrt[Sin[\[Alpha]]], 0},
{0, 0, 0, Sqrt[Sin[\[Alpha]]]}};

Storoid[R1_, R2_] := {
{1, 0, 0, 0},
{0, 1, 0, 0},
{-2/R1, 0, 1, 0},
{0, -2/R2, 0, 1}};

```

```

Srot[\[Phi]_] := {
{Cos\[Phi], Sin\[Phi], 0, 0},
{-Sin\[Phi], Cos\[Phi], 0, 0},
{0, 0, Cos\[Phi], Sin\[Phi]},
{0, 0, -Sin\[Phi], Cos\[Phi]}};

S[zcam_, \[Alpha]_, \[Phi]_, R1_, R2_, zbeam_] := FullSimplify[
Sprop[zcam].Stilt\[Alpha].Srot\[Phi].Storoid[R1, R2].Inverse[
Srot\[Phi]].Inverse[Stilt\[Alpha]].Sprop[zbeam]
];

Sn=Table[S[parameters[[n,6]],parameters[[n,4]]Degree,-parameters
[[n,5]]Degree,parameters[[n,2]],parameters[[n,3]],-(z0mean)
],{n,1,Length[parameters]}};

ScalingUV=1/(zRmean);

Mapping4D[fourier_,hsize_]:=Block[{h,hcount,ymax,xmax,k,l,i,j},

h=ConstantArray[0.+0.I,{hsize,hsize,hsize,hsize}];
hcount=ConstantArray[0,{hsize,hsize,hsize,hsize}];

ymax=Length[fourier[[1]]];
xmax=Length[fourier[[1,1]]];

Do[
Do[

i=Round[Sn[[n,1,1]](x-.5)/xmax*hsize + Sn[[n,2,1]](y-.5)/ymax*
hsize+.5+1/2 hsize(1-Sn[[n,1,1]]-Sn[[n,2,1]])];
j=Round[Sn[[n,1,2]](x-.5)/xmax*hsize + Sn[[n,2,2]](y-.5)/ymax*
hsize+.5+1/2 hsize(1-Sn[[n,1,2]]-Sn[[n,2,2]])];
k=Round[ScalingUV*Sn[[n,1,3]](x-.5)/xmax*hsize + ScalingUV*Sn[[n
,2,3]](y-.5)/ymax*hsize+.5+1/2 hsize(1-ScalingUV*Sn[[n
,1,3]]-ScalingUV*Sn[[n,2,3]])];
l=Round[ScalingUV*Sn[[n,1,4]](x-.5)/xmax*hsize + ScalingUV*Sn[[n
,2,4]](y-.5)/ymax*hsize+.5+1/2 hsize(1-ScalingUV*Sn[[n
,1,4]]-ScalingUV*Sn[[n,2,4]])];
If[1<=i<=hsize && 1<=j<=hsize && 1<=k<=hsize && 1<=l<=hsize,
hcount[[l,k,j,i]]=hcount[[l,k,j,i]]+1;
h[[l,k,j,i]]=h[[l,k,j,i]]+fourier[[n,y,x]]];

,{y,1,ymax},{x,1,xmax}};
,{n,1,Length[fourier]}};

entries=Position[hcount,x_/;x>0];

```

```
Do[
h[[entries[[n,1]],entries[[n,2]],entries[[n,3]],entries[[n,4]]]=
  h[[entries[[n,1]],entries[[n,2]],entries[[n,3]],entries[[n
    ,4]]]/hcount[[entries[[n,1]],entries[[n,2]],entries[[n,3]],
    entries[[n,4]]]];
,{n,1,Length[entries]};
h]
```


BIBLIOGRAPHY

- [1] D. Attwood, *Soft x-rays and extreme ultraviolet radiation*. Cambridge University Press, 1999.
- [2] V. Bakshi, ed., *EUV Lithography*. SPIE Press, 2008.
- [3] B. Wu and A. Kumar, "Extreme ultraviolet lithography: A review," *Journal of Vacuum Science & Technology B*, vol. 25, no. 6, pp. 1743–1761, 2007.
- [4] F. Scholze, B. Beckhoff, G. Brandt, *et al.*, "New PTB beamlines for high-accuracy EUV reflectometry at BESSY II," *Soft X-Ray and EUV Imaging Systems*, vol. 72, Nov 2000.
- [5] F. Scholze and L. Christian, "Use of EUV scatterometry for the characterization of line profiles and line roughness on photomasks," in *Mask and Lithography Conference (EMLC), 2008 24th European*, 2008.
- [6] M. Banyay and L. Juschkin, "Table-top reflectometer in the extreme ultraviolet for surface sensitive analysis," *Applied Physics Letters*, vol. 94, no. 6, p. 063507, 2009.
- [7] J. Chen, "NEXAFS investigations of transition metal oxides, nitrides, carbides, sulfides and other interstitial compounds," *Surface Science Reports*, vol. 30, pp. 1–152, Jan 1997.
- [8] C. Peth, F. Barkusky, and K. Mann, "Near-edge x-ray absorption fine structure measurements using a laboratory-scale XUV source," *Journal of Physics D*, vol. 41, p. 105202, May 2008.
- [9] J. Stöhr, *NEXAFS Spectroscopy (Springer Series in Surface Sciences)*. Springer, 2003.
- [10] L. B. Da Silva, J. E. Trebes, R. Balhorn, *et al.*, "X-ray laser microscopy of rat sperm nuclei," *Science*, vol. 258, pp. 269–271, Oct 1992.
- [11] M. Berglund, L. Rymell, M. Peuker, *et al.*, "Compact water-window transmission X-ray microscopy," *Journal of Microscopy*, vol. 197, pp. 268–273, Mar 2000.
- [12] H. Hertz, M. Bertilson, O. v. Hofsten, *et al.*, "Laboratory X-ray microscopy for high-resolution imaging of environmental

- colloid structure," *Chemical Geology*, vol. 329, pp. 26–31, Nov 2012.
- [13] H. N. Chapman, A. Barty, M. J. Bogan, *et al.*, "Femtosecond diffractive imaging with a soft-X-ray free-electron laser," *Nature Physics*, vol. 2, pp. 839–843, Dec 2006.
- [14] H. N. Chapman, P. Fromme, A. Barty, *et al.*, "Femtosecond X-ray protein nanocrystallography," *Nature*, vol. 470, pp. 73–77, Feb 2011.
- [15] M. M. Seibert, T. Ekeberg, F. R. N. C. Maia, *et al.*, "Single mimivirus particles intercepted and imaged with an X-ray laser," *Nature*, vol. 470, pp. 78–81, Feb 2011.
- [16] W. Hoppe, "Trace structure analysis, ptychography, phase tomography," *Ultramicroscopy*, vol. 10, pp. 187–198, Jan 1982.
- [17] R. N. Wilke, M. Priebe, M. Bartels, *et al.*, "Hard X-ray imaging of bacterial cells: nano-diffraction and ptychographic reconstruction," *Optics Express*, vol. 20, p. 19232, Aug 2012.
- [18] R. Rakowski, A. Bartnik, H. Fiedorowicz, *et al.*, "Characterization and optimization of the laser-produced plasma EUV source at 13.5 nm based on a double-stream Xe/He gas puff target," *Applied Physics B*, vol. 101, pp. 773–789, Dec 2010.
- [19] A. K. Rebrov, "Free jets in vacuum technologies," *Journal of Vacuum Science & Technology A*, vol. 19, no. 4, pp. 1679–1987, 2001.
- [20] J. Spence, U. Weierstall, and M. Howells, "Coherence and sampling requirements for diffractive imaging," *Ultramicroscopy*, vol. 101, pp. 149–152, Nov 2004.
- [21] L. W. Whitehead, G. J. Williams, H. M. Quiney, *et al.*, "Diffractive Imaging Using Partially Coherent X Rays," *Physical Review Letters*, vol. 103, p. 243902, Dec 2009.
- [22] B. Chen, B. Abbey, R. Dilanian, *et al.*, "Diffraction imaging: The limits of partial coherence," *Physical Review B*, vol. 86, p. 235401, Dec 2012.
- [23] A. Singer, F. Sorgenfrei, A. P. Mancuso, *et al.*, "Spatial and temporal coherence properties of single free-electron laser pulses," *Optics Express*, vol. 20, pp. 17480–17495, Jul 2012.

- [24] D. D. Mai, J. Hallmann, T. Reusch, *et al.*, "Single pulse coherence measurements in the water window at the free-electron laser FLASH," *Optics Express*, vol. 21, p. 13005, Jun 2013.
- [25] A. Singer, U. Lorenz, F. Sorgenfrei, *et al.*, "Hanbury Brown-Twiss Interferometry at a Free-Electron Laser," *Physical Review Letters*, vol. 111, Jul 2013.
- [26] H. E. Hinteregger, K. R. Damon, and L. A. Hall, "Analysis of photoelectrons from solar extreme ultraviolet," *Journal of Geophysical Research*, vol. 64, pp. 961–969, 1959.
- [27] G. Schmidtke, W. Schweizer, and M. Knothe, "The AEROS-EUV spectrometer," *Zeitschrift für Geophysik*, vol. 40, pp. 577–584, 1974.
- [28] J.-P. Delaboudinière, G. E. Artzner, J. Brunaud, *et al.*, "EIT: Extreme-UltraViolet Imaging Telescope for the SOHO Mission," in *The SOHO Mission* (B. Fleck, V. Domingo, and A. Poland, eds.), pp. 291–312, Springer Netherlands, 1995.
- [29] S. Krucker and A. O. Benz, "Energy Distribution of Heating Processes in the Quiet Solar Corona," *The Astrophysical Journal*, vol. 501, pp. 213–216, Jul 1998.
- [30] W. C. Röntgen, "Über eine neue Art von Strahlen," *Annalen der Physik*, vol. 300, no. 1, pp. 1–11, 1898.
- [31] A. Egbert, B. Mader, A. Ostendorf, *et al.*, "Compact electron-based extreme ultraviolet source at 13.5 nm," *Journal of Micro/Nanolithography, MEMS, and MOEMS*, vol. 2, pp. 136–139, Apr 2003.
- [32] F. Elder, A. Gurewitsch, R. Langmuir, *et al.*, "Radiation from Electrons in a Synchrotron," *Physical Review*, vol. 71, pp. 829–830, Jun 1947.
- [33] H. Motz, W. Thon, and R. N. Whitehurst, "Experiments on Radiation by Fast Electron Beams," *Journal of Applied Physics*, vol. 24, no. 7, p. 826, 1953.
- [34] H. Daido, "Review of soft x-ray laser researches and developments," *Reports on Progress in Physics*, vol. 65, pp. 1513–1576, Oct 2002.
- [35] K. A. Janulewicz, A. Lucianetti, G. Priebe, *et al.*, "Review of state-of-the-art and output characteristics of table-top soft x-ray lasers," *X-Ray Spectrometry*, vol. 33, pp. 262–266, Jul 2004.

- [36] J. Trebes, K. Nugent, S. Mrowka, *et al.*, "Measurement of the spatial coherence of a soft-x-ray laser," *Physical Review Letters*, vol. 68, pp. 588–591, Feb 1992.
- [37] M. Nishikino, M. Tanaka, K. Nagashima, *et al.*, "Demonstration of a soft-x-ray laser at 13.9 nm with full spatial coherence," *Physical Review A*, vol. 68, p. 061802(R), Dec 2003.
- [38] Y. Wang, E. Granados, M. Larotonda, *et al.*, "High-Brightness Injection-Seeded Soft-X-Ray-Laser Amplifier Using a Solid Target," *Physical Review Letters*, vol. 97, p. 123901, Sep 2006.
- [39] F. Barkusky, A. Bayer, C. Peth, *et al.*, "Direct photoetching of polymers using radiation of high energy density from a table-top extreme ultraviolet plasma source," *Journal of Applied Physics*, vol. 105, no. 1, p. 014906, 2009.
- [40] S. J. Haney, K. W. Berger, G. D. Kubiak, *et al.*, "Prototype high-speed tape target transport for a laser plasma soft-x-ray projection lithography source," *Applied Optics*, vol. 32, pp. 6934–6937, Dec 1993.
- [41] C. Wagner and N. Harned, "EUV lithography: Lithography gets extreme," *Nature Photonics*, vol. 4, pp. 24–26, Jan 2010.
- [42] C. Peth, A. Kalinin, F. Barkusky, *et al.*, "XUV laser-plasma source based on solid Ar filament," *Review of Scientific Instruments*, vol. 78, no. 10, p. 103509, 2007.
- [43] B. A. M. Hansson, O. Hemberg, H. M. Hertz, *et al.*, "Characterization of a liquid-xenon-jet laser-plasma extreme-ultraviolet source," *Review of Scientific Instruments*, vol. 75, no. 6, pp. 2122–2129, 2004.
- [44] U. Vogt, R. Frueke, T. Wilhein, *et al.*, "High-resolution spatial characterization of laser produced plasmas at soft x-ray wavelengths," *Applied Physics B*, vol. 78, pp. 53–58, Jan 2004.
- [45] P. A. C. Jansson, B. A. M. Hansson, O. Hemberg, *et al.*, "Liquid-tin-jet laser-plasma extreme ultraviolet generation," *Applied Physics Letters*, vol. 84, no. 13, pp. 2256–2258, 2004.
- [46] M. Richardson, C.-S. Koay, K. Takenoshita, *et al.*, "High conversion efficiency mass-limited Sn-based laser plasma source for extreme ultraviolet lithography," *Journal of Vacuum Science & Technology B*, vol. 22, no. 2, pp. 785–790, 2004.

- [47] M. Wieland, T. Wilhein, M. Faubel, *et al.*, "EUV and fast ion emission from cryogenic liquid jet target laser-generated plasma," *Applied Physics B*, vol. 72, pp. 591–597, Apr 2001.
- [48] V. Bakshi, ed., *EUV Sources for Lithography*. SPIE Press, 2006.
- [49] L. Rymell and H. M. Hertz, "Debris elimination in a droplet-target laser-plasma soft x-ray source," *Review of Scientific Instruments*, vol. 66, no. 10, pp. 4916–4920, 1995.
- [50] T. Mey, M. Rein, P. Großmann, *et al.*, "Brilliance improvement of laser-produced soft x-ray plasma by a barrel shock," *New Journal of Physics*, vol. 14, p. 073045, Jul 2012.
- [51] H. Fiedorowicz, A. Bartnik, R. Jarocki, *et al.*, "Compact laser plasma EUV source based on a gas puff target for metrology applications," *Journal of Alloys and Compounds*, vol. 401, pp. 99–103, Sep 2005.
- [52] C. G. Morgan, "Laser-induced breakdown of gases," *Reports on Progress in Physics*, vol. 38, pp. 621–665, May 1975.
- [53] H. Fiedorowicz, A. Bartnik, M. Szczurek, *et al.*, "Investigation of soft X-ray emission from a gas puff target irradiated with a Nd:YAG laser," *Optics Communications*, vol. 163, pp. 103–114, May 1999.
- [54] M. Müller, F. C. Kühn, P. Großmann, *et al.*, "Emission properties of ns and ps laser-induced soft x-ray sources using pulsed gas jets," *Optics Express*, vol. 21, p. 12831, May 2013.
- [55] T. Mayer-Kuckuk, *Atomphysik*. Teubner Verlag, 1997.
- [56] H. Komori, Y. Ueno, H. Hoshino, *et al.*, "EUV radiation characteristics of a CO₂ laser produced Xe plasma," *Applied Physics B*, vol. 83, pp. 213–218, May 2006.
- [57] K. Wiegardt, *Theoretische Strömungslehre*. Universitätsverlag Göttingen, 2005.
- [58] J. Spurk and N. Aksel, *Strömungslehre*. Springer Berlin Heidelberg, 2010.
- [59] C. Peth, S. Kranzusch, K. Mann, *et al.*, "Characterization of gas targets for laser produced extreme ultraviolet plasmas with a Hartmann-Shack sensor," *Review of Scientific Instruments*, vol. 75, pp. 3288–3293, Oct 2004.

- [60] E. P. Muntz, B. B. Hamel, and B. L. Maguire, "Some Characteristics of Exhaust Plume Rarefaction," *AIAA Journal*, vol. 8, pp. 1651–1658, Sep 1970.
- [61] H. Ashkenas and F. S. Sherman, "The structure and utilization of supersonic free jets in low density wind tunnels," in *Proc. Fourth Symp. on Rarefied Gas Dynamics*, vol. 2, pp. 84–105, 1966.
- [62] T. Pfeifer, C. Spielmann, and G. Gerber, "Femtosecond x-ray science," *Reports on Progress in Physics*, vol. 69, pp. 443–505, Feb 2006.
- [63] P. Franken, A. Hill, C. Peters, *et al.*, "Generation of Optical Harmonics," *Physical Review Letters*, vol. 7, pp. 118–119, Aug 1961.
- [64] A. McPherson, G. Gibson, H. Jara, *et al.*, "Studies of multiphoton production of vacuum-ultraviolet radiation in the rare gases," *Journal of the Optical Society of America B*, vol. 4, pp. 595–601, Apr 1987.
- [65] M. Ferray, A. L'Huillier, X. F. Li, *et al.*, "Multiple-harmonic conversion of 1064 nm radiation in rare gases," *Journal of Physics B*, vol. 21, pp. L31–L35, Feb 1988.
- [66] P. Corkum, "Plasma perspective on strong field multiphoton ionization," *Physical Review Letters*, vol. 71, pp. 1994–1997, Sep 1993.
- [67] K. C. Kulander, K. J. Schafer, and J. L. Krause, "Dynamics of Short-Pulse Excitation, Ionization and Harmonic Conversion," *NATO ASI Series*, pp. 95–110, Nov 1995.
- [68] M. Lewenstein, P. Balcou, M. Ivanov, *et al.*, "Theory of high-harmonic generation by low-frequency laser fields," *Physical Review A*, vol. 49, pp. 2117–2132, Mar 1994.
- [69] P. M. Paul, E. S. Toma, P. Breger, *et al.*, "Observation of a Train of Attosecond Pulses from High Harmonic Generation," *Science*, vol. 292, pp. 1689–1692, Jun 2001.
- [70] X. Li, A. L'Huillier, M. Ferray, *et al.*, "Multiple-harmonic generation in rare gases at high laser intensity," *Physical Review A*, vol. 39, pp. 5751–5761, Jun 1989.
- [71] L. V. Keldysh, "Ionization in the field of a strong electromagnetic wave," *Soviet Physics JETP*, vol. 20, no. 5, pp. 1307–1314, 1965.

- [72] J. Schwinger, "On the Classical Radiation of Accelerated Electrons," *Physical Review*, vol. 75, pp. 1912–1925, Jun 1949.
- [73] J. D. Jackson, *Classical Electrodynamics Third Edition*. Wiley, 1998.
- [74] H. Motz, "Applications of the Radiation from Fast Electron Beams," *Journal of Applied Physics*, vol. 22, no. 5, p. 527, 1951.
- [75] J. M. J. Madey, "Stimulated Emission of Bremsstrahlung in a Periodic Magnetic Field," *Journal of Applied Physics*, vol. 42, no. 5, pp. 1906–1913, 1971.
- [76] D. A. G. Deacon, L. R. Elias, J. M. J. Madey, *et al.*, "First Operation of a Free-Electron Laser," *Physical Review Letters*, vol. 38, pp. 892–894, Apr 1977.
- [77] E. L. Saldin, E. A. Schneidmiller, and M. V. Yurkov, *The Physics of Free Electron Lasers*. Springer Berlin Heidelberg, 2000.
- [78] C. Pellegrini and S. Reiche, "The Development of X-Ray Free-Electron Lasers," *IEEE Journal of Selected Topics in Quantum Electronics*, vol. 10, pp. 1393–1404, Nov 2004.
- [79] B. McNeil, "Free electron lasers: First light from hard X-ray laser," *Nature Photonics*, vol. 3, pp. 375–377, Jul 2009.
- [80] B. W. J. McNeil and N. R. Thompson, "X-ray free-electron lasers," *Nature Photonics*, vol. 4, pp. 814–821, Dec 2010.
- [81] F. Grüner, S. Becker, U. Schramm, *et al.*, "Design considerations for table-top, laser-based VUV and X-ray free electron lasers," *Applied Physics B*, vol. 86, pp. 431–435, Jan 2007.
- [82] K. Nakajima, "Compact X-ray sources: Towards a table-top free-electron laser," *Nature Physics*, vol. 4, pp. 92–93, Feb 2008.
- [83] A. R. Maier, A. Meseck, S. Reiche, *et al.*, "Demonstration Scheme for a Laser-Plasma-Driven Free-Electron Laser," *Physical Review X*, vol. 2, p. 031019, Sep 2012.
- [84] Z. Huang and K.-J. Kim, "Review of x-ray free-electron laser theory," *Physical Review ST Accelerators and Beams*, vol. 10, p. 034801, Mar 2007.
- [85] P. Schmüser, M. Dohlus, and J. Rossbach, *Ultraviolet and Soft X-Ray Free-Electron Lasers*. Springer Berlin Heidelberg, 2009.

- [86] J. A. Clarke, *The Science and Technology of Undulators and Wigglers (Oxford Series on Synchrotron Radiation)*. Oxford University Press, USA, 2004.
- [87] S. Schreiber, B. Faatz, J. Feldhaus, *et al.*, "FEL user facility FLASH," in *Proceedings of IPAC'10, Kyoto, Japan*, pp. 2149–2151, 2010.
- [88] E. Allaria, A. Battistoni, F. Bencivenga, *et al.*, "Tunability experiments at the FERMI@Elettra free-electron laser," *New Journal of Physics*, vol. 14, p. 113009, Nov 2012.
- [89] S. Schreiber, B. Faatz, J. Feldhaus, *et al.*, "Status of the FEL user facility FLASH," in *Proceedings of FEL2011, Shanghai, China*, 267–270, 2011.
- [90] D. Douglas, "The Jefferson Lab 1 kW IR FEL," *eConf C*, vol. 000821, p. TH204, 2000.
- [91] D. Douglas, S. V. Benson, G. A. Krafft, *et al.*, "Driver Accelerator Design for the 10 kW Upgrade of the Jefferson Lab IR FEL," *eConf C*, vol. 000821, p. THc03, 2000.
- [92] G. Margaritondo and P. Rebernik Ribic, "A simplified description of x-ray free-electron lasers," *Journal of Synchrotron Radiation*, vol. 18, pp. 101–108, Mar 2011.
- [93] W. Ackermann, G. Asova, V. Ayvazyan, *et al.*, "Operation of a free-electron laser from the extreme ultraviolet to the water window," *Nature Photonics*, vol. 1, pp. 336–342, Jun 2007.
- [94] K. Tiedtke, A. Azima, N. von Bargen, *et al.*, "The soft x-ray free-electron laser FLASH at DESY: beamlines, diagnostics and end-stations," *New Journal of Physics*, vol. 11, p. 023029, Feb 2009.
- [95] E. L. Saldin, E. A. Schneidmiller, and M. V. Yurkov, "Statistical and coherence properties of radiation from x-ray free-electron lasers," *New Journal of Physics*, vol. 12, p. 035010, Mar 2010.
- [96] E. Allaria, R. Appio, L. Badano, *et al.*, "Highly coherent and stable pulses from the FERMI seeded free-electron laser in the extreme ultraviolet," *Nature Photonics*, vol. 6, pp. 699–704, Sep 2012.
- [97] J. Amann, W. Berg, V. Blank, *et al.*, "Demonstration of self-seeding in a hard-X-ray free-electron laser," *Nature Photonics*, vol. 6, pp. 693–698, Aug 2012.

- [98] I. Newton, *Opticks or, a Treatise of the reflexions, refractions, inflexions and colours of light*. 1704.
- [99] C. Huygens, *Traité de la Lumière*. 1690.
- [100] T. Young, "The Bakerian Lecture: Experiments and Calculations Relative to Physical Optics," *Philosophical Transactions of the Royal Society of London*, vol. 94, pp. 1–16, 1804.
- [101] J. C. Maxwell, "A Dynamical Theory of the Electromagnetic Field," *Philosophical Transactions of the Royal Society of London*, vol. 155, pp. 459–512, Jan 1865.
- [102] A. Einstein, "Über einen die Erzeugung und Verwandlung des Lichtes betreffenden heuristischen Gesichtspunkt," *Annalen der Physik*, vol. 322, no. 6, pp. 132–148, 1905.
- [103] M. J. Bastiaans, "The Wigner distribution function applied to optical signals and systems," *Optics Communications*, vol. 25, pp. 26–30, Apr 1978.
- [104] M. J. Bastiaans, "Wigner distribution function and its application to first-order optics," *Journal of the Optical Society of America*, vol. 69, pp. 1710–1716, Dec 1979.
- [105] M. J. Bastiaans, "Application of the Wigner distribution function to partially coherent light," *Journal of the Optical Society of America A*, vol. 3, p. 1227, Aug 1986.
- [106] M. J. Bastiaans, "Applications of the Wigner distribution function to partially coherent light beams," *Selected Papers from International Conference on Optics and Optoelectronics '98*, Apr 1999.
- [107] L. Mandel and E. Wolf, *Optical Coherence and Quantum Optics*. Cambridge University Press, 1995.
- [108] A. Torre, *Linear Ray and Wave Optics in Phase Space: Bridging Ray and Wave Optics via the Wigner Phase-Space Picture*. Elsevier Science, 2005.
- [109] B. Eppich, *Die Charakterisierung von Strahlungsfeldern mit der Wigner-Verteilung und deren Messung*. PhD thesis, Technische Universität Berlin, 1998.
- [110] M. Born and E. Wolf, *Principles of Optics: Electromagnetic Theory of Propagation, Interference and Diffraction of Light*. Cambridge University Press, 1999.

- [111] "ISO 15367-1: Lasers and laser-related equipment – Test methods for determination of the shape of a laser beam wavefront – Part 1: Terminology and fundamental aspects," 2003.
- [112] J. H. Poynting, "On the Transfer of Energy in the Electromagnetic Field," *Philosophical Transactions of the Royal Society of London*, vol. 175, pp. 343–361, Jan 1884.
- [113] B. Flöter, *Strahlcharakterisierung von Freie-Elektronen-Lasern im weichen Röntgen-Spektralbereich*. PhD thesis, Universität Göttingen, 2012.
- [114] W. Lauterborn and T. Kurz, *Coherent Optics: Fundamentals and Applications*. Springer, 2003.
- [115] R. Castenada and F. F. Medina, "On spatial coherence beams," *Optik*, vol. 109, pp. 77–83, 1998.
- [116] E. Wigner, "On the Quantum Correction For Thermodynamic Equilibrium," *Physical Review*, vol. 40, pp. 749–759, Jun 1932.
- [117] J. Paye, "The chronocyclic representation of ultrashort light pulses," *IEEE Journal of Quantum Electronics*, vol. 28, no. 10, pp. 2262–2273, 1992.
- [118] W. Meckenbräuer and F. Hlawatsch, eds., *The Wigner Distribution: Theory and Application in Signal Processing*. Elsevier, Amsterdam, 1997.
- [119] A. Walther, "Radiometry and coherence," *Journal of the Optical Society of America*, vol. 58, pp. 1256–1259, Sep 1968.
- [120] B. Eppich, G. Mann, and H. Weber, "Measurement of the four-dimensional Wigner distribution of paraxial light sources," *Optical Design and Engineering II*, Sep 2005.
- [121] C. Q. Tran, G. J. Williams, A. Roberts, *et al.*, "Experimental Measurement of the Four-Dimensional Coherence Function for an Undulator X-Ray Source," *Physical Review Letters*, vol. 98, May 2007.
- [122] B. Schäfer, B. Flöter, T. Mey, *et al.*, "FEL beam characterization from measurements of the wigner distribution function," *Nuclear Instruments and Methods in Physics Research Section A*, vol. 654, pp. 502–507, 2011.
- [123] P. Toft, *The Radon transform - theory and implementation*. PhD thesis, Technical University of Denmark, 1996.

- [124] D. Proch and T. Trickl, "A high-intensity multi-purpose piezo-electric pulsed molecular beam source," *Review of Scientific Instruments*, vol. 60, no. 4, p. 713, 1989.
- [125] T. X. Phuoc, "Laser spark ignition: experimental determination of laser-induced breakdown thresholds of combustion gases," *Optics Communications*, vol. 175, pp. 419–423, Mar 2000.
- [126] C. E. Moore, "Selected Tables of Atomic Spectra, Atomic Energy Levels and Multiplet Tables - N IV, N V, N VI, N VII," *National Standard Reference Data Series, NSRDS-NBS3 (Sect. 4)*, 1971.
- [127] W. M. Haynes, ed., *CRC Handbook of Chemistry and Physics, 94th Edition*. CRC Press, 2013.
- [128] G. Settles, *Schlieren & Shadowgraph Techniques*. Springer, 2006.
- [129] J. Hartmann, "Bemerkungen über den Bau und die Justierung von Spektrographen," *Zeitschrift für Instrumentenkunde*, vol. 20, p. 47, 1900.
- [130] B. C. Platt and R. Shack, "History and principles of Shack-Hartmann wavefront sensing," *Journal of Refractive Surgery*, vol. 17, pp. 573–577, 2001.
- [131] I. N. Bronstein, K. A. Semendjajew, G. Musiol, *et al.*, *Taschenbuch der Mathematik*. Europa-Lehrmittel, 2013.
- [132] *Mathematica 8.0*. Champaign, Illinois: Wolfram Research, Inc., 2010.
- [133] T. Auguste, P. Monot, L.-A. Lompré, *et al.*, "Defocusing effects of a picosecond terawatt laser pulse in an underdense plasma," *Optics Communications*, vol. 89, pp. 145–148, May 1992.
- [134] H. Kim, I. Kim, V. Tosa, *et al.*, "High brightness harmonic generation at 13 nm using self-guided and chirped femtosecond laser pulses," *Applied Physics B: Lasers and Optics*, vol. 78, pp. 863–867, May 2004.
- [135] M. Schultze, E. Goulielmakis, M. Uiberacker, *et al.*, "Powerful 170-attosecond XUV pulses generated with few-cycle laser pulses and broadband multilayer optics," *New Journal of Physics*, vol. 9, pp. 243–243, Jul 2007.

- [136] M. Hutley, *Diffraction Gratings*. Academic Press Inc, 1982.
- [137] T. Mey, S. Zayko, C. Ropers, *et al.*, "Toroidal grating astigmatism of high-harmonics characterized by EUV Hartmann sensor," *Optics Express*, vol. 23, pp. 15310–15315, Jun 2015.
- [138] B. L. Henke, E. M. Gullikson, and J. C. Davis, "X-Ray Interactions: Photoabsorption, Scattering, Transmission, and Reflection at $E = 50\text{--}30,000$ eV, $Z = 1\text{--}92$," *Atomic Data and Nuclear Data Tables*, vol. 54, pp. 181–342, Jul 1993.
- [139] P. Villorosi, "Compensation of Optical Path Lengths in Extreme-Ultraviolet and Soft-X-Ray Monochromators for Ultrafast Pulses," *Applied Optics*, vol. 38, pp. 6040–6049, Oct 1999.
- [140] B. Flöter, P. Juranić, P. Großmann, *et al.*, "Beam parameters of FLASH beamline BL1 from Hartmann wavefront measurements," *Nuclear Instruments and Methods in Physics Research Section A*, vol. 635, pp. S108–S112, Apr 2011.
- [141] E. Hecht, *Optics*. Addison-Wesley, 2001.
- [142] R. Bartels, S. Backus, E. Zeek, *et al.*, "Shaped-pulse optimization of coherent emission of high-harmonic soft X-rays," *Nature*, vol. 406, pp. 164–166, Jul 2000.
- [143] R. A. Bartels, A. Paul, M. M. Murnane, *et al.*, "Absolute determination of the wavelength and spectrum of an extreme-ultraviolet beam by a Young's double-slit measurement," *Optics Letters*, vol. 27, p. 707, May 2002.
- [144] *MrBeam 3.6.0*. Laser-Laboratorium Göttingen e.V., 2012.
- [145] B. Flöter, P. Juranić, S. Kapitzki, *et al.*, "EUV Hartmann sensor for wavefront measurements at the Free-electron LASer in Hamburg," *New Journal of Physics*, vol. 12, p. 083015, Aug 2010.
- [146] H. Wabnitz, L. Bittner, A. R. B. de Castro, *et al.*, "Multiple ionization of atom clusters by intense soft X-rays from a free-electron laser," *Nature*, vol. 420, pp. 482–485, Dec 2002.
- [147] A. Sorokin, S. Bobashev, T. Feigl, *et al.*, "Photoelectric Effect at Ultrahigh Intensities," *Physical Review Letters*, vol. 99, p. 213002, Nov 2007.

- [148] B. Nagler, U. Zastra, R. R. Fäustlin, *et al.*, “Turning solid aluminium transparent by intense soft X-ray photoionization,” *Nature Physics*, vol. 5, pp. 693–696, Sep 2009.
- [149] H. N. Chapman, S. P. Hau-Riege, M. J. Bogan, *et al.*, “Femtosecond time-delay X-ray holography,” *Nature*, vol. 448, pp. 676–679, Aug 2007.
- [150] T. Mey, B. Schäfer, K. Mann, *et al.*, “Wigner distribution measurements of the spatial coherence properties of the free-electron laser FLASH,” *Optics Express*, vol. 22, pp. 16571–16584, Jun 2014.
- [151] V. Ayvazyan, N. Baboi, J. Bähr, *et al.*, “First operation of a free-electron laser generating GW power radiation at 32 nm wavelength,” *The European Physical Journal D*, vol. 37, pp. 297–303, Feb 2006.
- [152] S. Schreiber, “First lasing in the water window with 4.1 nm at FLASH,” in *Proceedings of FEL2011, Shanghai, China*, pp. 164–165, 2011.
- [153] S. Düsterer, P. Radcliffe, G. Geloni, *et al.*, “Spectroscopic characterization of vacuum ultraviolet free electron laser pulses,” *Optics Letters*, vol. 31, no. 11, p. 1750, 2006.
- [154] R. Simon and N. Mukunda, “Twisted Gaussian Schell-model beams,” *Journal of the Optical Society of America A*, vol. 10, pp. 95–109, Jan 1993.
- [155] F. Siewert, J. Buchheim, T. Zeschke, *et al.*, “Sub-nm accuracy metrology for ultra-precise reflective X-ray optics,” *Nuclear Instruments and Methods in Physics Research Section A*, vol. 635, pp. S52–S57, Apr 2011.
- [156] A. Singer and I. A. Vartanyants, “Modelling of partially coherent radiation based on the coherent mode decomposition,” *Advances in Computational Methods for X-Ray Optics II*, p. 814106, Sep 2011.
- [157] “ISO 11146-1: Lasers and laser-related equipment – Test methods for laser beam widths, divergence angle and beam propagation ratio – Part 1: Stigmatic and simple astigmatic beams,” 2003.
- [158] “ISO 11670: Lasers and laser-related equipment – Test methods for laser beam parameters – Beam positional stability,” 2005.

- [159] B. Schäfer and K. Mann, "Characterization of an ArF excimer laser beam from measurements of the Wigner distribution function," *New Journal of Physics*, vol. 13, p. 043013, Apr 2011.
- [160] M. Müller, T. Mey, J. Niemeyer, *et al.*, "Table-top soft x-ray microscope using laser-induced plasma from a pulsed gas jet," *Optics Express*, vol. 22, no. 19, p. 23489, 2014.
- [161] H. Kogelnik and T. Li, "Laser Beams and Resonators," *Applied Optics*, vol. 5, no. 10, pp. 1550–1567, 1966.
- [162] A. E. Siegman, "ABCD-matrix elements for a curved diffraction grating," *Journal of the Optical Society of America A*, vol. 2, p. 1793, Oct 1985.

DANKSAGUNG

Zu dieser Arbeit haben unzählige Personen ihre individuellen Beiträge geleistet, ohne die ein Gelingen in dieser Form nicht möglich gewesen wäre. Im Allgemeinen ist dabei die angenehme und freundliche Arbeitsatmosphäre zu nennen, die alle Kollegen des Laser-Laboratoriums sowie des SFB755 gleichermaßen prägen, ob im Arbeitsalltag oder im Rahmen von Dienstreisen und Exkursionen. Dafür möchte ich mich bei diesem Umfeld bedanken.

Im Speziellen danke ich Herrn Prof. Dr. Tim Salditt für die Übernahme des Erstreferats dieser Arbeit und die damit verbundene fachliche Unterstützung sowie für die Einbindung in eine hervorragende wissenschaftliche Umgebung. Ebenso gebührt mein Dank Herrn Prof. Dr. Claus Ropers für die produktive Zusammenarbeit im Sonderforschungsbereich und für die Übernahme des Korreferats.

Großer Dank gilt insbesondere Herrn Dr. Klaus Mann für die stets sehr gute wissenschaftliche Betreuung sowie die Möglichkeit, die erarbeiteten Ergebnisse international auf zahlreichen Konferenzen zu präsentieren.

Weiterhin danke ich den folgenden Personen:

- Dr. Bernd Schäfer für ausführliche und hilfreiche fachliche Diskussionen
- Jens-Oliver Dette und Andreas Spata für die Unterstützung bei der Konstruktion und Fertigung von benötigten Teilen
- Maik Lübbecke für die kompetente Lösung IT-spezifischer Probleme
- Barbara Keitel, Marion Kuhlmann und Elke Plönjes vom DESY für die kompetente und nette Unterstützung während der Messzeiten an FLASH
- Sergey Zayko für die fruchtbare Zusammenarbeit an der HHG Quelle

Ein ganz besonderer Dank gebührt meinen Eltern sowie meiner Freundin Michaela, die mir zu jeder Zeit den nötigen Rückhalt boten, um diese Arbeit anzufertigen.

LEBENS LAUF

Person

Name	Tobias Mey
Geburtsdatum	14.07.1984
Geburtsort	Hildesheim
Staatsangehörigkeit	Deutsch

Wissenschaftlicher Werdegang

10/2004 - 10/2006	Grundstudium der Physik Technische Universität Carolo-Wilhelmina zu Braunschweig
10/2006 - 05/2010	Hauptstudium der Physik Georg-August Universität Göttingen & Deutsches Zentrum für Luft- und Raumfahrt e.V.
05/2010	Diplom in Physik (Dipl. Phys.)
10/2010 - 11/2014	Promotion Georg-August Universität Göttingen & Laser-Laboratorium Göttingen e.V.

Electromagnetic radiation in the extreme UV and soft x-ray spectral range is of steadily increasing importance in fundamental research and industrial applications. An optimum use of the available photons can only be achieved under condition of a comprehensive beam characterization. Following that goal, this work addresses the pathway of extreme UV and soft x-ray radiation from its generation, through the beam transport by the beamline to the probe position. Experimentally, those aspects are optimized at a laser-produced plasma source and at an arrangement for the generation of high-harmonics. Additionally, the coherence of laser beams is analyzed by measurements of the Wigner distribution function. This method is applied to the photon beam of the free-electron laser FLASH, resulting in the entire characterization of its propagation properties.



ISBN 978-3-86395-211-2
ISSN 2191-9860

Universitätsverlag Göttingen